UNIVERSITY OF CANTERBURY

MASTERS THESIS

The Production of Custom Bolus using 3D printers for applications in Radiation Therapy

	Supervisor:
Author:	Dr Steven MARSH
Anthony KARL	*Co-Supervisor:*
	Dr Jerome GASTALDO

A thesis submitted in partial fulfilment of the requirements

for the degree of Master of Science in Medical Physics

in the

Department of Medical Physics

May 2016

Declaration of Authorship

I, Anthony KARL, declare that this thesis titled, 'The Production of custom Bolus for use in radiation Therapy' and the work presented in it are my own.

I confirm that:

- This work was done wholly or mainly while in candidature for a research degree at this University.
- Where any part of this thesis has previously been submitted for a degree or any other qualification at this University or any other institution, this has been clearly stated.
- Where I have consulted the published work of others, this is always clearly attributed.
- Where I have quoted from the work of others, the source is always given. With the exception of such quotations, this thesis is entirely my own work.
- I have acknowledged all main sources of help.
- Where the thesis is based on work done by myself jointly with others, I have made clear exactly what was done by others and what I have contributed myself.

Signed: Anthony Karl

Date:23/05/2016

Table of contents

Acknowledgements

This masters would not have been possible without considerable contributions from a range of people. I would like to thank the following for their assistance:

Firstly, my fiancée Centaine, for your ongoing emotional and writing support throughout this long arduous process.

Georgia, for your grammatical assistance, and determination, day and night, from the other side of the world.

Terry and Josh, for your endless technical and engineering assistance and advice.

Jerome and Steve, for you perseverance and persistence in helping me to finish this project.

David, for your support and understanding as well as some practical proof-reading assistance.

The staff at St Georges Cancer Care Centre for all their support and encouragement

The staff in the Oncology department at Christchurch Hospital for endless discussions and ongoing support.

Abstract

The nature of this work was to determine whether it was feasible to produce 3D printed bolus in a clinical setting and determine the most water equivalent 3D printed material for use as a bolus. Predictions of the water equivalence of multiple 3D printed plastics were made based on their electron density and effective Z. TMR and point dose measurements were carried out to estimate the attenuation properties of the plastics. CT, mass attenuation coefficients and PDDs were compared as methods for determining the radiation properties of the 3D printed plastics. To find the optimal depth scaling factor, the difference between the PDDs measured in the 3D printed plastics and the PDD measured in water were minimised. It was determined that ABS was the most water equivalent 3D printing plastic and could be printed to a sufficient quality for use a bolus material in a clinical setting. A methodology was developed to export a bolus structure created in the clinical treatment planning system and generate a file printable by the 3D printer. ABS was then used to produce an example of clinical bolus and when compared to other clinical bolus materials, the 3D printed bolus shifted the dose distribution by the same amount but provided a higher surface dose.

1 Introduction

Cancer is the leading cause of death in New Zealand, comprising approximately 30% of all deaths (Ministry of Health, 2010). There are currently many options for the treatment of cancer (Brannon-Peppas & Blanchette, 2012).The most common modalities are: surgery, in which the diseased tissue is mechanically removed, chemotherapy, which utilises cytotoxic drugs to preferentially damage cancerous cells and radiation therapy. Radiation Therapy is a technique whereby ionising radiation is delivered to diseased tissue to cause damage to the cell's DNA and prevent cell division. Although all the aforementioned methods are commonly used, this work will concentrate on radiation therapy. The Ministry of Health claim in their report "Cancer: New registrations and deaths" that 45-52% of people with cancer would likely benefit from treatment with radiation therapy, either as a standalone treatment or as part of a combined treatment plan in conjunction with surgery and/or chemotherapy (Ministry of Health, 2010).

3D printing is a tool becoming more commonly available in the hospital system and industry. A potential application of 3D printers in radiation therapy clinics is to produce objects that can be used as tissue substitutes. As such, the focus of the work presented in this thesis is to investigate the use of 3D printed materials as a mechanism for altering the depth at which treatment occurs.

This thesis will be structured as follows: Chapter 1 provides background information for the thesis. This includes sections on Radiation Therapy, photon and electron interactions, tissue substitutes and 3D printing. Chapters **Error! Reference source not found.** and 3 follow the same format and are broken down into a series of investigations leading to the evaluation of 3D printers for the production of clinical bolus. Chapter 2 describes the materials and methods and Chapter **3** describes the results and then discusses them. Finally Chapter 4 provides a summary of the thesis.

The introduction is divided into three sections. The first section is an introduction to radiation therapy, which provides an overview of the important photon and electron interactions responsible for the deposition of energy in tissue and is essential to the understanding of why bolus is implemented in radiation therapy.

Section two describes tissue substitutes currently used as bolus in radiation therapy including their design and characteristics. This section also describes how bolus is used and what materials are commonly utilised in its manufacture.

Section three discusses the advent of the 3D printer, including an introduction to the current technology which includes the various printers as well as available printing media. It then goes on to describe what progress has already been made with 3D printing in radiation therapy.

1.1 Medical applications of 3D Printers

3D printing has been adopted into many clinical practices with $131.8 million already invested by the medical sector and that figure is expected to rise to $306 million within 5 years (3D Printing Industry).

According to Leary et al., (2015) "the design and cost benefits associated with additive manufacture are highly compatible with clinical requirements for improved patient outcomes and reduced cost and response time." The medical applications of additive manufacturing cover a wide range, and can include everything from surgical planning, medical education and training, to the fabrication of structural implants and tissue scaffolds. Examples include orthopaedic implants and surgical guides, neonatal modelling for expectant mothers, and site specific training models for surgical registrars. Research interest is also peaking with the number of articles on 3D printing that Pubmed references rising rapidly (Figure 1.1) as 3D printing finds its place in the biotechnology field.

Yet exploration of its uses in radiation therapy is only in its infancy. We plan to establish a recurring need in the radiation therapy field for patient specific bolus. Access to a 3D printer would offer a unique level of freedom providing the ability to efficiently and accurately produce inexpensive patient specific bolus.

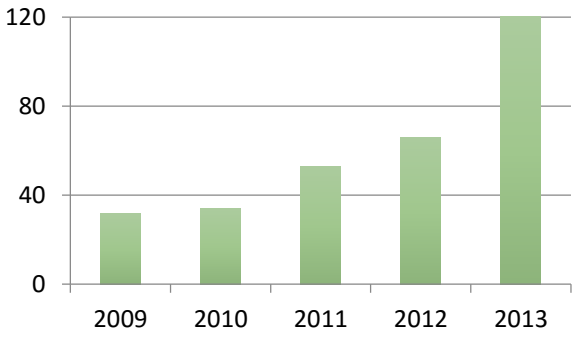

Figure 1.1 Number of Pubmed articles containing “3D Print”

3D printing bolus would mean less discomfort for the patients, especially those with claustrophobia and comorbidities, as the bolus would be designed from the planning CT scan which is required for treatment planning anyway. The process of defining the bolus within the treatment planning system and generating a form that can be interpreted by the slicing software will need to be determined. 3D printing the bolus will take longer to create that manual production but should require less labour costs as the printing process should not require supervision. Producing the bolus based on the patient's geometry mean that it is an exact model of the bolus defined within the treatment planning system. This should also mean that the bolus produced fits better to the patient's surface, reliably reducing air gaps. However, a 3D printed bolus will be rigid and therefore would not adapt to changes in the patients surface features.

1.2 Principles of Radiation Therapy

In Radiation Therapy (RT) the intention is to deliver a lethal dose of radiation to diseased tissue while sparing surrounding healthy tissues as much as possible. External beam radiation therapy is one method that attempts to achieve this by utilising external beams of ionising radiation, administered from a variety of angles to obtain a conformal dose.

The interaction of ionising radiation with matter is of particular interest as it determines how energy and hence dose (refer chapter 1.2.3) is absorbed in the medium (Attix, 1986).

1.2.1 Ionising radiation

Radiation that carries sufficient energy to eject one or more orbital electrons from atoms or molecules is referred to as ionising radiation (Hall & Giaccia, 2012). The threshold energy for ionisation events is in the order of $4 - 25\ eV$ ($50\ nm - \ 300\ nm$). Electromagnetic radiation in or above the upper range of the ultraviolet spectrum is ionising as it is above the threshold energy. The electromagnetic force is then transmitted by massless uncharged particles known as photons (Khan, 2010).

In modern radiation therapy clinics the main form of ionising radiation is x-rays, produced by a linear accelerator (LINAC). LINACs emit both characteristic x-rays and a spectrum of bremsstrahlung photons. LINACs will be discussed in more detail in Appendix 1. In this work, unless specified otherwise, characteristic x-rays, γ-rays and bremsstrahlung x-rays will be referred to simply as photons, as they are all electromagnetic radiation and their origin is generally of little consequence.

Charged particles such as electrons or protons are directly ionising meaning that they deposit energy, through Coulomb interactions, directly to the medium. Neutral particles, such as photons or neutrons, are indirectly ionising, depositing energy in a two-step process. During an interaction between a neutral particle and a charged particle, kinetic energy is transferred and the charged particle is set in motion in the medium. The charged particles then go on to have a directly ionising effect. Photons and electrons, in their respective indirect and direct interactions with the medium, are the focus of this work. The mechanisms by which energy is transferred from the incident photon to the irradiated medium are described in the next sections.

1.2.2 Microscopic radiation interactions

In this section we will consider interactions between matter and both photons and electrons on an individual particle level.

Photon interactions

Photon interactions are characterised as either absorption or scattering processes. In each interaction with the medium, some fraction of the photon's energy is transferred to particles in the medium. If the photon transfers all of its energy to the target entity, the interaction is a full absorption process. Secondary particles can be emitted but the incident photon is lost. In a scattering process, the photon is not lost but may undergo a change in energy, momentum or direction of motion. The primary absorption processes are photoelectric, pair production and triplet production. There are two types of scattering processes: Compton (incoherent) scattering and Rayleigh (coherent) scattering (Mayles, Nahum, & Rosenwald, 2007).

Photons can interact with atomic electrons and nuclei. The probability of interaction with such an entity is expressed in terms of the cross-section (σ) with the unit m^2. This is given by the fraction of the unit area that is occupied by the target area. The probability of interaction can be interpreted as the cross-sectional area (σ) that the target presents in the plane normal to the incident photon direction.

Compton (incoherent) Scattering

Incoherent scattering, of which Compton is the most relevant, is when some of the energy of the photon is transferred to the target entity. Compton scattering is also the dominant interaction process for photon beams used in megavoltage radiotherapy. These photon beams have sufficient energy that the electrons they interact with are considered to be free and at rest and therefore undergo Compton scattering. This implies that the electrons' kinetic and binding energies are of a magnitude that is negligible in comparison to the energy of the photons. The interaction with the target entity transfers part of the photon's energy to an atomic electron that is ejected from the atomic shell.

The Compton interaction cross-section is dependent on the energy of the incoming photon and the electron density of the medium, which is proportional to the ratio of atomic number and atomic weight (Hill, Brown, & Baldock, 2008). However, it is said that Compton interactions are essentially independent of the atomic number (Z) as the Compton mass attenuation coefficient ${}^{\sigma}/_{\rho} = \frac{N_A Z}{A}$ and ${}^{Z}/_{A}$ is roughly constant (Khan, 2010).

Rayleigh (coherent) Scattering

Rayleigh scattering occurs when a photon passes near an electron, is absorbed and causes it to oscillate. A photon is then re-emitted with the same energy as the incident photon. No energy is absorbed by the medium; the only effect is the scattering of the photon at small angles.

Rayleigh scattering is only briefly mentioned for comparison with Compton scattering as it only contributes a few percent or less to the total attenuation coefficient (interaction cross-section σ) in materials at MV therapeutic energy ranges.

Unlike Compton scattering, the Rayleigh interaction occurs when photons interact with orbital electrons whose binding energy is not negligible when compared to the energy of interacting photon, and therefore interacts with the atom as a whole.

The mass attenuation coefficient for Rayleigh scattering is proportional to $Z/(hv)^2$ and is therefore dependant on the atomic number of the absorbing material - unlike Compton scattering (Podgoršak, 2005).

Photoelectric absorption

In the process of photoelectric absorption, an incoming photon is absorbed by the atom and an atomic electron is ejected. The ejected electron has energy equal to the incoming photon minus the energy that bound the electron to the nucleus. The atomic interaction cross-section of photoelectric absorption is dependent on the atomic number and photon energy as:

$$\tau_m \propto \left(\frac{Z}{hv}\right)^3 \tag{1.1}$$

As a result, this process has a strong effect when it occurs in mediums with high atomic numbers, particularly when using low energy photons.

Pair Production and triplet production

Pair production is an interaction between the incident photon and the strong electromagnetic field produced by the nucleus, in which an electron-positron pair is created. The mass attenuation coefficient for pair production and triplet production varies approximately with Z.

The interaction to create the electron-positron pair requires a photon with a minimum energy of 1.022 MV ($2m_ec^2$). The photon is absorbed in the interaction and any excess energy the photon had is distributed between the electron and positron as kinetic energy. Apart from a very small amount of recoil energy to conserve momentum, the nucleus remains otherwise unchanged (Nelson & Reilly, 1991). The positron and electron then undergo collisions, losing kinetic energy until the positron combines with an electron in an annihilation process, releasing two gamma rays with energies of 0.511 MV. These photons produce a peak in the bremsstrahlung spectrum at 511 keV (Ali & Rogers, 2011).

If the interaction occurs in the Coulomb field of an orbital electron, instead of the nucleus picking up the extra momentum, it is transferred to the orbital electron. The recoil energy may be significant that the orbital electron is ejected from the atom. This effect is described as triplet production as three particles (two electrons and a positron) leave the interaction site.

Summary of photon interactions

At lower energies (10 keV), photoelectric interactions are dominant and therefore absorption has a high dependence on the atomic number (Z) of the attenuator. Compton interactions dominate at megavoltage treatment energies, making up 99% of the total cross section in muscle at 1 MV. As such, absorption is independent of Z but dependant on the electron density of the material. As energy increases past 1.022 MV, pair production starts to play a role, introducing a linear dependence on Z. At 100 MV pair production makes up 16% of the total attenuation in muscle (Orton, 2013). A reasonable approximation when determining the expected attenuation at treatment energies (1-10 MV), could be to assume that only Compton interactions occur.

Figure 1.2 illustrates the relative contribution of each interaction to the total interaction cross section for both carbon and lead from 10 keV to 100 MV. Having both elements illustrates the effect of atomic number on the relative contributions from each interaction but also carbon represents tissue like elements while lead illustrates the mechanical elements of the beam shaping system. It can be seen that the photoelectric effect (PE) has a lot larger impact at higher atomic numbers whereas pair and triplet production (Pair and Trip) do increase as dramatically. Compton (Incoh) plays a significant role is both cases but is pushed into middle range of energies out at higher atomic numbers.

Electron Interactions

Mobilised electrons from photon interactions undergo Coulomb interactions with both orbital electrons and atomic nuclei as they pass through matter.

Electronic collisions

Coulomb interactions are electrostatic interactions between charged particles and are inversely proportional to the square of the distance between them. The charged particles of interest are the negatively charged electrons of the beam and the positively charged nucleus surrounded by a negatively charged cloud of electrons that make up atoms.

The type of interaction that occurs is determined by how close the path of the free electron is to the atom. If the electron is distant from the electron cloud, the interaction will be a “soft” collision, interacting with the whole atom and imparting only a small amount of energy. If the electron comes into close contact with the electron cloud, but not so close as to interact with the nucleus, the electron will undergo a “hard” collision with an orbital electron, imparting a substantial fraction of its kinetic energy to the orbital electron. The energy transferred during the interaction either results in the ionisation of the absorbing atom if sufficient energy has been transferred to eject an electron, or if insufficient energy is transferred, the orbital electron is promoted into a higher orbit and the atom enters an excited state. To exit the excited state a photon will be emitted.

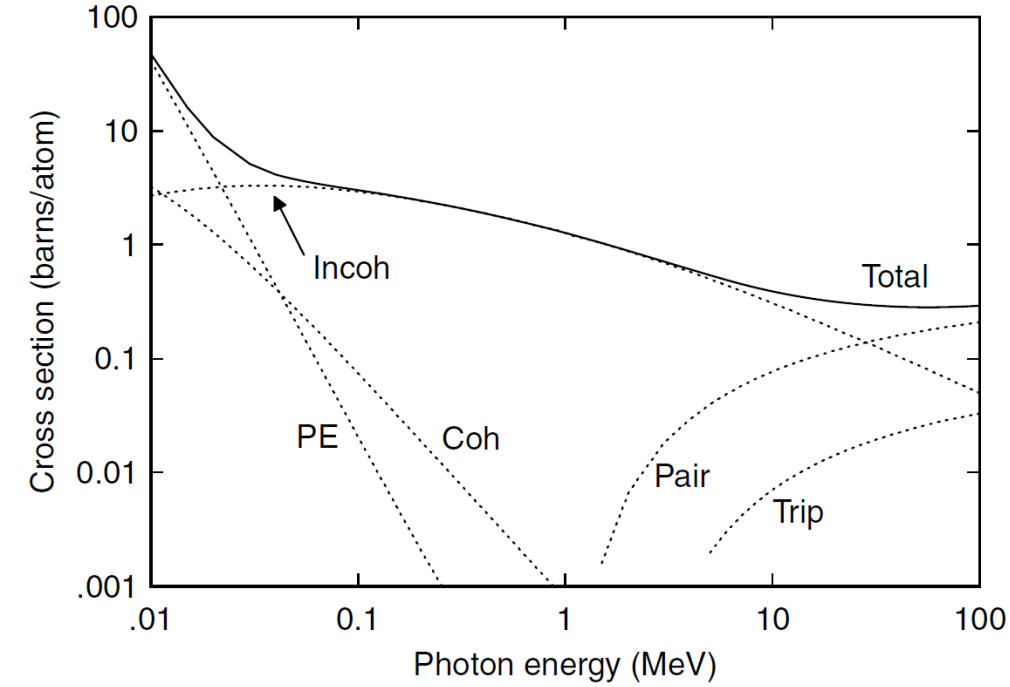

(a) Carbon

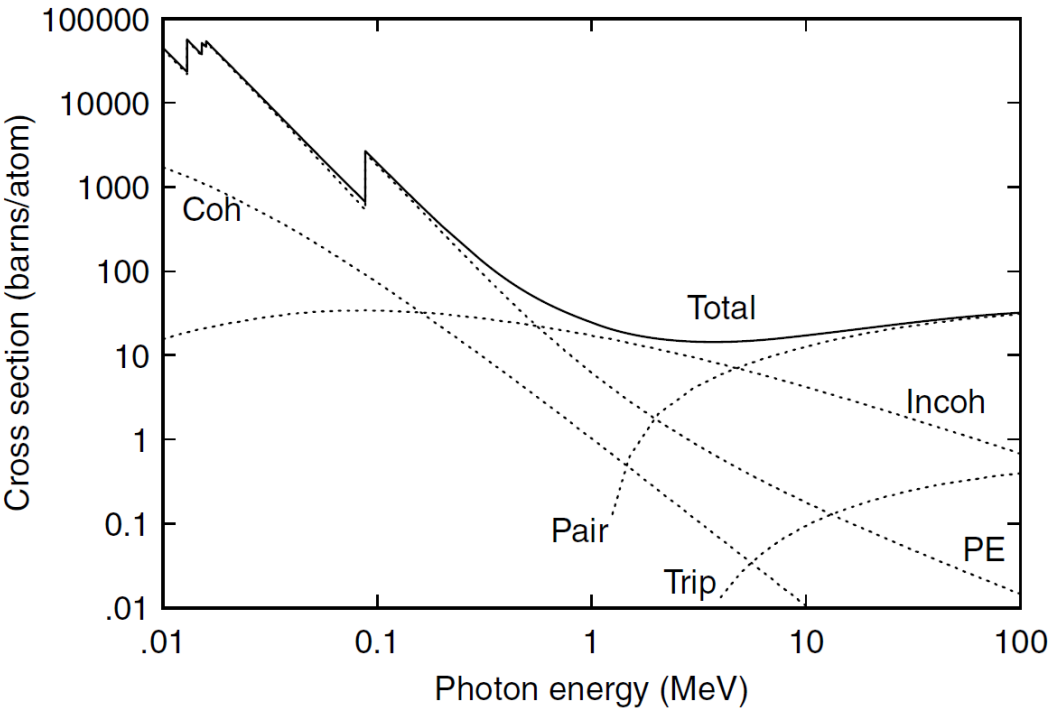

(b) Lead

Figure 1.2. The total and partial cross-sections for carbon (a) and lead (b) for photon energies from 10 keV to 100 MeV. (Data taken from Berger, M. J. and Hubbell, J. H., XCOM: Photon Cross Sections on a Personal Computer, 87-3597, NBS, Washington, DC, 1987.)

If the electron is on a path that will come close to the nucleus, the electron will undergo a radiative interaction, emitting a bremsstrahlung photon as the atomic nucleus accelerates the electron away from the nucleus. Bremsstrahlung photons have a continuum of energy depending on how much energy was imparted by the electron. The proportion of energy lost to bremsstrahlung photons increases with the energy of the electron and the atomic number (Z) of the material.

Both "hard" and "soft" collisions impart energy locally to the medium. The electrons set in motion by hard collisions can transport energy away from the local interaction site. Bremsstrahlung interactions also result in energy being transported away from the local interaction location but can also transport energy out of the medium. These types of energy losses are characterized by radiative stopping powers. The total mass-energy stopping power, is given by

$$(S/\rho)_{tot} = \frac{1}{\rho}\frac{dE_k}{dx} \tag{1.2}$$

where (E_K) is total kinetic energy lost per unit path length (x) by an electron as it moves through a medium undergoing both collisions and radiative interactions. $(S/\rho)_{tot}$ comprises two components $(S/\rho)_{col}$ and $(S/\rho)_{rad}$,

$$(S/\rho)_{tot} = (S/\rho)_{col} + (S/\rho)_{rad} \tag{1.3}$$

where $(S/\rho)_{col}$ is the energy lost by the electron to atomic excitations and ionisation when interacting with orbital electrons and $(S/\rho)_{rad}$ is the energy lost by the electron to bremsstrahlung photon production when the electron interacts with the nucleus (Podgoršak, 2005).

The effect of ionising radiation on cells

As described in the previous sections, both photon and electron interactions can result in ionisations. When these ionisations occur within living cells they can cause cell death, either damaging DNA directly, breaking bonds within the DNA molecule, or indirectly through the ionisation of water molecules which produces free radicals that interact with DNA molecules. The purpose of radiation therapy is to sufficiently damage the DNA of the tumour's clonogenic cells that they undergo cell death. Clonogenic cells are the replicative cells within the tumour that give rise to new tumour cells. Killing these cells will prevent growth and leads to regression of the tumour. However, the successful use of radiation therapy is largely due to a differential effect between clonogenic cells within a tumour compared to the surrounding normal tissues. One explanation for this difference in relative sensitivity

is because some cancerous cells have compromised DNA repair mechanisms which allows normal tissues to repair sub-lethal damage, whereas, the same sub-lethal damage in cancerous cells accumulates, becoming lethal.

1.2.3 Macroscopic Interactions

In this section we will consider the interaction of a beam of photons on a medium and describe how energy is deposited as dose.

Fluence

The first step in determining how and where dose is deposited is to describe the particles that will be interacting.

A photon beam, produced by a LINAC for use in radiation therapy, is made up of a spectrum of photons (this process is discussed in more detail is Appendix 1). To understand the properties of a beam of photons that feature numerous particles of different energies we need to shift from single particle interactions to a beam of photons, and we need to develop some new tools.

Shifting from single particle interactions to a beam of photons, we first need to specify how many particles are available to interact. The concepts of photon fluence and energy fluence are used to specify the number and the energy of the photons making up a beam.

Photon fluence

The photon fluence(Φ) is a measure of the number of photons $(\mathrm{d}N)$ that enter an imaginary sphere of cross-sectional area (dA) and is defined as follows:

$$\Phi = \frac{\mathrm{d}N}{\mathrm{d}A} \tag{1.4}$$

Energy fluence

The energy fluence (Ψ) is a measure of the radiant energy (dE) that enters an imaginary sphere of cross-sectional area (dA) and is defined as follows:

$$\Psi = \frac{\mathrm{dE}}{\mathrm{dA}} \tag{1.5}$$

The energy fluence can be calculated from the photon fluence by multiplying it by the energy of the incident photons (E).

$$\Psi = \frac{\mathrm{dN}}{\mathrm{dA}}\mathrm{E} = \Phi\mathrm{E} \tag{1.6}$$

Both photon fluence and energy fluence are defined for the mono-energetic photon, but they can be extended to address the spectral nature of beams produced by LINACs by considering the photon fluence spectrum. The photon fluence spectrum is the number of photons (dN) that enter an imaginary sphere of cross-sectional area (dA) in each energy range (dE), multiplied by their respective photon fluence.

Attenuation coefficients

The probability of interaction within the material also needs to be specified. This is described by the linear attenuation coefficient (μ), an energy dependent property of the material that describes the probability for interaction per unit length.

The linear attenuation coefficient is defined by Mayles et al. (2007) for the arrangement (depicted in Figure 1.3) where a flux of mono-energetic photons (Φ) have been collimated into narrow beam.

The beam encounters a medium with a thickness (t), and as particles traverse the medium to a depth (x) they have a chance to interact in each thin layer (dx), either being absorbed or scattered via the processes described in section 1.2.2.

$$d\Phi = -\mu dx\, \Phi(x) \tag{1.7}$$

Narrow beam geometry is then established by collimating again between the material and the detector. Narrow beam geometry assumes that only the photons that have passed though the materials without interacting have been counted or detected. Any photons that have interacted and been scattered by some angle are unlikely to be pass through the second collimator and reach the detector.

The total transmitted photon fluence can be determined by integrating from the surface ($x = 0$) to the depth of interest ($x = t$), summing all the interactions at each thin layer (dx),

$$\int_0^t d\Phi = \int_0^t -\mu\Phi(x)dx \tag{1.8}$$

which for a homogeneous medium, reduces to the well-established Beer–Lambert exponential attenuation law (Geraldelli, Tomal, & Poletti, 2013).

$$\Phi(t) = \Phi_0 e^{-\mu t} \tag{1.9}$$

The linear attenuation coefficient describes the exponential removal of photons from the primary beam with increasing thickness.

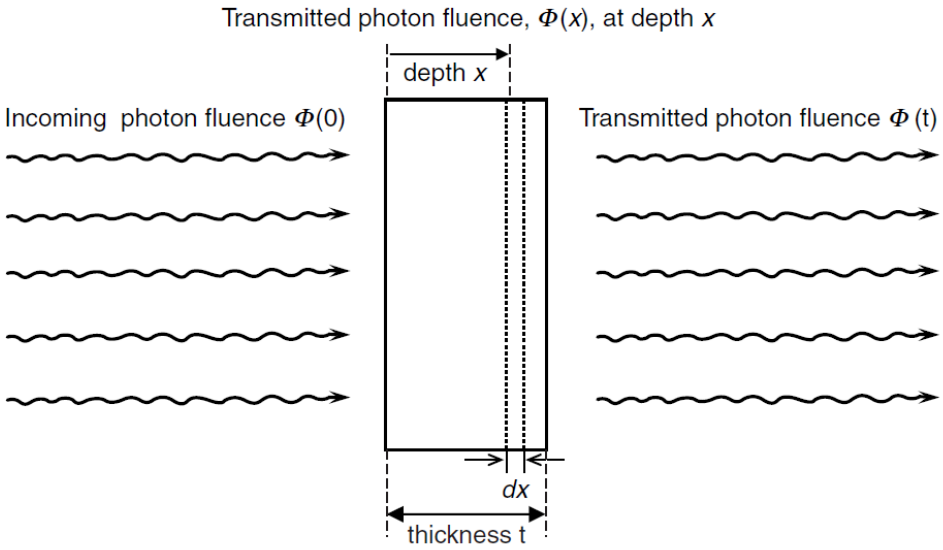

Figure 1.3. Calculation of photon transmission through a slab of matter. The incident fluence of primary photons $\boldsymbol{\Phi(0)}$ is reduced to a fluence $\boldsymbol{\Phi(x)}$ of primary photons at depth x in the slab (Mayles et al., 2007).

The linear attenuation coefficient is the sum of the attenuation coefficients of the photo-electric effect (τ), Compton (σ_C) and Raleigh scattering (σ_R) and pair production (κ).

$$\mu = \tau + \sigma_R + \sigma_C + \kappa \tag{1.10}$$

The density and thickness of the medium affects the likelihood of an interaction occurring. The mass attenuation coefficient is the ratio of the linear attenuation coefficient of the material and its mass density.

$$\mu_m = \frac{\mu}{\rho} \tag{1.11}$$

The mass attenuation coefficient is independent of the density of the material which makes it attractive for use in mixtures (Geraldelli et al., 2013). The mass attenuation coefficient for mixtures and compounds such as water can be calculated as the weighted sum of the mass attenuation coefficients of their components.

$$\frac{\mu}{\rho} = \sum w_i \left(\frac{\mu}{\rho}\right)_i \tag{1.12}$$

The Beer Lambert Law, introduced as equation 1.9 above, is commonly applied to the chemical analysis of materials. It relates the properties of a material to its attenuation of photons. Using a mono-energetic beam under narrow beam geometry the Beer-Lambert Law can be used to determine the linear attenuation coefficient of materials of interest.

As already discussed, photon beams produced by a LINAC feature a continuum of energies and are therefore not mono-energetic as the Beer Lambert Law requires. Expressing the quality of the photon beam produced by a LINAC in terms of the effective energy simplifies the poly-energetic beam into a mono-energetic beam. The effective (or equivalent) energy of an x- ray beam is the energy of photons in a mono-energetic beam that is attenuated at the same rate as the radiation in question.

One method for determining the effective energy is to determine the energy of mono-energetic photons that have the same μ as that given for a poly-energetic beam. However the μ of a heterogeneous beam varies with the absorber thickness, and therefore the effective energy will also vary. This is because the spectrum of the beam changes as it is attenuated, with lower energies being attenuated first, increasing the proportion of higher-energy photons and thus hardening the beam. The assumed effective energy will therefore only be valid over similar absorber thickness (Khan, 2010).

Practical application of attenuation

Radiographic techniques, specifically Computed Tomography (CT), are used to acquire the patient data required to simulate treatment for radiation therapy. It is the differences in the μ of materials that creates contrast for these radiographic techniques.

To carry out Monte Carlo treatment planning the patient's geometry needs to be known and segmented into voxels of known material and mass density (ρ). To do this a planning CT scan is taken and the CT number of each voxel is determined. Using the pre-established relationship between CT number and materials of known electron density, the CT numbers are converted into electron densities which are then used to infer the types of tissue that make up each voxel.

The CT number is defined as

$$HU = 1000\left(\frac{\mu - \mu_w}{\mu_w}\right) \tag{1.13}$$

where μ and μ_w are the linear attenuation coefficients for an arbitrary medium and water respectively. CT numbers are not standardised as spectral differences between scanners introduce differences in the energy dependent attenuation coefficients.

The known mass collision stopping powers, mass scattering powers, mass energy absorption coefficients and density of the materials are then used by the Monte Carlo based treatment planning algorithms to simulate particle histories and determine where dose is deposited (Verhaegen & Devic, 2005).

Linear attenuation coefficients only describe how many photons are removed from the beam. We are also interested in what happens to the photons after they interact and what energy is transferred. Scattering profiles describe exiting direction of the photons and the mass energy absorption

coefficients describe how energy is deposited in the medium. The scattering profiles are important because if we could measure both them and the attenuation coefficient we would have an independent measure of both the components of the PDD which could then be used to predict how the materials would influence the PDD, the clinically relevant parameter.

While scattering profiles are very important, they will not be examined directly in this project because we did not have access to the equipment required to make the measurements.

Energy Transfer Coefficient

Of particular interest, in a dosimetric sense, is the fraction of energy imparted by the incident photons to the medium. While the attenuation coefficient deals with the number of photons removed from the primary beam, it is the mass energy transfer coefficient μ_{tr}/ρ that describes the amount of energy transferred.

A photon travelling through a material that undergoes an interaction is removed from the primary beam. During the interaction, the photons transfer a fraction of their energy through ionisations and excitations of electrons in the medium.

To calculate the energy transferred the mass energy transfer coefficient μ_{tr}/ρ has been defined as

$$\frac{\mu_{tr}}{\rho} = \frac{\mu}{\rho}\frac{\bar{E}_{tr}}{h\nu} \tag{1.14}$$

where $\bar{E}_{tr}$ is the average energy transferred to charged particles per interaction.

The mass energy transfer coefficient is dependent on the type of interaction and the energy of the particles interacting. Like the linear attenuation coefficient, the mass energy transfer coefficient can be determined by taking the weighted sum of each of the photo-electric effect, Compton and Raleigh scattering and pair production coefficients.

When interacting, the electrons may produce secondary photons (as discussed in section 1.2.2 on bremsstrahlung) which transport energy away from the interaction site. The mass energy absorption coefficient μ_{en}/ρ allows for these losses

$$\frac{\mu_{en}}{\rho} = (1-g)\frac{\mu_{tr}}{\rho} \tag{1.15}$$

where g is the fraction of the energy lost to the production of bremsstrahlung photons.

Kinetic Energy Released per unit Mass (Kerma)

The kerma is defined as the sum of the initial kinetic energies of all the charged ionising particles liberated by uncharged particles $(\mathrm{d}E_{tr})$ in a material of mass $(\mathrm{d}m)$ (Mayles et al., 2007). Kerma shares the same SI unit of Gy with absorbed dose. The difference between the two is that the energy in kerma is the energy released and the energy in absorbed dose is the energy absorbed. These are not equal as some of the energy released is not absorbed but transported away.

Kerma is directly proportional to the photon energy fluence (Ψ) at a point given by:

$$K = \frac{\mathrm{d}E_{tr}}{\mathrm{d}m} = \Psi\left(\frac{\bar{\mu}_{tr}}{\rho}\right)_{med} \tag{1.16}$$

where $\bar{\mu}_{tr}/\rho$ is the mass energy transfer coefficient for the medium (discussed in the previous section), averaged over the energy fluence spectrum of the traversing photons.

Kerma can be divided into two parts:

$$K = K^{col} + K^{rad} = \Psi\left(\frac{\bar{\mu}_{en}}{\rho}\right) + \Psi\left(\frac{\bar{\mu}_{en}}{\rho}\right)\left(\frac{\bar{g}}{1-\bar{g}}\right) \tag{1.17}$$

where $K^{col} = \Psi\left(\frac{\bar{\mu}_{en}}{\rho}\right)$ is the kinetic energy of the electrons expended by inelastic collisions (ionisations and excitations) with atomic electrons $K^{rad} = \Psi\left(\frac{\bar{\mu}_{en}}{\rho}\right)\left(\frac{\bar{g}}{1-\bar{g}}\right)$ is the kinetic energy transferred to radiation in the form of bremsstrahlung photons and $\bar{g}$ is the small amount of kinetic energy expended in radiative collisions with atomic nuclei producing bremsstrahlung photons.

Dose

Absorbed dose is a measure of the mean energy imparted by ionizing radiation$(\mathrm{d}\bar{\varepsilon})$ to material of mass $(\mathrm{d}m)$ and has the SI unit of Gray (Gy) which is equal to $1\ \mathrm{J/kg}$. (ICRU 33 Radiation Quantities and Units 1980)

$$D = \frac{\mathrm{d}\bar{\varepsilon}}{\mathrm{d}m} \tag{1.18}$$

In a clinical setting, absorbed dose is of particular interest as it is linked to the biologically significant effects produced by ionizing radiation.

Absorbed dose describes the quantity of radiation deposited for all types of ionizing radiation, charged and uncharged, to all materials at all energies.

Charged particle equilibrium (CPE) is said to exist in a volume of irradiated medium if each charged particle of a given type and energy leaving the volume is replaced by an identical particle of the same

energy entering the volume (Mayles et al., 2007). When charged particle equilibrium has been established absorbed dose it is equal to the collision kerma (this is illustrated in Figure 1.4).

$$D_{med} = K^{col} \tag{1.19}$$

At higher energies, above approximately 1 MV, strict CPE does not exist as the photon fluence is appreciably attenuated with depth. Therefore, the number of secondary particles entering the volume at one depth cannot be replaced by an identical number of particles at some later depth.

K^{col} is instead proportional to absorbed dose which is dealt with by introducing a constant of proportionality β which is related to the mean distance the secondary charged particles carry their energy (Khan, 2010; Podgoršak, 2005).

$$D_{med} \overset{tcpe}{=} \beta K^{col} \tag{1.20a}$$

$$K^{col} \overset{tcpe}{=} D_{med} = \frac{1}{\beta}\Psi\left(\frac{\bar{\mu}_{en}}{\rho}\right) \tag{1.20b}$$

$$D_{med} \overset{tcpe}{=} \beta \int_0^{E_{\max}} E\Phi_{\mathrm{E}}\left(\frac{\mu_{en}(E)}{\rho}\right)_{med} \mathrm{d}E \tag{1.20c}$$

For electrons it is $(S/\rho)_{col}$ that plays the important role in determining dose. The dose D deposited by electron interactions in the medium may be calculated from the collisional stopping power by multiplication with the electron fluence as:

$$D = \phi(S/\rho)_{col} \tag{1.21}$$

Percentage depth dose curves (PDDs)

The mechanism determining how the energy from ionising radiation is deposited is a multistep process involving different types of interactions. The sum of all these interactions can be illustrated in PDDs. A PDD is a plot of how much dose is deposited per unit length of material. PDDs in water are used clinically as it is the main constituent of body fluids and it behaves similarly in terms of radiation interactions at the energies used in radiation therapy (Khan, 2010).

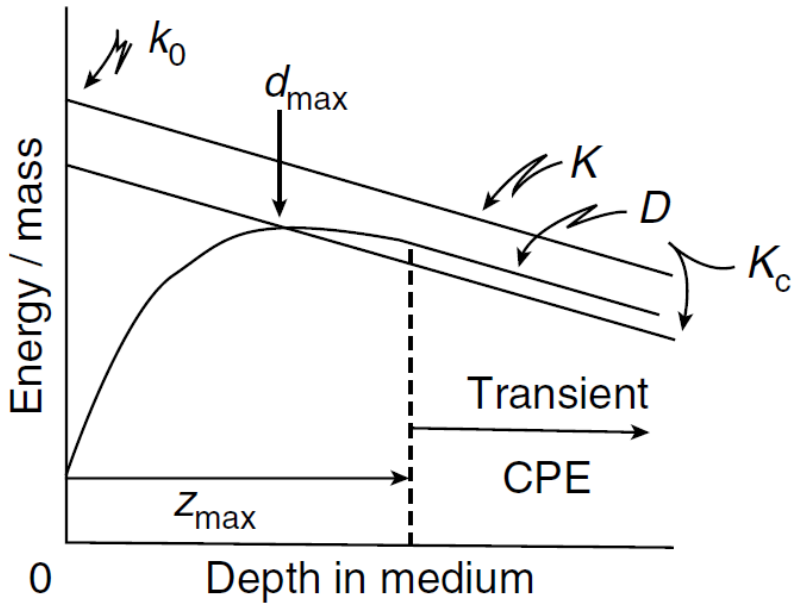

Figure 1.4. Variation of kerma ($\boldsymbol{K}$), collision kerma ($\boldsymbol{K_c}$), and dose ($\boldsymbol{D}$), with depth in a beam of indirectly ionising radiation such as a photon beam (Mayles, Nahum, and Rosenwald 2007).

A PDD is defined as the ratio, expressed as a percentage, of the absorbed dose at a point on the central axis divided by the absorbed dose at the depth of dose maximum (Boles, 1972). As the beam propagates through the medium it is absorbed and scattered. The sum of these effects is termed the attenuation and depends both on the medium and the energy spectrum of the beam. As the PDD measures how the beam is attenuated with depth, it is one of the fundamental parameters that characterise a radiation beam and can also be used to derive many other parameters.

There are two components that make up PDDs: the primary component and the scattered component. The primary component comes directly from the source and is a combination of the inverse square law and the attenuation by the medium, both of which reduce the primary component with distance.

For a poly-energetic photon beam, attenuation of the primary component is not strictly exponential. The low energy components of the beam will be attenuated more than the high energy components, increasing the mean energy of the primary beam and reducing the overall attenuation which moves away from an exponential relationship (Mayles et al., 2007).

The tissue phantom ratio (TPR) is defined as the ratio of the dose at a given point on the beam central axis in phantom to the dose at the same point at a fixed reference depth, all other machine parameters being constant.

$$TPR(z, A_Q, hv) = \frac{D_Q}{D_{Q_{ref}}} \tag{1.22}$$

The setup geometry for a TPR is illustrated in Figure 1.5. The TPR is essentially independent of the distance between the source and the surface of the patient for clinical Source to Surface Distances (SSD) which makes it useful for isocentric treatments. Similarly to PDDs, TPRs are dependent on the depth of measurement z, the field size and the energy of the beam (hv).

The TMR is a special case of the TPR where z_{ref} is chosen as d_{max} .

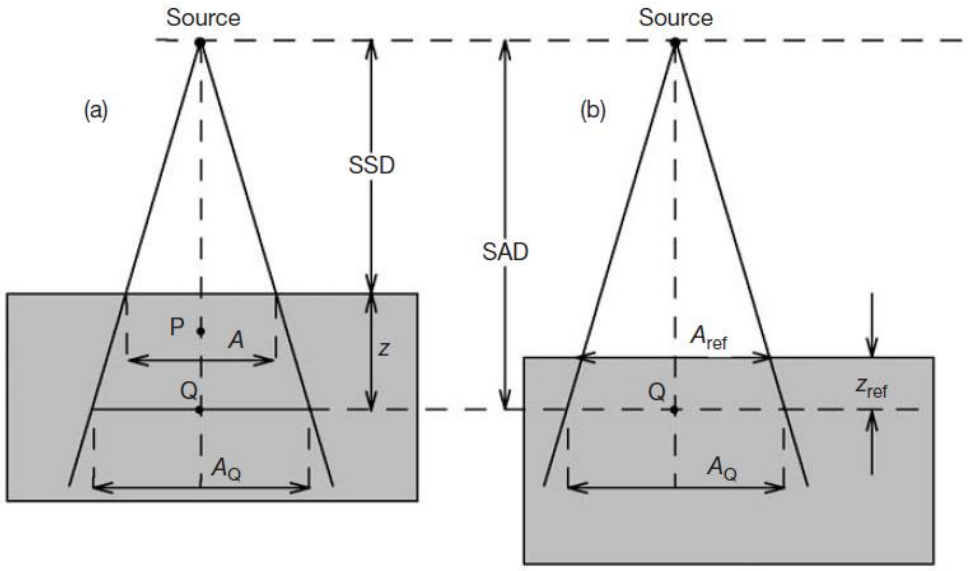

Figure 1.5 Geometry for measurement of TPR (a) The geometry for the measurement of dose at depth z in a phantom; (b) the geometry for the measurement of dose at depth $\mathbf{z_{ref}}$ in a phantom. The distance between the source and the point of measurement, as well as the field size at the point of measurement, is the same for (a) and (b) (Podgoršak, 2005).

Figure 1.6 shows the effect of field size on the spectrum of a 6 MV LINAC photon beam at 10 cm deep along the central axis. A nominal 6 MV beam is produced using electrons that are accelerated to 6 MV; therefore, the maximum energy of the photons will be approximately 6 MV. The fluence weighted mean x- ray energy for a nominal 6 MV beam with a 10 ×10 cm^2 field size was measured to be 1.29 MV. Whereas, for a 4×4 cm^2 field size, the fluence weighted mean x- ray energy increases to 1.65 MV and increases further to 1.93 MV for a 1×1 cm^2 field size (Benmakhlouf et al., 2014).

The PDDs of beams with smaller field sizes differ because of the increase in average energy of the beams spectrum because of the decreased scatter volume, making it more penetrative, meaning that more dose is deposited at greater depths.

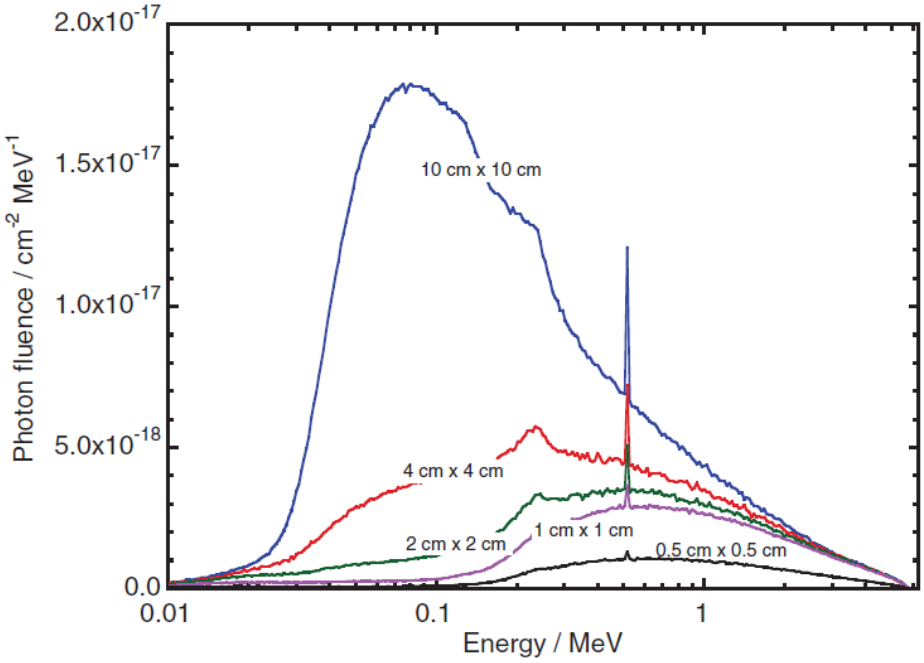

Figure 1.6. Monte Carlo calculations of the photon fluence in a small water volume in the beam central axis at 10 cm depth in water for five nominal square field sizes ranging from 0.5 × 0.5 cm2 to 10 × 10 cm2 of a Varian Clinac iX 6 MV clinical accelerator (Benmakhlouf, Sempau, & Andreo, 2014)**.**

1.3 Tissue Substitutes

In radiation therapy, tissue substitutes are materials used to simulate a particular body tissue with respect to a set of physical characteristics. Tissue equivalence is defined by the International Commission on Radiation Units (ICRU) as a material for which the absorption and scattering properties for a given irradiation, simulate as closely as possible those of a given biological material such as soft tissue, muscle, bone, or fat (White, Booz, Griffith, Spokas, & Wilson, 1989).

The average human body is composed of 65% water and therefore for some applications it can be appropriate, as well as more practical to achieve water equivalence instead of tissue equivalence. If a material is to be considered water equivalent, it is recommended by ICRU Report 44 that it should not introduce uncertainties to the absorbed dose of greater than 1% otherwise correction factors may be required (White et al., 1989).

In a strict dosimetric sense, achieving water equivalence requires the dose measured by a dosimeter in a water equivalent material and the dose measured in natural water to be equal.

However, it is not possible for a material, to be completely water equivalent for both photon and electron beams, at all depths and at all energies. A choice must be made depending on the application as to which characteristics are most important (Tello, Tailor, & Hanson, 1995). These characteristics include mass density, relative electron density and effective atomic number as well as similar absorption and scattering of radiation (Hill et al., 2008). As already stated in section 1.2.3 on attenuation coefficients, the mass density (ρ) of the medium affects the likelihood of an interaction occurring. It does this by influencing N, the number of target entities available per unit volume, which is shown by the following relationship,

$$N = \frac{N_A}{A}\rho \tag{1.23}$$

where N_A is Avogadro's number and A is the relative atomic mass. Therefore, mass density has an effect that is independent of the radiation interactions taking place and is instead solely dependent on a physical property of the medium. This implies that the density needs to be matched regardless of what the application is.

As already discussed, interaction probabilities for the photoelectric effect, Compton scatter and pair production processes are energy dependent. Therefore how water equivalent a material will be depends on the photon energy range of the application, which determines which interactions are more likely.

For photon energies where the photoelectric effect and pair production have a significant contribution, there is also dependence on the atomic number. For tissue substitutes that are atomic mixtures, the

effective atomic number Z_{eff} is used. The formula used for calculating Z_{eff} applies a different weighting to the atomic composition of the material depending on the energy of the photon beam.

In contrast, for photon energies where Compton interactions have a significant contribution, there is a dependency on electron density rather than Z_{eff} (Podgoršak, 2005).

The energy of the application determines which interactions are going to dominate and therefore whether the relative electron density or the effective atomic number of the tissue substitute is the most important characteristic.

σ_{pe} is the interaction cross section for the photoelectric effect, σ_{coh} is the interaction cross section for coherent or Raleigh scattering. σ_{incoh} is the interaction cross section for incoherent or Compton scattering. σ_{pair} is the interaction cross section for pair production and σ_{trip} is the interaction cross section for pair production similar to pair production.

No material will be exactly equivalent to another over the entire energy spectrum. The attenuation coefficient of the materials being used will not be identical to water as there may be different influences from its dependent interactions. As long as the attenuation coefficient is the same at the energy of interest, then the effective atomic number and electron density in the water equivalent material can be different from water. The material we are trying to match to the reference will not exactly match the attenuation coefficient, as there might be different influences from its dependent interactions. As long as the attenuation coefficient is the same at the energy of interest, then the effective atomic number and electron density in the reference and tissue/water equivalent material can be different.

1.3.1 Dose Depth scaling factor

When the absorbed dose in a water substitute differs by more than 1% from that measured in water, ICRU recommends that a correction factor be used. To ensure that the dose measured in the plastic water substitutes is equal to that measured in water, the scaling factor converts depths measured in a plastic water substitutes into the equivalent depth in water (Andreo et al., 2002). For photons, the so called "effective attenuation method" (ICRU 24) permits a correction factor (CF) to be defined as:

$$CF = e^{\bar{\mu}(d-d')} \tag{1.24}$$

where d is the actual thickness of the substitute material, d' is the equivalent thickness, and $\bar{\mu}$ is the experimentally derived effective linear attenuation coefficient.

Equal thicknesses of water and water substitutes will attenuate photons to the same extent if the total linear attenuation coefficients, over the appropriate energy interval, are identical for the two materials. The effective linear attenuation coefficient ($\bar{\mu}$) can be determined using the Beer-Lambert law which was discussed in 1.2.3 (Johns & Cunningham, 1983). However, it can be assumed that for photon beams, in energy ranges where Compton scatter dominates, that depth scaling factors can be taken as proportional to electron density (Mayles et al 2007).

1.3.2 Bolus

Bolus can be described as a water equivalent material that is generally placed in direct contact with the patient; either on the patient's external surface or inside a body cavity (D. A. Low & Hogstrom, 1994). ICRU recommends that bolus should not produce uncertainties in absorbed dose estimations in excess of 1% because of errors in thickness or attenuation properties (White et al., 1989).

Bolus was first used to provide additional scattering to a patient's surface, simplifying the scatter contributions from different parts of an irregular surface geometry. This creates a plane incident surface for the radiation beam to strike, reducing the difficulty in predicting the dose distribution, as shown in Figure 1.7. Bolus can also be used to compensate for missing tissue within a body cavity such as the ear canal or the nasal cavity (Morrison et al 1995) (Hogstrom 2004).

Figure 1.7. Custom 3D electron bolus in treatment position (R J Kudchadker, Antolak, Morrison, Wong, & Hogstrom, 2003)

Bolus is also very useful for the treatment of shallow tumours. In a clinical situation, a limited number of radiation modalities and energy combinations are available. In situations where dose needs to be delivered preferentially to a depth greater than desired that cannot be matched by an available energy or modality, the therapeutic range of a beam can be reduced by providing additional scattering material. This shifts the PDD towards the surface, as shown in Figure 1.8, allowing standard beam energies to be used. This does however, increase the dose to the skin which is usually spared by the reduced dose deposited while charged particle equilibrium is established.

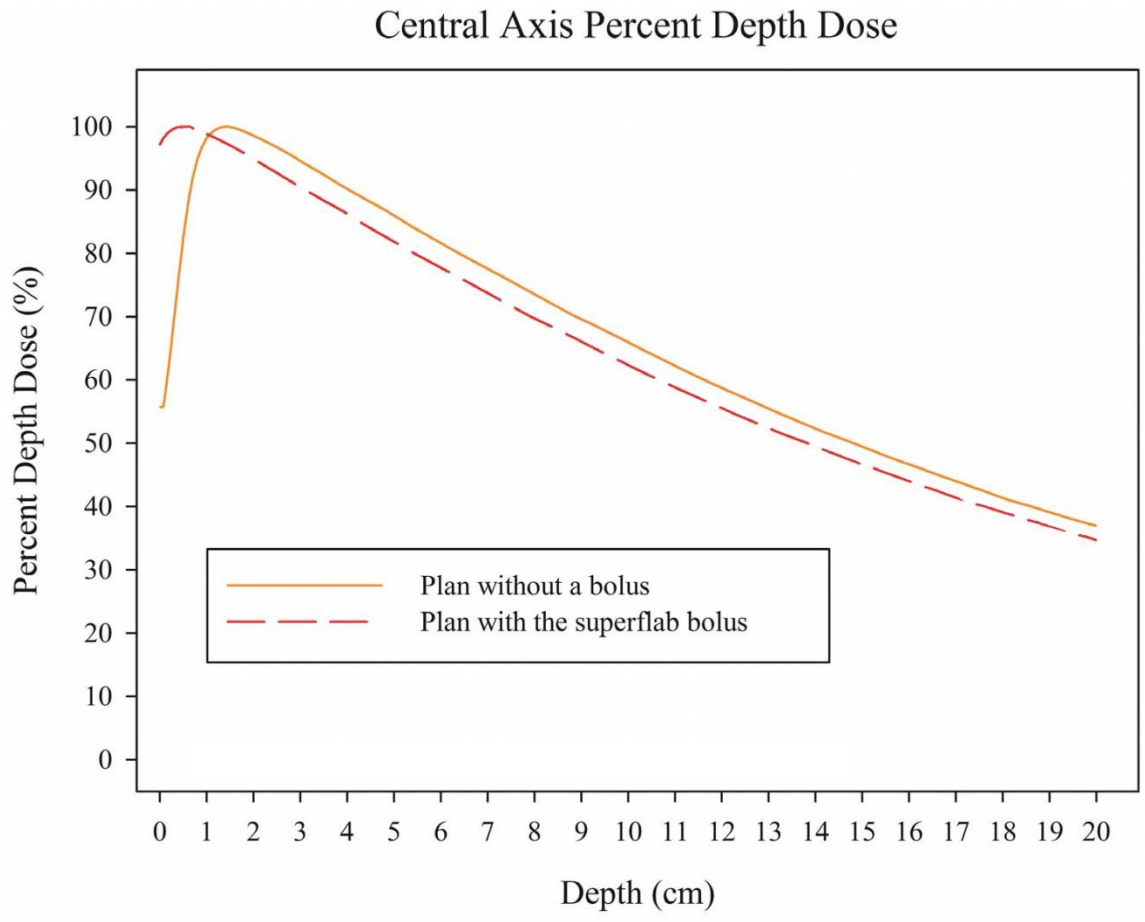

Figure 1.8. PDD Percent depth dose (PDD) at the central axis in the Blue water phantom study calculated from the treatment planning system with and without bolus. (adapted from Kim, Shin, Kay, & Son, 2014)

By taking into account both the patient's surface contours and the desired dose distribution, the thickness of the bolus can be tailored to modulate the intensity of the incident photon or electron beam to create the desired dose distribution (Rajat J Kudchadker et al., 2002; D. Low, Starkschall, Bujnowski, Wang, & Hogstrom, 1991). Electron conformal therapy can be achieved using patient specific bolus (Burleson, Baker, Hsia, & Xu, 2015). Patient specific bolus conform the dose to the desired location while minimising the dose delivered to adjacent and underlying critical structures and to normal tissues by providing additional scatter where required (Burleson et al., 2015). To determine the desired bolus geometry, the linear collision stopping power and linear scattering power of the material needs to be determined (Rajat J Kudchadker et al., 2002). The downside of patient specific bolus is that a new bolus needs to be manufactured for each patient.

Common Bolus materials and methods

Wax is commonly used as a material that is equivalent to adipose tissue and is a popular choice as a bolus material. Wax is low cost, non-toxic and is easily cast, moulded or machined into the required

geometry (Mayles et al., 2007). The production of wax bolus requires a cast of the patient to be created which is time consuming, labour intensive and uncomfortable for the patient. For patients with claustrophobia or comorbidities, such as breathing difficulties, the mould creation process can be impossible or may require input from a psychology expert.

Many companies produce bolus materials. Superflab is one such example and will be the commercially produced bolus material used in this project. It is purchased as flat sheets of the desired thickness. Superflab is ideal for clinical applications where the treatment surface has only a slightly changing gradient such as a breast (Mayles et al., 2007). Superflab is not the ideal bolus material to use on irregular patient surfaces such as the nose or face, as it cannot create perfect contact with irregular surfaces, leaving air gaps which reduces the surface doses (Kim et al., 2014). Variations in the size of the air gaps can be difficult to detect in day to day treatment, which in turn means it's difficult to estimate the dose actually delivered.

Third party companies, such as .decimal, will manufacture high accuracy patient-specific bolus, however using a third party company adds additional transportation time, costs and complexity to the process.

Polymethyl Methacrylate (PMMA) is a rigid plastic material that is more durable, holds its shape better and is less sensitive to temperature than wax, however it is not reusable and is harder to machine. It has a different electron density to tissue but can be used effectively if this is taken into account. If sheets are used, PMMA can be difficult to match to irregular patient surfaces, much like Superflab (Mayles et al., 2007).

1.4 3D printing

In the previous section common bolus materials and their production materials were discussed. This section introduces the concept of utilizing a 3D printer for manufacturing of patient specific bolus in the clinical environment. The fabrication of bolus requires the accurate production of complex geometries in a timely manner, while minimising labour and material costs. Onsite 3D printing could accelerate production with the required geometrical accuracy and with minimal capital investment and ongoing costs.

3D printing is the production of a physical object layer by layer as defined in a computer aided design (CAD) data set (Rengier et al., 2010). Additive manufacturing techniques, like 3D printing, can be used to create prototypes, both illustrative and functional, but also low-volume end product production. The object is created using 3D modelling software, which defines the object uniquely in a CAD data set. The CAD data set is then used to calculate the instructions or tool paths required to lay down the material on each layer to create the desired object (as shown in Figure 1.9)

The most commonly used material in 3D printing is plastic but other materials are available, some examples are metal, concrete, carbon fibre, rubber, glue and foodstuffs. Another exciting area using similar technologies is bio-printing in which animal cells are arranged into functional tissues (Melchels et al., 2012; Ventola, 2014).

It has become common for the terms 3D printing, additive manufacturing, and rapid prototyping to all be used synonymously. However, additive manufacturing specifically refers to a production technique whereby objects are built layer by layer, adding only the material required. In direct contrast to this are subtractive techniques like milling, where a solid block of material is shaped into the desired 3D object by the removal of material. Rapid prototyping is the construction of illustrative or functional prototypes. Additive manufacturing techniques have become especially pertinent in rapid prototyping as production times have be decreased from days to a few hours due to the inherent ease of creating one-off objects with little waste. Reducing waste also reduces the overall material costs (Rengier et al., 2010).

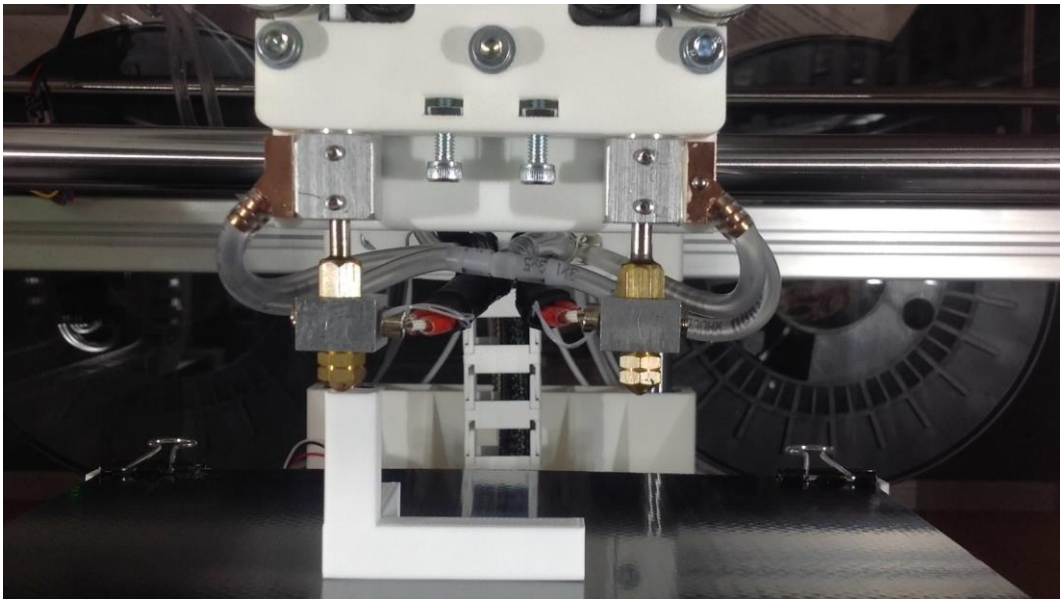

Figure 1.9. Example of FDM 3D printed depositing a layer of molten plastic for the upper layer of a CAD design**.**

1.4.1 Advantages and disadvantages

There are some inherent benefits to building up an object additively. Highly complex structures that are not possible with subtractive manufacturing are possible when they are being built up layer by layer. Additive techniques allow for the production of objects with internal structures which maintain structural strength while being lighter, and reducing material costs. Wasted material costs are largely avoided as the material used, in the most part, is that which is used in the final product. As production can be carried out onsite, only the raw materials are shipped, reducing packaging and transportation costs. With production times in the realm of hours, parts can be produced on demand. Depending on the size of the objects required, multiple objects can be printed concurrently, and if more throughput is required the cost of individual printers makes owning a number of printers to match the required production worthwhile. Rapid growth in the 3D printing industry has encouraged the development of 3D printer filaments using new materials to come to market. Each new material offers unique structural properties ranging from elastomers which are flexible to carbon fibre which has superior tensile strength (Stratasys Inc, 2012).

The key advantages of interest to the current project are the high degree of design freedom and the ability to manufacture small batch sizes at reasonable cost. The high degree of design freedom gained by printing from digital designs allows users with minimal design skills to produce simple structures easily. The ability to manufacture small batch sizes at reasonable cost means designs can be iterated quickly to deliver an optimised design at a reasonable cost per unit. The radiation therapy industry is not large enough to support large economies of scale, and the healthcare industry in general is moving

towards using products that are highly customised for specific patients to achieve better health outcomes for each patient.

Imaging and 3D printing

Using 3D CAD designs allows for easy sharing of information via the internet, facilitating collaboration between facilities that have access to 3D printing.

In radiation therapy the use of 3D imaging modalities, such as CT and MRI, facilitates the production of patient specific designs, as anatomical information can be extracted from the 3D imaging data and can be reproduced in the 3D CAD design. It has been shown that 3D printers can use these 3D representations to create physical objects that represent or are designed to fit a patient's specific anatomy. The use of 3D printing materials that are sterilisable and bio-compatible has allowed the production of patient-specific implants (Harris, Nilsson, & Poole, 2015).

Comparison with CNC Milling

Computer Numerical control (CNC) milling uses computers to define a coordinate system and control cutting and shaping tools within that system to form CAD designed objects out of raw materials. CNC milling is a more mature technology than 3D printing and is currently more precise as well. However the fact that CNC milling hardware is larger and more expensive means that there are significant barriers to entry. The hardware that makes up the positioning systems needs to be robust enough to deal with the resistance it encounters when removing materials. The subtractive nature also causes a messy environment and the large machinery creates an increased risk of injury.

The professional computer aided manufacturing (CAM) software that is used to create the tool paths for the milling machines is also expensive, although free software is available. CAM software is significantly more complex than the slicing software used in additive manufacturing because tool paths need to be manually defined and tweaked to avoid crashing the tool into the design. The added complexity creates impedance for new users without the support of a network of like-minded creators that the 3D printing industry currently has (France, 2013).

1.4.2 Techniques

There are many methods to "print" physical objects from digital designs. The method that will be used in this project is Fused Filament Deposition (FDM) which is also referred to as fused filament fabrication (FFF) in the literature. Other techniques will also be briefly described to provide contrast and to illustrate the other possibilities available.

Fused Filament Deposition (FDM)

FDM printers are based on the heating and layering of thermoplastics. Thermoplastics are polymers that change to a liquid form when heated above a specific temperature. Upon the application of liquid polymer to a cool surface the polymer solidifies. Applying the liquid polymer to a layer of the same polymer that has had time to cool and solidify creates a strong bond between layers.

In FDM printers the thermoplastic filament is fed into a chamber within the hot end where it is heated above its characteristic glass transition temperature, and it changes into a semi-molten state. As more filament is fed into the chamber, pressure builds and extrudes the semi-molten plastic through a nozzle producing a fine thread. The continuous thread of plastic is then precisely deposited into a layer that represents the cross section of the desired object. The laying down of plastic is guided by instructions created from the slicer. The slicer is a piece of software that takes the CAD file and uses the known characteristics of the desired object to create the instructions required to recreate the objects geometry. This layering process repeats and each layer bonds to the layer below and promptly hardens to represent the cross section of the object at every level until the final object has been produced. Support material is material that is not intended to be included in the final design but is required where there are no layers directly below part of the print. These may be used and would need to be removed after printing is complete. The requirement for the layer above to be supported by the layer below effects the optimisation of objects designed that are intended to be produced by FDM and most other additive manufacturing techniques (Hiemenz & Stratasys Inc, 2008).

RepRap project

Until recently, 3D printers have been unobtainable for small scale use as they had high capital cost and large operating costs. Now, a huge range of 3D printers are available for as little as a few hundred dollars. This change was fuelled by the RepRap project; a group of scientists and engineers lead by Adrian Bower whose aim was to create a self-replicating machine. The group chose FDM printers as a method for creating the custom parts required to create another FDM printer. The rest of the required materials needed to be widely available, such as linear rods that can be purchased from a hardware store. One of the contributing factors for the RepRap project for choosing FDM printers was due to the expiration of a number of key patents in FDM printers. The momentum created by the RepRap project has seen the price of FDM printers fall rapidly, flooding the home consumer market with a wide variety of FDM printers. This has also had the benefit of reducing the cost of the higher end 3D printers and has made them accessible to small businesses.

The use of FDM printers by the RepRap project has made the production of FDM printers in a hobbyist setting possible. Numerous commercial entities have built upon the work done by the RepRap project and hobbyists to create unique printers that use similar core technologies. The use of similar core technologies within the FDM printer community makes hardware upgrades easier. The

relative ease of upgrading was seen to aid our research as keeping up with the swiftly changing technology could require regular modification (Zwicker, Bloom, Albertson, & Gershman, 2015)(Jones et al., 2011).

The printers used for this project were FDM printers due to their low cost, large build, the range of materials available and the cost of those materials.

Stereo lithography (SLA)

SLA was the first form of 3D printing to be realised by Chuck Hull in 1986. SLA utilises photopolymers that solidify or cure when exposed to UV (Rengier et al., 2010). A UV laser beam, directed into a pool of photopolymer, traces the cross-section pattern of the model for that particular layer onto a platform and cures it. The platform is then repositioned, moving by a single layer thickness and the process repeats until the object is completed (Hull, 1986).

Selective laser sintering (SLS)

SLS is a natural continuation of SLA and utilises a high powered laser to fuse small particles of plastic, metal, ceramic or glass together instead of curing plastics. The platform on which the build is taking place is lowered by a single layer thickness each time and another layer of material is added. The process is repeated until the object is completed. Unlike SLA and FDM technology, support material is not needed as the build is supported by unsintered material. This does however prevent the production of hollow objects as the hollow cavity would be filled with unsintered material. The removal of the unsintered material creates a labour intensive post processing chore that needs to be carried out after each print (Mazzoli, 2013).

Inkjet

Inkjet technology combines the precision technology found in traditional ink printers with materials used in other 3D printing methods. One type of Inkjet technology uses photopolymers precisely jetted from a carriage as it traverses the print that are then cured by a UV lamp attached to the inkjet carriage. Each time a cross section has been traced out, the surface lowers by a single layer and the process repeats. By adding additional print heads, just as you would for additional colours, the technique is easily extended to use multiple materials. With the option of combining materials, a continuum of materials would be available. The jetted material may be a photopolymer, such as those used in SLA, or adhesives that bond powders, similar to how the laser bonds materials in SLS (Dimetrov, Schreve, & Beer, 2006; Lindsay et al., 2015).

Each of the 3D printing technologies described have been used as the basis for the formation of today's largest 3D printing companies. 3D Systems uses SLA technology, Stratasys uses FDM, GmbH uses SLS and Z Corporation uses Inkjet.

1.4.3 Parameters

Here, the effect of different printing parameters will be discussed in turn and related to how they influence print quality. These parameters need to be well understood as they will directly influence the homogeneity of bolus produced and ultimately impact the clinical outcome.

Movement and Extrusion speed

The movement speed, the speed with which the head is moving, is set within slicer which X-Y detail size. The minimum and maximum extrusion width is dependent on the nozzle size. If the extrusion width is too large relative to the nozzle size, the filament could start to curl, which is not desirable. It is not recommended to have an extrusion width much smaller (75%) than the nozzle as filament is drawn out, which reduces the adhesion to the layer below.

The slicer assumes that the filament extruded onto a surface has a rectangular cross section with semicircular ends as depicted in Figure 1.10.

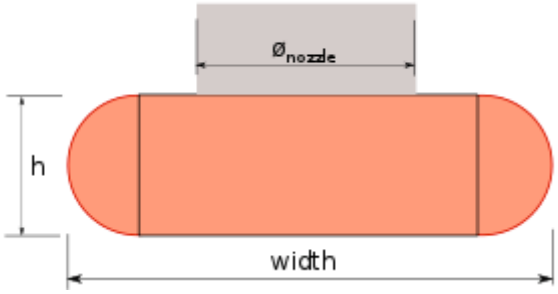

Figure 1.10 Diagram illustrating the assumed geometry used by the slicing software, where h is the layer height and ∅ is the nozzle diameter. Credit: Slic3r Manual

$$A = \text{rectangle} + \text{circle} = (w - h)h + \pi\left(h/2\right)^2 \tag{1.25}$$

where A is the cross-sectional area, w is the extrusion width and h is the layer height.

It is important for the production of tissue substitutes to have sufficient overlap, to minimise voids. Voids are due to the semicircular ends of the extruded filament, and in the worst case where there is no overlap the situation would be described by Figure 1.11, where the yellow is the voids.

Layer height affects the extrusion width possible, the Z resoltuion and the visibility of layers. It also drastically affects print time.

Figure 1.11. illustration depicticting the geometry of two extruded strands in red with no overlap and the voids in yellow formed with this geometry. Credit: Slic3r Manual

$$\text{void area} = h^2 - \pi \left(h/2\right)^2 \tag{1.26}$$

To achieve a homogenous infill, we would want to fill all of the voids using the overlap parameter. It is however unlikely that the second extrusion would completely fill the void, depending on the viscosity of extruded material and how much the previous extrudate has cooled. The amount of cooling depends on extrusion speed, temperature and geometry of the print.

"Slic3r", the slicing software we are using, corrects for the void using an overlap factor. By default the overlap factor is at its maximum, minimising voids but possibly over-extruding.

The amount of void is of interest to the current project as it determines the amount of air captured in each layer and therefore the effective density and mass attenuation coefficient of the material.

Temperature

A heated bed facilitates adhesion of the print to the bed surface and decreases the temperature gradient across the height of the print, reducing warping due to thermal contraction. Warping compromises the geometric accuracy of the object as it causes part of print, usually the corners, to become distorted and detach from the bed. In the worst case, the whole print can become detached causing the print to fail. A heated chamber is used for larger prints because it decreases the temperature gradient in the same way a heated bed does, but in all directions and over a larger volume. The nozzle temperature affects the number of materials that it is possible to print and must be finely tuned for each filament and each new batch.

Print volume

The print volume restricts how large an object can be printed without it breaking into multiple parts that then have to be assembled later. Assembly creates an additional point in the process where accuracy can be lost.

Bed adhesion

Good adhesion to the bed reduces printing failures and warping. Each 3D printing material adheres to some print surfaces better than others due to the different chemical properties. There are many options to enhance adhesion to the bed. Typical examples include: heating the print surface; choosing an

appropriate print surface material such as glass or Polyetherimide (PEI); covering the print surface in tape, plastics or adhesives such as Kapton tape, or hair spray; or optimising the object's design to minimise thermal mass while maximising the surface area in contact with the bed, such as printing objects hollow when possible, or adding a raft. A raft is a sparse horizontal latticework of filament that helps to stabilise designs with small footprints by increasing the surface area in contact with the bed.

1.4.4 Materials/Thermoplastics

Plastic is a category of polymer based on its physical properties. The polymers are either classified as elastomers (rubbers), plastics or fibres depending on their elastic modulus and tensile strength. Elastomers have the greatest elasticity and the lowest tensile strength while fibres have the greatest tensile strength but very low elasticity. Plastics have medium elasticity and medium tensile strength. A thermoplastic is a type of plastic whose deformation at elevated temperatures is reversible, whereas thermosets undergo irreversible changes when heated (Beyler & Hirschler, 2002).

The glass transition temperature is when the material starts a transition towards a soft and rubbery state. The states and transitions a thermoplastic undergoes as the temperature is increased are illustrated in Figure 1.12.

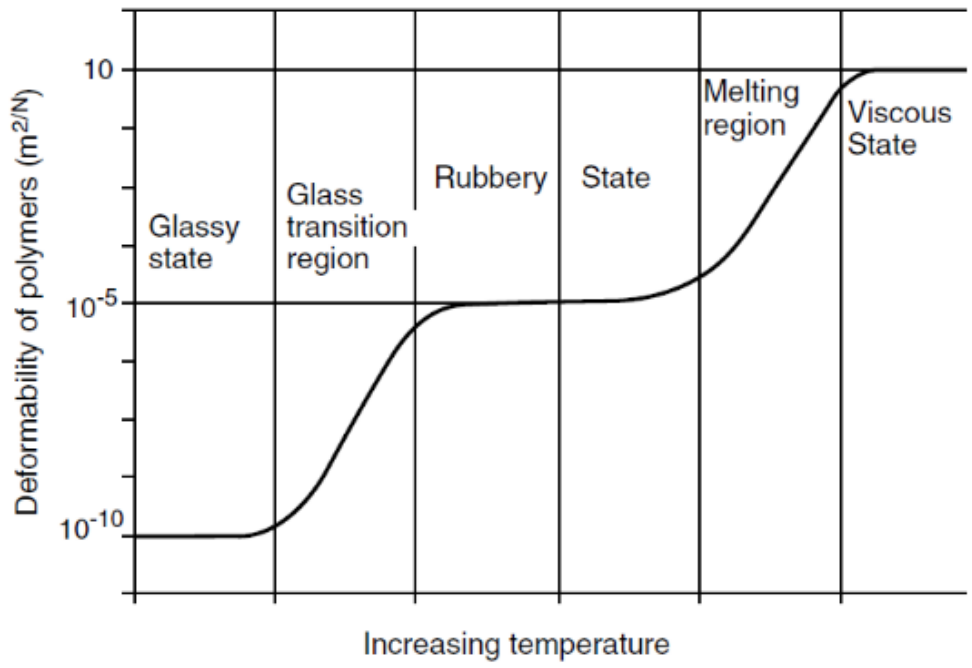

Figure 1.12. Idealised view of effect on deformability of thermoplastics with increasing temperature (Beyler & Hirschler, 2002).

Acrylonitrile Butadiene Styrene (ABS)

First developed in the early 1950s, ABS was one of the first material substrates for 3D printers and is still one the most widely used. ABS is a plastic that is made of three distinct monomers; acrylonitrile, butadiene and styrene (Cunha et al., 2015).

FDM printing has been built upon the use of ABS. Variations on the original ABS formulations have been developed to accentuate specific mechanical properties such as greater tensile, impact, and flexural strength (Fischer & Stratasys, 2011). Its malleability facilitates post-processing and the removal of support material with minimal loss of structural rigidity. It is a petroleum product with an extrusion temperature of around 250 ℃, which allows it to be used for most applications that do not require very high temperatures, but it produces an unpleasant odour during extrusion.

ABS can be produced by two general methods, each of which generate slightly different types of plastic: mechanical blending of a styrene-acrylonitrile copolymer resin with a butadiene-acrylonitrile rubber or grafting polybutadiene to the styrene-acrylonitrile copolymer. The elemental composition will therefore depend on the ratio of styrene to acrylonitrile in the styrene-acrylonitrile copolymer but also on the ratio of styrene-acrylonitrile copolymer to the butadiene component and any other additives. The composition of ABS can range from 15% to 35% acrylonitrile, 5% to 30% butadiene and 40% to 60% styrene (Kumar et al 2010).

Titanium dioxide ($Ti0_2$) is used as a whitening agent in ABS. The amount of $Ti0_2$ used could impact the water equivalence of 3D printed ABS, and could even be optimised to improve its water equivalence.

While it has not been approved as a biocompatible material, ABS has been used to make tissue equivalent phantoms for IMRT QA. Kumar et al., (2010) showed in their paper "ABS-based low-cost IMRT phantom" that when dose measurements in an ABS phantom were compared to those in a Scanditronic – Wellhofer IMRT RW3 phantom, corresponding points were within 2%. The finding suggests that ABS can be used to create a versatile tissue-equivalent phantom that is suitable for IMRT pre-treatment dosimetry checks. It should be noted however, that the phantom produced by Kumar et al. was not 3D printed but machined. As ABS has been shown to be tissue equivalent and is widely available as a 3D printing substrate, it serves as an ideal material to start investigating its applications to phantoms and especially as a bolus material.

Bed adhesion is a particular challenge for ABS as it is particularly prone to warping. Burleson et al., (2015) suggested that the warping of ABS during printing with their current printer precluded it from being used as a material for bolus even though it was more water equivalent than PLA, which will be introduced in the next section. However, there are many methods to reduce warping including using a

heated build surface, fully enclosed heated build chamber or ABS juice (a mixture of ABS dissolved acetone).

Table 1.1. Thermo-physical properties of ABS

Thermo-physical Property	Value
Glass transition temp	105℃
Melting point	NA
Molecular formulae	$C_8H_8 \bullet C_4H_6 \bullet C_3H_3N$
Physical Density	$\sim 1.04\ g/cm^3$
Hydrogen Content (by mass)	8%
Effective Z	3.45
Electron Density ratio compared to water	1.01

(Source:IDEMAT 2003)

Polylactic Acid (PLA)

PLA is quickly becoming the starting material of choice for many FDM printer manufacturers due to the fact that it is relatively easy to obtain good quality prints and is produced from renewable resources, is recyclable and does not produce an unpleasant odour. PLA particles are believed to be bio-compatible and are often used for drug delivery (Stephens, Azimi, El Orch, & Ramos, 2013).

Burleson et al., (2015) showed that there was a 1.5 mm shift in the depth of dose maximum between that measured in 3D printed clear PLA and that measured in water. They also found the average CT number of clear PLA to be 240 HU and the electron density ratio between clear PLA and water to be 1.14.

Similarly to ABS, PLA is an attractive candidate due to extensive use as a 3D printing substrate with the added benefit that it is bio-compatible and safer to print. However, PLA was never used as a tissue equivalent material before its use in 3D printing. Furthermore, being able to verify our results against published findings will be invaluable even though some parameters will inevitably be different between the two setups.

Table 1.2 Thermo-physical properties of PLA

Thermo-physical Property	Value
Glass transition temp	$45 - 65℃$
Melting point	$150 - 160℃$
Molecular formulae	$C_3H_4O_2$
Physical Density	$1.20 - 1.4\ g/cm^3$
Hydrogen Content (by mass)	6%
Effective Z	3.33
Electron Density ratio compared to water	1.14

(Source:IDEMAT 2003)

Polymethyl methacrylate (PMMA)

PMMA (also known as acrylic or Perspex™) was originally desirable for its high light transmittance, high strength and resistance to scattering, like silica glass. As an FDA approved synthetic biomaterial it is widely used to fabricate reconstructive structures, such as dental implants, implants for craniofacial defects, or as bone cement to remodel lost bone and affix implants. It is also a thermoplastic and is suitable for extrusion in FDM printing. However, when used as bone cement, the polymerization that is initiated in-situ when mixing and shaping the PMMA causes tissue necrosis. The long surgical times due to the manual sculpting can also lead to other complications. Using 3D imaging data, implants specific to the patient's own anatomy can be printed prior to surgery, removing the need to have the PMMA polymerize in situ, greatly improving patient outcomes. (Espalin, Arcaute, Rodriguez, Medina, & Posner, n.d.).

Although PMMA is not widely available as a 3D printing substrate, it is commonly used as a tissue substitute and is currently recommended for use as a water substitute for lower energy photons in TRS398 (Andreo et al., 2000). The tissue equivalence of PMMA has been well established and gaining access to a PMMA phantom for comparison measurement is relatively easy. It is also of interest to be able to compare a material that has been 3D printed against the same material not 3D printed.

Table 1.3 Thermo-physical properties of PMMA

Thermo-physical Property	Value
Glass transition temp	105℃
Melting point	NA
Molecular formulae	$(C_5O_2H_8)_n$
Density	1.2 g/cm^3

(Source:IDEMAT 2003)

High impact polystyrene (HIPS)

HIPS is used to manufacture a large variety of objects, ranging from plastic cups to refrigerator chambers (Albright, 1972). The difference between HIPS and polystyrene is the addition of synthetic rubber (4-12%), which improves its tensile strength. HIPS is also more ductile and resistant in comparison to polystyrene (F.R. Cunha et al, 2013). In 3D printing HIPS is appealing because it behaves similarly to ABS. HIPS bonds well with ABS and dissolves in limonene, whereas, ABS does not, making HIPS a possible support material for ABS prints.

Jelčić & Ranogajec (2012) investigated the modification of HIPS by irradiation with γ- rays at the 1 MGy level. They found that tensile strength decreased initially and then recover at approximately 200 kGy. Tensile strength then increased linearly then from 500 kGy to 1 Mgy, resulting in an overall increase to tensile strength by 20%. This change, although an increase overall, does suggest that HIPS may not have the stability to be used as a bolus material. Additionally, something that might also impact its use in radiation therapy, due to charge storage, is HIPS's charging and discharging times, which were also found to change in response to accumulated dose.

The radiation absorption and scattering properties of HIPS are unknown but as it is chemically quite similar to both polystyrene and ABS, near water equivalence would not be unreasonable. On a practical side using HIPS as a dissolvable support with bolus would be advantageous.

Table 1.4 Thermo-physical properties of HIPS

Thermo-physical Property	Value
Molecular formulae	$C_8H_8{\bullet}C_4H_6$
Density	1.04 g/cm^3

(Source:IDEMAT 2003)

Polyvinyl Alcohol (PVA)

PVA is a non-toxic synthetic polymer that is generally used as wood or paper glue. It is not synthesized directly from its monomer, as vinyl alcohol is unstable, but instead is usually converted to PVA by transesterification of polyvinylacetate with ethanol. The properties and exact molecular formulae of PVA will vary depending on the amount of ester groups that remain (*Ullmann's Encyclopedia of Industrial Chemistry*, 2003).

PVA has also been used as a 3D printer substrate and as it is water-soluble it is easily dissolved in warm water. It bonds well with PLA, making it an excellent candidate for use as a dissolvable support material with PLA.

Similarly to HIPS, the radiation properties of PLA are relatively unknown as it is not a material often used as a tissue substitute or any other applications in radiation therapy. Our interest in it is solely as a support material for PLA prints.

Table 1.5 Thermo-physical properties of PVA

Thermo-physical Property	Value
Molecular formulae	$CH_2CH(OH)$
Density	$1.19 - 1.31\ g/cm^3$

(Source:IDEMAT 2003)

Thermoplastic polyurethane (TPU)

TPU or as it is known by its trade name, "Ninja flex", is a 3D printable elastomers which is formed from a reaction of 3 compounds: diisocyanates, short-chain diols and long-chain diols. However, the ratios of each vary depending on the desired properties of the resulting TPU.

Its flexibility makes it unsuitable for many applications but it could be beneficial in deformable motion phantoms or as a deformable bolus material to minimise air gaps. A careful analysis of the intra-fraction reproducibility would need to be carried out.

This list is in no way exhaustive but is simply of those used in this project. New materials reach the market regularly that could have properties suitable for use as tissue substitute or other application in radiation therapy. Leary, et al (2015) recently expounded the need to experimentally quantify the radiation properties of commercially available 3D printing substrates. The radiation property data for commercially available 3D printing substrates is not well reported in the literature and such information will be fundamental in promoting development of 3D printing within the radiation

therapy field. Therefore there exists an opportunity to quantify the data. This project will ascertain the relative radiological response of a range of candidate materials

2 Materials and Methods

The materials used throughout this project will be described in section 2.1 and section 2.2. Section 2.1 describes the two 3D printers that were used in the investigation and section 2.2 describes that sample blocks that were produced and the printer settings used.

The current work consists of a series of investigations that evaluate 3D printed materials for the production of clinical bolus. The methodologies reflect this by consisting of six main sections, one for each investigation. The same format will then be carried through to the Chapter 3 Results and Discussion.

Section 2.3 describes the preliminary investigations, bringing to light any unforeseen problems or flaws before further investigations were carried out. As such, the preliminary investigations identified possible issues with our methodology allowing us to refine the methods and investigate new possibilities in this up and coming field. Section 2.4 describes methods used to estimate the tissue equivalence of common 3D materials based on their electron density. The CT properties of the same 3D printed materials were measured in section 2.5 to provide another more clinically relevant estimate of their electron density. Narrow beam attenuation coefficients of the blocks were then measured in section 2.6. PDDs were measured next in section 2.7, which offers an illustrative description of the deposition of dose within a phantom under full scatter conditions. Then finally, in section 2.8, an example of a clinical bolus was produced and the effect it had on the dose distribution within the patient was measured.

2.1 Description of Printers

Two printers were used during our investigation; a custom made RepRap printer, referred to as the MDFstrap, and the RepRap Industrial manufactured by Kühling&Kühling.

The MDFstrap was the personal project of a staff member who based the design on a Mendel/Prusa type geometry in which the bed is belt driven, moving in X and Y directions and the extruder is raised by dual threaded rods. It originally had two standard 0.3 mm J-Head hot ends but these were later upgraded to dual high temperature (300°C) E3D hot ends that had exchangeable nozzle sizes (0.35 and 0.5 mm). It features a heated glass bed and print volume of 225 mm (L) by 245 mm (W) by 270 mm (H).

The RepRap Industrial is a Cartesian style printer consisting of a belt driven H-frame which controls movements of the extruder in the X/Y axis. A screw driven print table controls the Z-axis. With this

setup there is a maximum printable geometry of 800 mm (L) by 600 mm (W) by 800 mm (H) all housed within a chamber that can be heated to 70℃. The resolution of the extruder movements is determined by the minimal step width of each axis, which for the RepRap Industrial is X=0.028 mm, Y=0.019, Z=0.003 mm.

The printer supports two high temperature extruders (up to 300ºC) that can be used individually or in combination to provide two colours, nozzle sizes or materials. The use of two materials creates an opportunity to produce objects that require support material but also require an accurate finish that cannot be achieved with breakaway supports. By selectively dissolving one of the materials away only the desired object is left, unaffected by the removal process.

Nozzles of 0.5 and 0.75 mm bore diameter were used. The 0.5 mm nozzle was used to print in ABS and PLA but was unable to print PMMA, so the larger 0.75 mm nozzle was used.

As stock, the printer has a PEI/glass fabric/carbon composite sheet as a print surface that could be heated up to 120°C to aid adhesion of the hot filament to the print surface. After limited use, it was found that the composite sheets bowed and the print quality was adversely affected. A glass plate was then trialled and was found to improve print quality and therefore replaced the composite for the remainder of the investigations.

To print an object there are a number of steps that need to be taken. First the object needs to be defined in CAD software (Sketchup, by Trimble). It is then exported as a stereolithographic (STL) file with an extension developed by the “Sketchup Team”.

The STL is then used by Slic3r to determine how to modulate position, velocity, temperature and extrusion velocity to create the object. It creates instructions in the form of Gcode based on the printer specifications inputted by the user, such as print dimensions, nozzle size and layer height. Slic3r then divides the model into horizontal layers based on the inputted layer height and uses the nozzle width, the number of perimeters and the infill pattern to create the desired cross section. The 3D printer then uses the Gcode to print the desired object.

2.2 Description of Blocks

As there was very little published literature about 3D printing in radiation therapy in the initial phase of the project, the 3D printing settings that influenced radiation characteristics were investigated. While it had already been shown by Madamesila et al. (2015) that fill density would be influential, it had not been determined what effect different slicing software packages have on the attenuation properties due to the different levels of access allowed to various parameters. For example some

software packages only had very coarse settings for infill amount and didn't have the possibility of printing 100% fill.

For the initial investigations, the preliminary investigation and CT which are described in section 2.3 and 2.5 respectively, 5x5 cm 3D printed blocks with thickness of 1 cm and 2 cm were printed, including blocks of white ABS, white HIPS, black PLA and black TPU. An ABS block with a fill density of 75% was also measured to provide an indication of the effect of fill density on attenuation.

When ABS was printed on the MDFstrap the print temperature for ABS varied from 220 – 240℃, and the nozzle width was either 0.35 or 0.45 mm. On the K&K the nozzle width was either 0.35 or 0.5 mm and layer height was 0.25 mm. The print temp was 260℃, while the chamber temp was set at 70℃ and bed was at 100℃.

For use in the Attenuation and PDD measurements, described in 2.6 and 2.7 respectively, a new set of blocks were printed with well specified properties defined in Table 2.1. These settings were also used to print the example of clinical bolus, described in section 2.8.

The three materials, white ABS, black PLA and natural PMMA, were used to create 19 blocks (6 ABS, 6 PLA and 7 PMMA). Table 2. provides a summary to review the relevant physical characteristics of each of the materials. The blocks were constructed from a CAD generated STL file defining a block of material with dimensions 70 x 70 mm. The other dimension varied in thickness with one each of 1 mm, 2 mm, 3 mm, 5 mm, 10 mm and 20 mm being printed. By using different combinations of this set of blocks, measurements from 1 mm to 41 mm in 1 mm steps are possible. Due to significant warping, the 10 and 20 mm blocks of PMMA were unable to be printed. Instead four 5 mm blocks were printed, reducing the total thickness achievable by adding all the blocks together from 41 mm to 31 mm. Where possible the minimum number of blocks were used to achieve a certain depth. This created a pattern in the order of the blocks which was repeated for each plastic.

Where it was possible, the same settings were used for each of the different materials, excluding extrusion temperature. This was largely achieved with PLA and ABS; where the only things that had to be changed were the nozzle temperature and the bed temperature to aid adhesion for ABS. With PMMA the nozzle size was also changed, as even at the hottest temperature it was still not possible to get constant extrusion with the 0.5 mm nozzle.

The density (g/cm^3) of each sample was calculated by measuring the sample weight in grams using Fuzion FR-150 Professional digital mini scales and the sample volume (cm^3) using a digital Vernier Calliper.

Table 2.1. Standardised print settings used for those blocks printed for use in the attenuation and PDD investigations.

Kuehling and Kuehling Industrial RepRap

Filament			
Type	PLA	ABS	PMMA
Brand	Diamond Age	Diamond Age	Custom
Colour	Black	White (batch 1-2 (3mm)	Natural
Batch	Batch 1: 1,2,3,5,20 mm Batch 2: 10mm	Batch 1: 2,5 mm Batch 2: 1,3,10,20mm	Batch 1:1,2,3,5(1),5(2) Batch 2:5(3),5(4)
Diameter	2.9 mm (3.0mm nominal)	2.85 mm (3.0mm nominal)	3.0mm nominal

Slic3r settings (ver. 1.29)

Layer Height	0.25 mm		
Bed Temperature	60℃	100	
Extruder Temperature	220℃	260℃	280-295℃
Chamber Temperature	Room Temp	70	
Nozzle diameter	0.5		0.75
Layer speed perimeters	20 mm/s	25mm/s	25mm/s
Layer speed infill	30 mm/s		15-30 mm/s
Fill density	100%		
Fill pattern	Rectilinear		
Fill angle	45º		
Number of Perimeter	2		
Extrusion multiplier	1.0		
Z offset	0 mm		

First Layer

Bed Temp	65℃	100℃	
Extruder Temp	225℃	260℃	280-295℃
Layer Height	0.25		
Extrusion width	0.75		
Layer speed	15mm/s		
Skirts	1	0	2

Advanced

Retraction	1.5mm		0-0.5mm
Z lift	0mm		
Retraction Speed	24 mm/s		
Extra length on restart	0mm		
Seam	Nearest		
wipe while retracting	Inactive		
Retract on layer change	Inactive		
Overlap	15% (default)		
Slicer resolution	0 (default)		
Drive gear tension	0.4mm	0.48mm	0.2-0.3
Retract only when crossing perimeters	Inactive		

Extrusion widths

Infill extrusion width	0.5mm	0.75
Perimeter Extrusion width	0.5mm (external)	0.75
Top and bottom thickness	1 layer	

Table 2.2. Physical Properties of 3D printed plastics

Physical Property	White - ABS	Black - PLA	Natural PMMA	- Water
Chemical formula	$C_8H_8•C_4H_6•C_3H_3N$	$C_3H_4O_2$	$C_5H_8O_2$	H_2O
Physical Density	1.060-1.080 $g·cm^{-3}$	1.210–1.430 $g·cm^{-3}$	1.18 $g·cm^{-3}$	1 $g·cm^{-3}$
Effective Z*	3.45	4.36	3.74	3.33

* Effective Z calculated based on a 6MV LINAC spectrum weighted average using method developed by Taylor, Smith, Dossing, & Franich (2012)

2.3 Preliminary investigation to estimate water equivalence

The aim of this investigation was to estimate the water equivalence of a range of 3D printed materials using TMRs, which were described briefly in section 1.2.3.

A cylindrical chamber (CC13, active volume 0.3 cm^3) (IBA Dosimetry GmbH, Schwarzenbruck, Germany) was placed at the centre of a custom 2 cm sheet of Gammex solid water and positioned at the isocenter of the LINAC.

The TMR for gammex solid water was measured by placing 30 cm x 30 cm sheets in combinations to create depths from 2 mm to 3 cm on top of the custom 2 cm sheet which housed the cylindrical chamber.

100 MU of both 6 MV and 10 MV photons were then delivered to the sheets using a 4x4 cm^2 field size. The number of MU is a compromise between the amount of signal required and the amount of

time required to make the measurements. The longer the measurements take, the more temperature and pressure can vary causing slight deviations in the results.

By replacing the sheets of Gammex solid water with 5x5x2 cm 3D printed plastic blocks centred above the chamber, as depicted in Figure 2.13, point dose measurements were taken for a range of 3D printed materials; ABS, PLA, TPU, PVA, and HIPS. A measurement was also made for ABS printed with a 75% fill setting. Point dose measurements were also made for 5x5x1 cm blocks of ABS, PLA and TPU.

Using the TMR curve, measured in solid water, the depth of solid water required to achieve the same point dose was that achieved in the 1 and 2 cm 3D printed blocks was determined. By linearly interpolating between the two closest dose measurements on the TMR curve the equivalent depth could be determined.

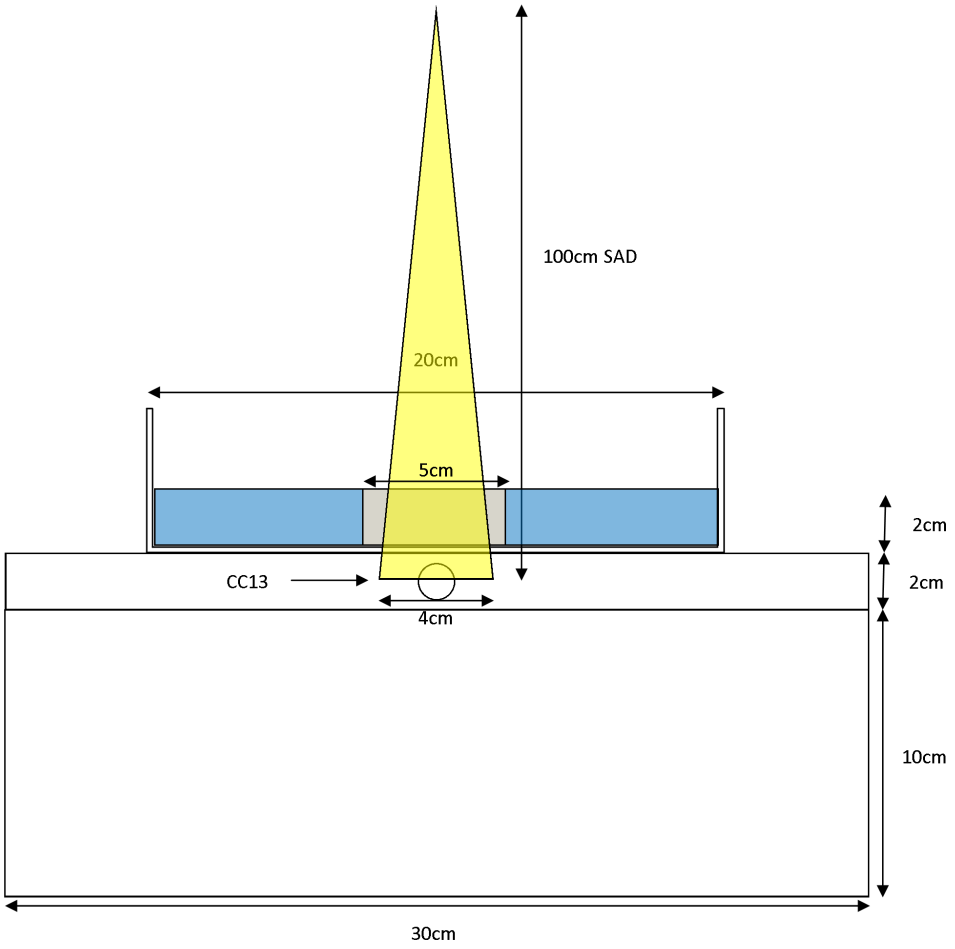

Figure 2.13. Experimental schematic illustrating the beam arrangement and the geometric relationship between the sample blocks, the 10cm of solid water used as back scatter and the water container that was used when determining if the dimension of the blocks was appropriate. CC13 was placed in a custom 2 cm thick sheet of solid water that had a void the shape of the chamber milled out of it. A 4 x 4 cm^2 field size photon beam was delivered with the gantry at 0°.

While Gammex solid water is designed to have radiation interaction properties that are matched to water, it is the TMR of solid water, not water, being used to measure water equivalence. Accordingly, it could be thought that it is the solid water equivalence is being determined. This means that it could slightly differ to that of water but it would still be indicative of true water equivalence.

It wasn't known if these 5x5 cm blocks provided sufficient lateral scatter to establish charged particle equilibrium when only 5 mm of material was left around the edge when used with a 4x4 cm^2 field size. To determine the impact of the missing lateral scatter, measurements using the 5x5x2 cm blocks were compared to measurements under the same conditions with 7x7x2 cm blocks. The same 5x5x2 cm blocks were then placed in a 27x20 cm container (as shown in Figure 2.13) which was filled with water to the level of the blocks and these measurements were compared with the original 5x5x2 cm block measurements.

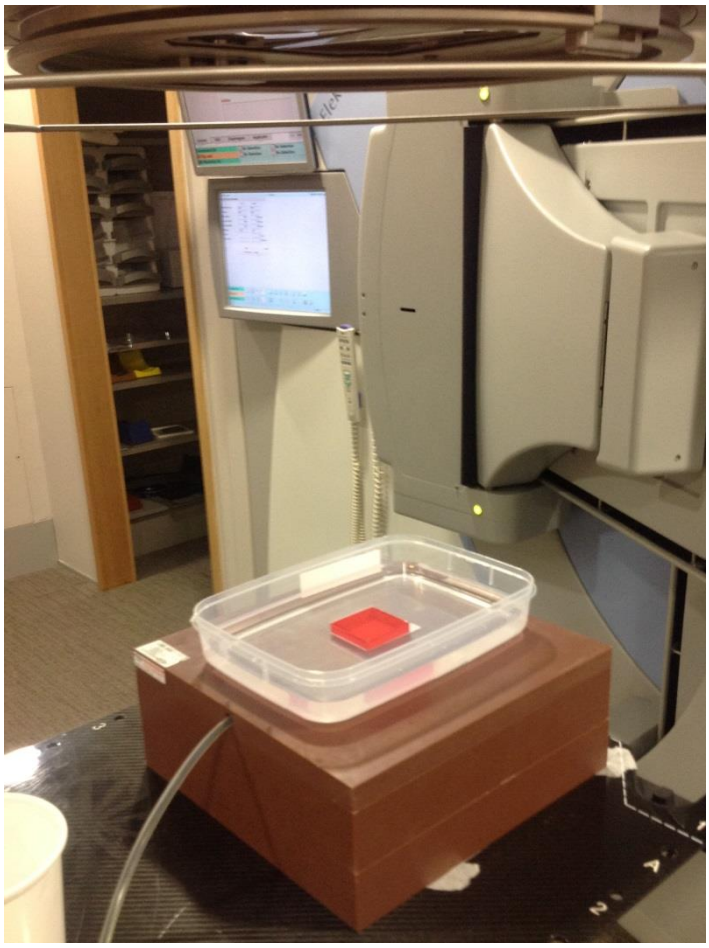

Figure 2.14. Photo of the the beam arrangement and the geometric relationship between the sample blocks, the 10cm of solid water used as back scatter and the water container that was used when determining if the dimension of the blocks was appropriate. The cable for CC13 is visible leading into its custom 2 cm thick sheet of solid. A 4 x 4 cm^2 field size photon beam was delivered with the gantry at 0°.

A hollow 3D printed cube, also 5x5x2 cm, was filled with water and measured, so that the above measurements could be related directly with water, rather than solely Gammex solid water, as shown in figure Figure 2.14. A comparison between the printers was made using two 5x5x2 cm blocks printed in the same PLA filament, one printed on the K&K the other on the MDF strap. Additional 5x5x2 cm blocks were also requested and received from external parties. An ABS block printed on the Qubea printer, a delta styled Reprap based printer, a block from Ultimaker that is believed to be PLA that was printed at 0.02 mm layer height, and a 4.4x4.4x1.8 cm block printed on a Stratsys Object 30 pro, a commercial inkjet printer, made of Vero Gray.

2.4 Depth Scaling Factors

To determine their relative water equivalence and therefore their suitability for use as tissue substitutes in 6 and 10 MV photon beams, the depth scaling factors for ABS, PLA and PMMA were calculated. The photon interaction that largely dominates between 100 KV and 10 MV is the Compton Effect which, as previously described in section 1.2.2, is dependent on the electron density (ED) which is a measure of the number of atomic electrons per cm^2. This can be calculated for water using:

$$ED = d_w N_A \rho_w \overline{\left(\frac{Z}{A}\right)}_w \tag{2.1}$$

here N_A = Avogadro's constant, ρ_w = density of water and

$$\overline{\left(\frac{Z}{A}\right)}_w = f_1 \left(\frac{Z}{A}\right)_1 + f_2 \left(\frac{Z}{A}\right)_2 \ldots \tag{2.2}$$

where f_i is the fractional weight of each element (indicated by the subscript) and $\left(\frac{Z}{A}\right)_i$ is the ratio of the atomic number and the atomic mass of each element.

Assuming that only Compton interactions are occurring, two materials would have equivalent photon attenuation properties if they have equal numbers of atomic electrons per cm^2.

$$ED_w = ED_p = d_w N_A \rho_w \overline{\left(\frac{Z}{A}\right)}_w = d_p N_A \rho_p \overline{\left(\frac{Z}{A}\right)}_p \tag{2.27}$$

Where the subscript w and p indicates the components that relate to water and plastics respectively. By rearranging the depths d_p and d_w into a ratio, the depth scaling factor $\frac{d_p}{d_w}$ can be written as,

$$\frac{d_p}{d_w} = \frac{\rho_w \overline{\left(\frac{Z}{A}\right)}_w}{\rho_p \overline{\left(\frac{Z}{A}\right)}_p} \tag{2.28}$$

The ABS, PLA and PMMA blocks used for this investigation were described in section 2.2. The density of each was able to be physically measured. The density of the 3D printable plastics was calculated as a weighted average based on the exact dimensions of the blocks to allow for comparisons. The density (ρ) used was,

$$\rho = \frac{\sum_i \rho_i \cdot Z_i}{\sum_j Z_j} \tag{2.29}$$

where, the sum of the densities of each block in the series weighted by their respective exact z dimension $(\sum_i \rho_i \cdot Z_i)$, which is then divided by the sum of the exact z dimensions of the entire series $(\sum_j Z_j)$.

For all materials except solid water, which when purchased is supplied with elemental fractional weight, the elemental composition was assumed based on the chemical formulae. For both ABS and HIPS the exact ratio of the constituent elements is not known, but variations of the ratios were explored to give a range of expected electron densities.

2.5 CT

The aim of this work was to determine the average CT number of both materials commonly used in FDM printing and those more widely used in radiation therapy but less commonly used in FDM printing. The homogeneity of the 3D printed materials was also able to be investigated using CT

The impact of difference filament manufactures were investigated, using ABS produced by K&K, Diamond Age and Hobbyist. The impact of the additives used to achieve different colours in PLA were also examined.

CT scanning was performed using a Philips Brilliance with the “Small Pet” CT protocol (exposure of 92 mAs, peak voltage 120 kV, slice thickness 0.8 mm, rotation time 0.75 s and field of view of 18.9 cm. The CT was taken while the samples were in air, and in direct contact with the treatment couch surface. The CT images were then stored in DICOM format and imported into the treatment planning system, Elekta’s MonacoSim, for CT number measurement, visual inspection and analysis.

2.5.1 Data analysis

By contouring a slice at either end of the sample in MonacoSim and interpolating in between them, the volumes of the samples were defined. Similar to the method used Bibb, Thompson, & Winder,

(2011), pixels at the edges of the sample images were excluded from the contour by shrinking them geometrically by 1mm to avoid both the partial volume effect which would lower the average CT number and the higher density shell around some blocks, which would artificially raise the average CT number . The mean and standard deviation (SD) of the CT numbers for each sample were recorded using MonacoSim's data analysis tools. By averaging over the contoured volume of the sample it ensures that the measure is representative of the whole sample.

2.5.2 Uniformity

To measure uniformity the average and standard deviation of the mean values were then taken. A screenshot was taken with the window level set as the mean and the window set to four times the standard deviation.

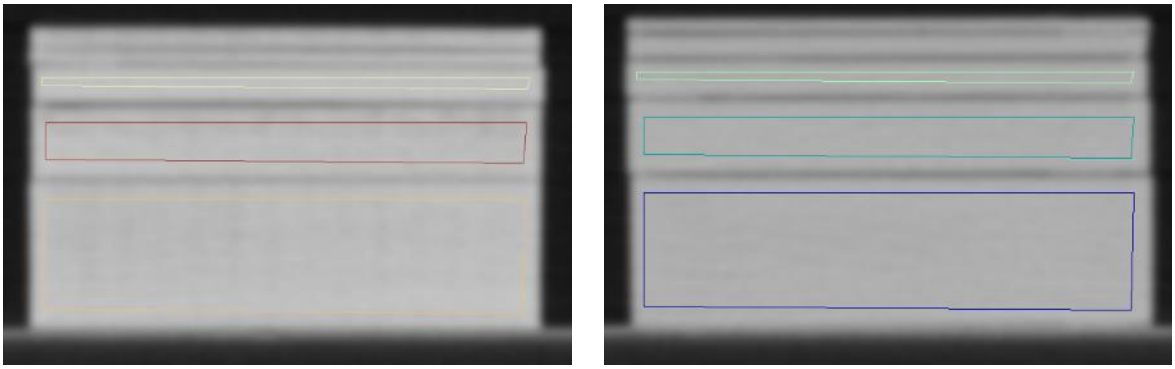

(1) **(2)**

Figure 2.15. (1) PLA, (2) ABS, both illustrate the regions used for analysis , used a 0.1cm shrink margin – displayed in the lung pre-set (1700/-300 W/L) . Can see some of the patterning on the PLA but ABS looks homogenous.

2.6 Attenuation

This work presents a method of determining the total mass linear attenuation coefficients in poly-energetic LINAC beams for potential 3D printed bolus materials.

By rearranging the Beer-Lambert Law and adding an additional term for the attenuation of air, the following equation can be reached,

$$\mu(E) = -\frac{1}{t}\ln\left(\frac{\Phi_t(t)}{\Phi_0(t)}\right) - \frac{(x_1 + x_2)}{t}\mu_{air}(E) \tag{2.30}$$

where $\Phi_0(t)$ is the photon flux in the reference spectrum $\Phi_t(t)$ is the photon flux in the attenuated spectrum $\mu_{air}(E)$ is the linear attenuation coefficient for air, x_1 is the distance between the source and the sample (100 cm), x_2 is the distance between the sample and the detector (150 cm) and t is the sample thickness.

Although the linear attenuation coefficient of air is similar to that of the samples, the density of air is 1/1000 of the density of the samples, which means that the attenuation due to air will be insignificant compared with the measurement error.

All measurements were performed with beam matched Elekta Synergy linear accelerators with poly-energetic 6 MV beams. The LINAC gantry was rotated to 90^{o} to allow positioning of the chamber and collimating system on the treatment bed when it is also rotated to 90^{o}.

Narrow beam conditions were established using two collimating systems, as depicted in Figure 2.. The first collimating system used was the MLC and Jaws to deliver a 1x1 cm field size, 100 cm from the source. The most distant part of the first collimating system is the Y diaphragms at 50.9 cm from the source with the MLCs being the closest at 29.8 cm. The second collimating system consisted of two layers of 5 cm thick lead bricks, aligned to the centre of the arrangement using the in-room laser system to be perpendicular to the beam. The bricks were arranged to only allow a 1 cm square through at 100 cm from the source (at the isocentre).

The reference intensity $\Phi_0(\mathrm{t})$ was measured by placing a compact ion chamber (CC04, active volume 0.04 cm^3) (IBA Dosimetry GmbH, Schwarzenbruck, Germany) 250 cm from the source when there was no sample in the beam. By adding the sample into the beam, the attenuated intensity(t) was measured. Any photons scattered by the absorber were not supposed to be measured in this arrangement. This is why the detector was placed 150 cm away from the sample so that only the primary photons, photons that passed through the absorber without interacting, were measured. Thus, if a photon interacts with an atom, it is either completely absorbed or scattered away from the detector (Khan, 2010).

Since the LINAC spectrum is continuous and the Beer-Lambert law requires a mono- energetic beam, the effective energy of the poly-energetic 6 MV beam needed to be determined. By rearranging the Beer-Lambert law for $\mu(\bar{E})$ the following can be reached,

$$\mu(\bar{E}) = -\frac{\ln\frac{\Phi_t(\mathrm{t})}{\Phi_0(\mathrm{t})}}{x} \tag{2.3}$$

Using water as a reference material, its linear attenuation coefficient was calculated using Equation 2.6 for the LINAC's poly-energetic 6 MV beam. The energy of a mono-energetic photon beam that is attenuated by water at the same rate was then found using National Institute of Standards and Technology's (NIST) Xcom database and used as the effective energy $(\bar{E})$ of the poly-energetic 6 MV beam.

To determine the ratio of $\Phi_t(\mathrm{t})/\Phi_0(\mathrm{t})$ for water, it was suggested by Hill, Brown, & Baldock (2008) that the water container used for the $\Phi_t(\mathrm{t})$ measurement also be included in the $\Phi_0(\mathrm{t})$ measurement. This would reduce the effect of the walls, however the attenuation in the walls would also cause a shift in the energy spectrum of the beam, causing an underestimate of the effective energy.

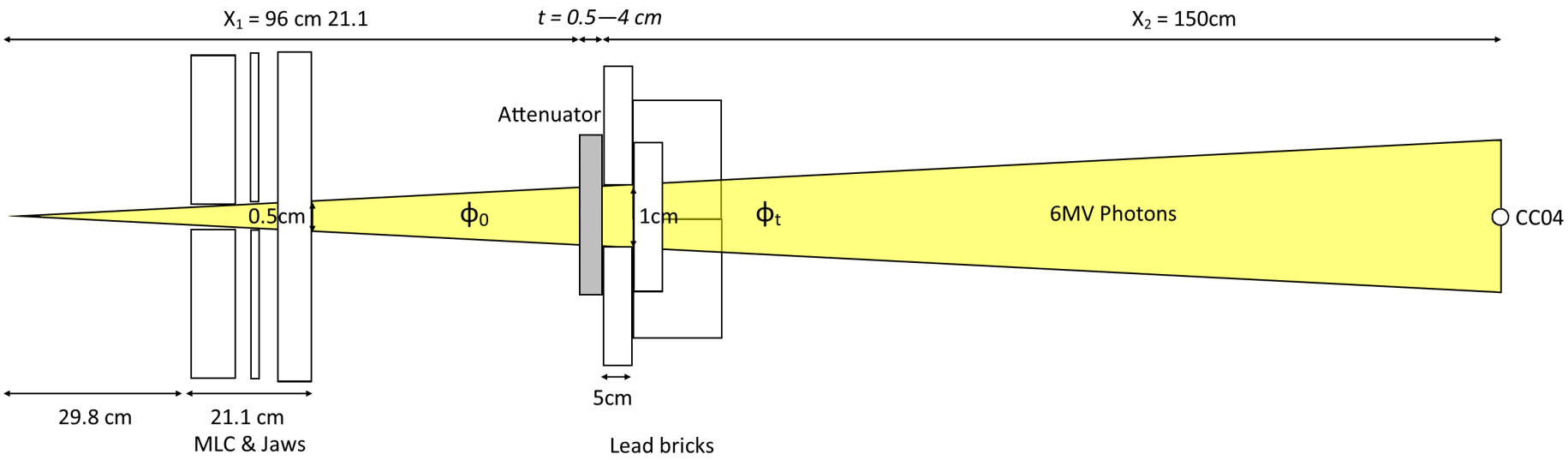

Figure 2.1. Shows the experimental setup illustrating the placement of the attenuating materials, the arrangement of the lead brick collimator and the ion chamber. The LINAC would be just out of frame to the left.

Therefore, when determining the initial intensity measurements$(\Phi_0(t))$, which were taken in the same narrow beam conditions depicted in Figure 2., the empty PLA container, with 1.74 mm thick walls (two layers thick), was included in the beam. The PLA container was then filled with water for the $\Phi_t(t)$ measurement and the distance between the container walls (4.83 cm) then defined the path length (x) of the beam.

The 3D printed blocks described in 2.2 were then placed between the two collimators, flush against the lead brick collimator. As it was suspected that transmission through the blocks may exhibit an anisotropic effect, due to the alignment of filament as it was laid down during printing, all the blocks except for the PLA water container beam axis was aligned with the Z printing axis (height) using the in-room laser system and were centred using the projected light field from the LINAC.

$$\mu(E) = -\frac{1}{t}\ln\left(\frac{\Phi_t(t)}{\Phi_0(t)}\right) \tag{2.4}$$

To obtain the mass attenuation coefficient, the transmission intensity was plotted against the path length and the exponential fitting parameter was determined by minimising the least squares difference using the Generalized Reduced Gradient (GRG2) code. The GRG2 code reduces the original problem into a sequence of reduced problems which are then solved by the gradient method using a variant of Newton's method (Lasdon, Waren, Jain, & Ratner, 1976).

$$\Phi(t)/\Phi_0(t) = e^{-\mu t} \tag{2.5}$$

The equation of the fit, which would be in the form of equation 2., can then be output with the linear attenuation coefficient being the coefficient in the exponential. The linear attenuation coefficient was divided by the weighted average density to calculate the mass attenuation coefficient; this compensated for the slightly different densities in each block.

Once again, without the exact fractional elemental composition it is not possible to compare the measurements from the above investigations to those previously measured or predicted.

2.7 PDDs

As introduced in section 1.3.2, for the clinical use of bolus, the effect of the material on the dose distribution needs to be determined. In this section percentage depth dose values will be measured, illustrating the importance of scattered radiation. The effective linear attenuation coefficients discussed in the last section were assumed to be scatter free as they were under narrow beam geometry. Percentage depth dose distributions were measured in three 3D printed plastics; white ABS,

black PLA and clear PMMA, whose production was described in section 2.2. The 7×7 cm blocks were used in combination to test depths from 1 mm to 40 mm.

The PDDs were measured using a plane-parallel ion chamber (PPC40, active volume 0.4 cm^3) (IBA Dosimetry GmbH, Schwarzenbruck, Germany) placed in a custom 2 cm thick sheet of Gammex solid water that has had a void milled into it specifically for the PPC40. The custom sheet of Gammex solid water was then placed on top of another 8 cm of Gammex solid water to provide back scatter. PPC40 was used to minimise transmission through any medium apart from the sample of interest. The 1 mm PMMA chamber window on PPC40 was taken into consideration.

100 MUs were delivered using 6 MV and 10 MV photon beams with a field size of 5×5 cm from an Elekta synergy with an MLCi. The 7×7 cm blocks were then placed on top and an SSD of 100 cm was maintained with the surface of the plastic blocks. Initially for PLA and ABS the optical distance indicator was used to determine SSD. For PMMA the front pointer was used to set the SSD. For both PLA and PMMA the digital readout on the couch was used to verify the couch movements.

The measurements were then compared to measurements made in water and PDDs determined using two different treatment planning systems, Monaco and XiO. The treatment planning systems calculated the PDDs using CT scans of the plastics in the same position used to measure the PDDs. This generated a comparison between the measured values and how it would be simulated clinically.

The differences between the measurements were quantified by summing the square of the difference between each measurement in the plastic and a point interpolated directly beneath but between the two nearest points on the water curve smoothed with a 5 point mean filter. An evolutionary solving method, which uses a variety of genetic algorithms and local search methods developed by Frontline Systems, Inc, was used to adjust the depth scale and the depth offset, minimising the sum of the differences between each of the plastics and the smoothed water curve. This allows the PDD results to be compared to the depth scaling results determined earlier. This process was adapted from vertical least squares fitting

The scale factor was restricted to values between 0.8 and 1.2 as values outside of this range would not be likely to reduce the difference. The depth shift was limited between –2 mm and +2 mm as outside of this range would also not be likely to reduce the difference.

2.8 An example of clinical bolus

In this section a 3D printed bolus will be evaluated and compared with the more common bolus materials wax and Superflab. By comparing the dose distributions produced in the patient using radiochromic film measurements in transverse plan, the effect the bolus materials had on dose

distribution was quantified. The film dose measurements were then compared to the dose distributions calculated within the treatment planning system (Monaco and XiO).

An anthropomorphic RANDO phantom (The Phantom Laboratory, Salem NY), as shown in Figure 2.16 was used to carry out dosimetric measurements. The RANDO phantom consists of a series of transverse slabs held together by two rods that run the length of the phantom. Film was placed in the gap between the slabs that meet in the same plane as the tip of the RANDO phantoms nose. The RANDO phantom will be referred to as 'the patient' in the following description.

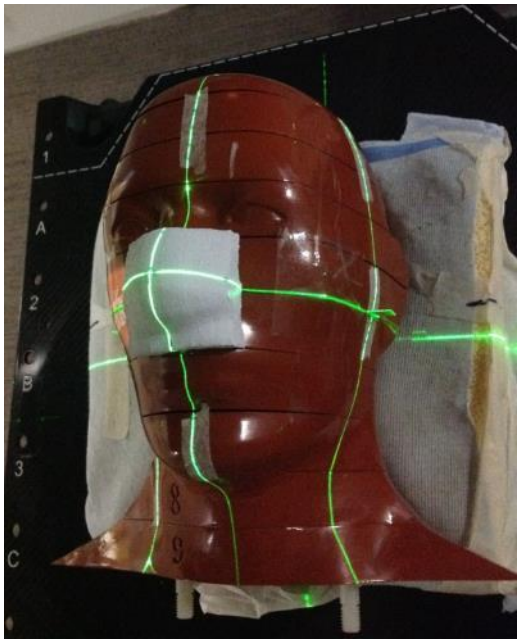

Figure 2.16. The head portion of the RANDO phantom aligned in the treatment position with the 3D printed bolus and film in place, only the tabs are visible

2.8.1 3D-printed bolus design

A bolus was designed using CT images of the patient that were acquired on a Philips big bore scanner and then imported into a treatment planning system (MonacoSim). An external patient contour was generated using the auto threshold tool with the soft tissue pre-set, and a 5x5 cm region centred on the patient's nose was defined. The bolus tool within MonacoSim was then used to generate a structure that was a 1 cm expansion from the patient's surface. The CT data and the bolus structure were then exported from MonacoSim into Slicer. Slicer is an open source tool for the analysis and visualisation of medical images. With the addition of the RT module it is able to import DICOM structures which consist of a series of contours. Slicer creates a ribbon model from the contour which was transformed into a closed surface model and then exported as an STL file.

MeshLab was then used to smooth the bolus using a Laplacian smooth function with 1D boundary smoothing and cotangent weighting active. The Laplacian smooth function calculates a new vertex position based on the average position of the nearest vertices. This process was iterated 9 times before the bolus model was deemed acceptably smooth.

The STL file was then opened in Sketchup and 0.5 mm was trimmed off each of the side faces to remove extra material and create a reasonably flat edge. It was then exported as an STL file once again.

2.8.2 3D-printed bolus fabrication

It was decided that the bolus would be printed on its side to minimise overhang. Slic3r, the 3D printing software, then used the STL file to determine the Gcode for the printer.

The bolus was printed in ABS using all the standardised ABS settings described in section 2.2 except for layer height. A layer height of 0.1 mm was used to help with the overhang and gently changing contour in the Z direction. Although 0.5 mm was trimmed on each face to remove extra material, a raft was still needed to create a flat edge to aid adhesion.

2.8.3 Measurement

The patient was aligned in the treatment position using the in-room lasers, as shown in Figure 2.16. The in- room lasers are aligned to project the anatomical planes onto the patient to assist with patient set-up as illustrated in Figure 2.17. The patient was positioned such that the gap between transverse sections, which went through the centre of his nose, was aligned with the transverse laser plane. The sagittal laser plane was then aligned with the centre of the nose. The coronal laser plane was first aligned with the very tip of the patient's nose and then the patient was shifted 10 cm anteriorly to locate the coronal laser plane at a depth of 10 cm (90 cm SSD).Another CT scan was taken with the bolus positioned on the patient as shown in Figure 2.16 to evaluate the fit and generate the planning data required for the TPS. The position of the lasers was then marked on the 3D printed bolus to enable the reproduction of the setup alignment during "treatment".

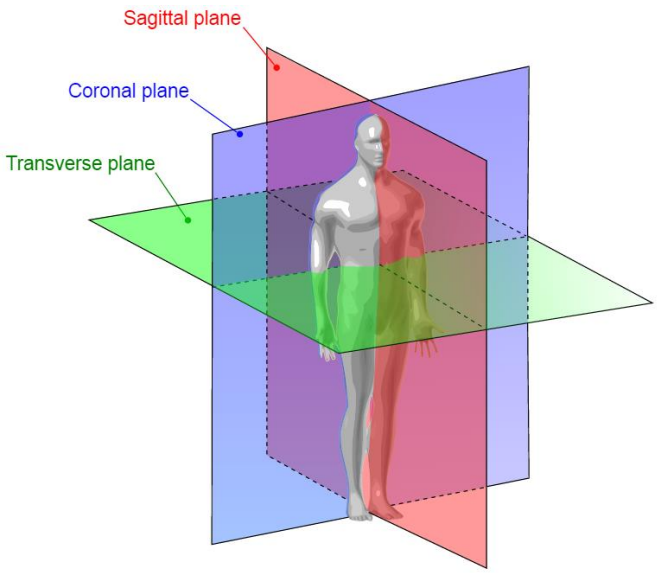

Figure 2.17. Illustrates the three basic anatomical planes. The sagittal plane is any imaginary plane parallel to the median plane, the transverse plane is any plane that divides the body into superior and inferior parts, roughly perpendicular to the spine and the coronal plane is any vertical plane that divides the body into anterior and posterior sections. Source: Boundless. "Body Planes and Sections." Boundless Anatomy and Physiology.

A CT scan was also taken with a wax bolus placed in the treatment position. The wax bolus was created using a 6x8 cm sheet of 1cm thick wax that was heated in a water bath until pliable. It was then draped over the nose area of the patient and was gently but rapidly shaped to the contours on the nose. After shaping, the resulting wax bolus was 6cm long in the sup-inf and 5cm in the left-right direction. The bolus could have been trimmed to be precisely 5x5 cm but the additional 0.5 cm at either end in the superior - inferior direction was deemed to be unlikely to have an effect on the dose measured in the plane of interest. Tape was applied to the surface of the wax bolus and the intersection with the lasers was marked to reproduce the setup alignment during treatment.

A 5.5x 10 cm sheet of 0.5 cm thick Superflab was also attached to the patient in the treatment position and a CT scan taken. Tape was used to deform and fix the Superflab into the contours of the nose. Markings were made on the Superflab to define the setup laser locations for reapplication during treatment. The tape used was also left attached so that deformation and fixation could be mimicked during treatment.

On the treatment planning system (Monaco or XiO) the CT scan of the patient was used to establish the patient geometry. The LINAC position specifications were then entered to match the setup described below, and the dose distribution within the patient was calculated. The dose plane that corresponded to the same transverse plane that the film was placed in was extracted. This was repeated using the CT of the patient, both with the bolus in position and without a bolus. The 3D printed bolus was also virtually defined using the structure generated by the bolus tool with an

Figure 2.18. Scan of the EBT3 gafchromic film used for the wax measurement, illustrating the shape and markings on the film. It is acknowledged that the image of the film is post irradiation,

electron density of 1.00 as we were unable to force it to another value.

Sheets of radiochromic film (EBT3 gafchromic film) were shaped to match the contour of the transverse cross section of the Rando phantom at the level of the nose and to avoid the two rods that run the length of the phantom, as shown in Figure 2.18.

Radiochromic film utilises radiation-sensitive organic microcrystal monomers dispersion coated on both sides of a thin polyester base with a transparent coating. The Colour of the film darkens with increasing absorbed dose and does not required processing to develop or fix the image (Blackwell et al., 1998).

The film was then inserted between the slices, flush with the outer surface, and markings were placed where the anterior laser and the two lateral lasers struck the film. These were used for alignment during the comparison.

The LINAC gantry was positioned at 0° to deliver 200 MU using a 4x4 cm field size 6 MV beam anteriorly to the patient in the aforementioned treatment alignment (90 cm SSD) without a bolus material. This was then repeated for each of the bolus materials, aligned in the same position they were in during their respective CT scans.

The films were then scanned on an Epson 10000 XL at 96 DPI with 48 bit colour as a positive film. RGB values were converted to absolute dose measurements using Radiological Imaging Technologies (RIT) film analysis software (version 6.3). Calibration films exposed to 7 different dose levels which were used to establish a calibration curve between signal from the red channel and absolute dose. A nine point median filter was then used to reduce the visible streaking artefact. It has been shown that the signal from the blue channel could be used to remove this streaking artefact but this method was yet to be implemented in our clinic.

The line rotate tool within RIT was used to align films using the marks illustrating the position of the sagittal lasers. As the anterior laser markings on the film were not discernible once scanned and imported into the RIT software, the full width half max at 5 cm was used to determine the middle of the profile. This point was then compared against the physical markings on the film to confirm the correct location of the profile.

3 Results and Discussion

In this section, the format used in the methods is continued with each of the 6 main results being presented and analysed in successive sections. An analysis of the experimental error is then presented in section 3.7.

3.1 Preliminary investigation to estimate water equivalence

In this section, the water equivalence results will first be presented and then discussed. The section is broken into two subsections based on which beam energy the results relate to.

3.1.1 6MV

In Figure 3.19 point dose measurements for various 5 x 5 x 2 cm 3D printed materials are compared with a TMR curve for solid water. The point dose measurements range from 0.969 to 0.990 which is equivalent to 2.23 and 1.54 cm respectively.

These results are also presented in Table 3.6, where the first column of Table 3.6 presents the point dose measurements for each of the 3D printed plastics and the water block as a percentage of the maximum dose measured in solid water. Columns 2 and 3 are the measured thicknesses of each block and their densities respectively. Even though the blocks were 2 cm thick (Z) when defined in the CAD design the blocks actually have thickness that varied by 0.5 mm. Column 4 presents the water equivalence (Z_{eq}) determined from the measured thickness of the 2 cm blocks. The fifth column is the ratio of the water equivalence and the actual thickness of the block (Z_{eq}/Z) where the number presented is the amount of solid water equal to 1 cm of each 3D printed material. The sixth column is the ratio from the water equivalence and the actual thickness and density ($Z\_eq/(Z \cdot \rho)$) of the respective blocks.

Referring to table 3.1 it is apparent that ABS had a point dose measurement that was 96.9% of the maximum dose recorded during the TMR. This point dose corresponds to an equivalent thickness of 2.23 cm of solid water, which is the largest value measured above the desired 2 cm. Adjusting for the actual thickness of the block, which was measured to be 1.94 cm, (Z_{eq}/Z) results in a solid water equivalence where 1 cm of ABS is equivalent to 1.15 cm of solid water. The density (ρ) was measured to be 1.02 g/cm^3 which is only 2% higher than 1, so the density scaling can be considered minor. The density adjusted water equivalence of 1 cm of ABS that had a density of 1 g/cm^3, would be equivalent to 1.13 cm of solid water. The measured water equivalence suggests that ABS would require depth scaling to achieve water equivalence. This was confirmed when adjusted for its actual thickness and density.

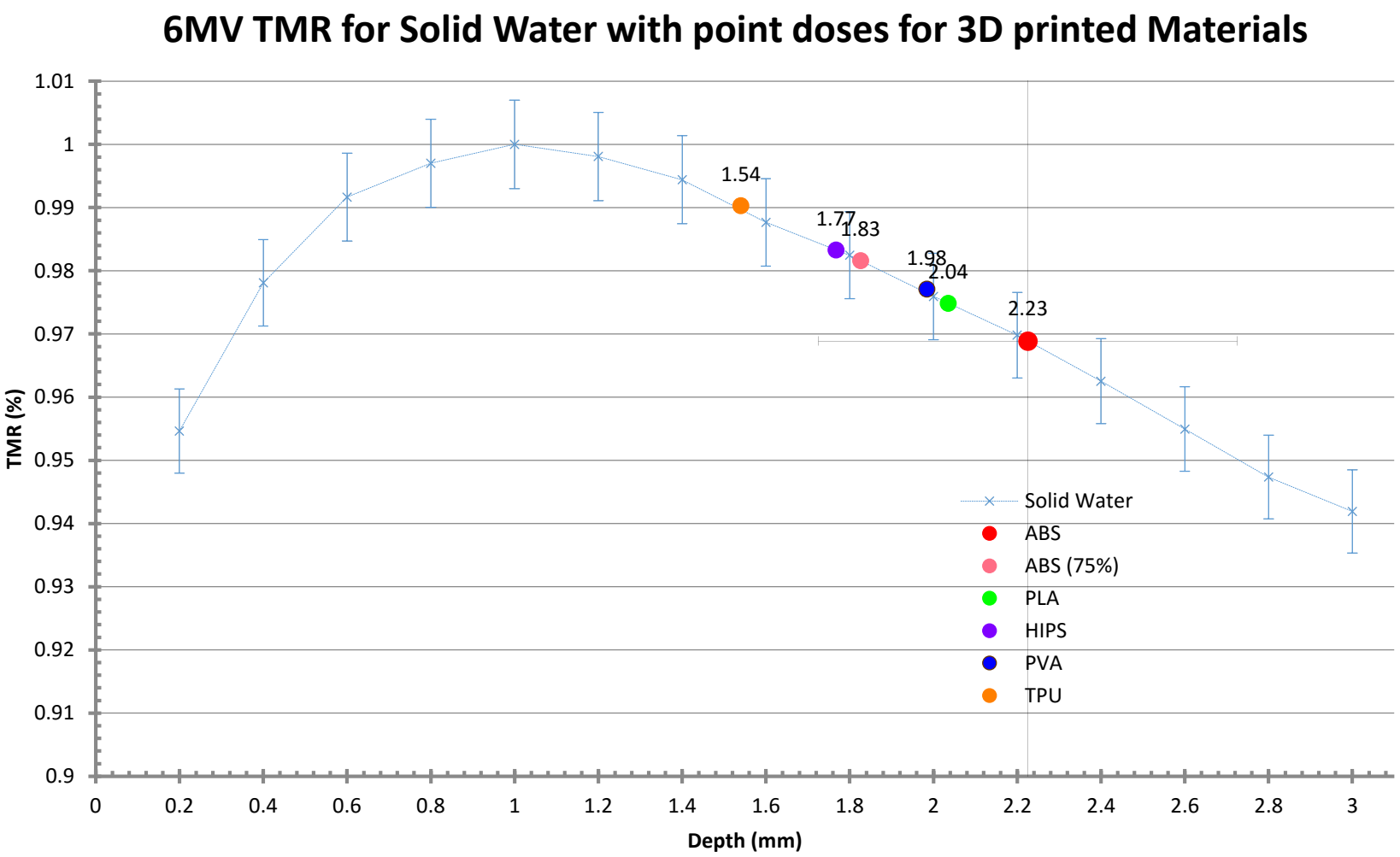

Figure 3.19. TMR curve using 6 MV photons in Gammex solid water with point doses for 3D printed Materials and 0.7% error bars displayed**.**

Table 3.6 Water equivalence of 2 cm 3D printed plastics blocks in a 6 MV beams.

Material	Pt Dose (%)	Z (cm)	ρ (g/cm^3)	Z_{eq} (cm)	Z_{eq}/Z	$Z_{eq}/Z \cdot \rho$
ABS	96.9	1.94	1.02	2.23	1.15	1.13
ABS (75%)	98.2	1.96	0.62	1.83	0.93	1.51
PLA	97.5	1.98	1.21	2.04	1.03	0.85
HIPS	98.3	1.94	0.78	1.77	0.91	1.17
PVA	97.7	2.00	1.17	1.98	0.99	0.85
TPU	99.0	1.99	0.97	1.54	0.77	0.80
Water	98.2	1.93	1.05	1.82	0.94	0.90

With a point dose measurement that was 98.2% of the maximum dose recorded during the TMR, decreasing the fill amount to 75% in ABS decreased the water equivalent thickness to 1.83 cm of solid water. Adjusting for the actual thickness of the block, which was measured to be 1.96 cm, (Z_{eq}/Z) resulted in a solid water equivalence where 1cm of ABS (75%) is only equivalent to 0.93 cm of solid water. Interestingly, when adjusted for density (ρ), which was measured to be 0.62 g/cm^3, the density adjusted water equivalence of 1 cm of ABS (75 %) that had a density of 1 g/cm^3 would be equivalent to 1.51 cm of solid water. The results of the ABS (75%) were as expected, with the reduction in the fill decreasing the density from 1.02 to 0.6 g/cm3. The water equivalence was also anticipated to decrease as it did, from 1.15 to 0.93 cm. When adjusted for density, the expectation was that both the 100% fill ABS and the 75% fill ABS would result in the same solid water equivalence. However, the density adjusted result for the 75% fill ABS was 1.51, whereas for the 100% fill ABS it was 1.13. These results are similar, but not identical as expected. They suggest that using density to correct the results could give an indication of the equivalence that could be achieved with optimal print settings, such as overlap and layer height.

PLA had a point dose measurement that was 97.5% of the maximum dose recorded during the TMR. This point dose corresponds to an equivalent thickness of 2.02 cm of solid water which was one of the closest values to 2 cm that was measured. Adjusting for the actual thickness of the block which was measured to be 1.98 cm, (Z_{eq}/Z) results in a solid water equivalence where 1cm of PLA is equivalent to 1.03 cm of solid water. The density (ρ) was measured to be 1.21 g/cm^3 which is much higher than 1, so the density scaling had a large impact. The density adjusted water equivalence of 1 cm of PLA that had a density of 1 g/cm^3 would be equivalent to 0.85 cm of solid water. In terms of raw measurements, PLA appeared to be closest to water equivalent and retains this equivalence even when adjusting for the actual thickness of the block. However, when adjusted for density, it seems to suggest that PLA is much denser than water. It seems the print settings used were near optimal for PLA to be a water equivalent material.

With a point dose measurement that was 98.3% of the maximum dose recorded during the TMR, 1.94 cm of HIPS was found to be equivalent to 1.77 cm of solid water. Adjusting for the actual thickness

results in a solid water equivalence where 1cm of HIPS is equivalent to 0.91 cm of solid water. Interestingly, when adjusted for density (ρ), which was measured to be 0.78 g/cm^3, the density adjusted water equivalence of 1 cm of HIPS that had a density of 1 g/cm^3 would be equivalent to 1.17 cm of solid water. HIPS has a similar composition to both ABS and polystyrene. As previously stated, both of these have been used as water equivalent phantom materials, therefore it was expected that HIPS would also be water equivalent. However, with 1 cm of HIPS being equal to 0.91 cm of solid water, HIPS is less attenuating than water. Further optimisation of the print settings for HIPS could result in an increase water equivalence.

PVA had a point dose measurement that was 97.7% of the maximum dose recorded during the TMR. This point dose corresponds to an equivalent thickness of 1.98 cm of solid water which was the closest value to 2 cm that was measured. The actual thickness of the block was measured to be 2.00 cm, (Z_{eq}/Z) resulting in a solid water equivalence where 1cm of PVA is equivalent to 0.99 cm of solid water. The density (ρ) was measured to be 1.17g/cm^3, which is much higher than 1, so the density scaling had a large impact. The density adjusted water equivalence of 1 cm of PVA that had a density of 1 g/cm^3 would be equivalent to 0.85 cm of solid water. With the current print settings, PVA is similar to solid water, making it a good substitute, but this is negated because PVA absorbs water which causes it to lose its structure. These absorbent properties make it a good support material for 3D prints, however for use as a bolus material it would require some sort of waterproofing, such as a lacquer coating or a plastic bag. These waterproofing solutions would require further investigations to determine their impact on the water equivalence of PVA.

TPU had a point dose measurement that was 99.0% of the maximum dose recorded during the TMR in solid water. This corresponded to an equivalent thickness of 1.99 cm of TPU being equal to 1.54 cm of solid water. With an actual thickness of 1.99 cm which is very close to the desired 2 cm, adjusting for the actual thickness Z, the Z_{eq}/Z result does not add much and 1cm of TPU is equivalent to 0.77 cm of solid water. This is the same for density (ρ), as the density was measured to be 0.97 g/cm^3 which is very close to 1, so the density scaling is also only very minor. The density adjusted water equivalence of 1 cm of TPU that had a density of 1 g/cm^3 was equivalent to 0.80 cm of solid water.

The water block had a point dose measurement that was 98.2% of the maximum dose recorded during the TMR in solid water. This corresponded to an equivalent thickness of 1.93 cm of water being equal to 1.82 cm of solid water. Taking Z_{eq}/Z results in 1cm of water being equivalent to 0.94 cm of solid water. By definition the density of water should be exactly 1 g/cm^3 however it was measured at was 1.05 g/cm^3. The density adjusted water equivalence of 1 cm of water that had a density of 1 g/cm^3 was equivalent to 0.90 cm of solid water. Correcting for density should not be required, however, the ABS container that the water was in appears to have affected the measurements. It was determined that when empty, the container itself had a point dose measurement that was 92.6% which corresponds to an

equivalent thickness of 0.07 cm of solid water. Due to the steep dose gradients near the surface, a much higher uncertainty in the equivalent thickness needs to be considered. This could explain the variation seen in the results of the water measurement. The non-water equivalence of the water block could be explained by the extra 4 layers of sparse plastic which was used to firmly attach it to the print bed. Although sparse, these extra layers increased the amount of attenuation. Removing this effect from the water block measurement with water leaves the result of 2.07 cm water equivalence. To combat these issues, a new water block was printed that did not use the extra four layers. Despite these containers being only 2 cm thick, the actual thickness of the water in the container was difficult to measure precisely as it could be overfilled, causing the surface to bulge. This bulging could cause an error in the thickness measurements of the water container.

As the measurements of the water block did not match those that were expected, another set of measurements were done using a water tank. These measurements were compared directly with solid water and it was found that between 1.5 cm and 4 cm there was less than 0.3% difference between the two. This difference is of the same order of magnitude of the error that we were working with, so this difference is irrelevant. However, it was found that the difference increased as the depth increased. Over the range of depths used in these experiments, this error is acceptable, however pushing past these depths, the difference could become problematic.

Each way of presenting the data is informative; the water equivalent measurements present the results achieved, highlighting the variations between blocks. The ratio indicates what is practically achievable and provides a standardised measurement, allowing comparison with the measurements taken with the 1 cm blocks. The density corrected results remove the effect of density on the measurements, effectively giving the material specific equivalence. This is what is theoretically achievable when printer settings, such as fill density and overlap, are optimised.

It is easier to make the materials that have a higher water equivalence less dense by changing print settings such as fill density. This makes materials with a higher water equivalence more appealing in a clinical setting as they can be adjusted to match the water equivalence required. If print settings, such as overlap and layer height, were optimised further, the blocks of some of the plastics could be printed with a higher density. This takes more effort than making the blocks less dense, however it means that some blocks would become closer to being water equivalent and others would require less plastic to be equivalent to 1 cm solid water, reducing the bulk of the bolus, which could be desirable in a clinical setting.

The first thing that needs to be kept in mind is that because of the chamber choice and the setup with the chamber being placed at the centre of a 2 block, there is an additional 1 cm of solid water that the beam is transmitted through before it reaches the chamber. The additional path length though the solid water causes problems because the beam is always passing through the solid water before it reaches the

chamber, which could be having some impact on the beam. Removing it would remove any possibility of having it an effect and therefore we used a different chamber and experimental setup for the PDD measurements present in section 3.4

Both the 1 and 2 cm blocks were tested using both 6 and 10 MV energies, however the 1 cm blocks did not give meaningful results in the 6 MV beam, while the 2 cm blocks did not give meaningful results in the 10 MV beam. This was because at 1cm, in a 6 MV beam, the measurements were made around the dose maximum which is the flattest part of the curve, where a 4 mm difference in depth only results in less than 1% change in dose. Accordingly, all of the point dose measurements for the 1 cm blocks were the same, making these results not fit for determining a solid water equivalence.

At 10 MV this effect is exacerbated due to the flat portion of the peak being spread over a greater range, with a 1% change in dose covering a range of 1.2 cm, with the dose maximum occurring at 1.8 cm in solid water. Fortunately, in the 6 MV beam the 2 cm blocks fall into a relatively linear portion of the curve and the 1 cm blocks fall into a linear section of the build-up region in the 10 MV beam, therefore only the 2 cm 3D printed plastics in the 6 MV beam and the 1 cm blocks in the 10 MV beam are presented.

Similarly to a quadratic around the maximum, there are two X solutions for every Y value. As a plot of TMR has a similar shape around the dose maximum, there is not a one to one relationship between dose and depth. Thus there are two possible depth solutions for one point dose measurement, one on either side of the TMR peak.

As already discussed, two solutions exist for most of the point dose measurements. To obtain the correct solution, it was assumed that only depth solutions above 1 cm were considered valid. This was due to the knowledge that none of the materials were going to have an equivalent thickness so low that they would equal less than 1 cm of solid water.

In a 6 MV beam, the 3D printed materials that were the closest to water equivalent were PLA and PVA, however due to PVA's water absorbing characteristics, it is not an ideal bolus material. Both ABS (printed with a 75% fill setting) and HIPS had a similar water equivalence and it is predicted they would need to be 10% thicker than the solid water they are trying to mimic to have equivalent radiation interaction properties. TPU had an even lower solid water equivalence requiring it to be more than 20% thicker than solid water to be water equivalent. ABS, on the other hand, was the only material to have a solid water equivalence that was predicted to need to be 15% thinner than solid water.

3.1.2 10 MV

While the 10 MV results are interesting on their own, the main purpose of presenting them in this project is as a comparison to the 6 MV results. The particle interaction components for 10MV are

different to 6MV due to a greater presence of pair and triplet production and a reduction in the amount of Compton interactions. This causes a shift in the attributes that are required to be water equivalent from electron density towards atomic number.

In contrast to the 6 MV results, for 10MV the depth from TMR ambiguity is resolved by only selecting depths below the dose maximum.

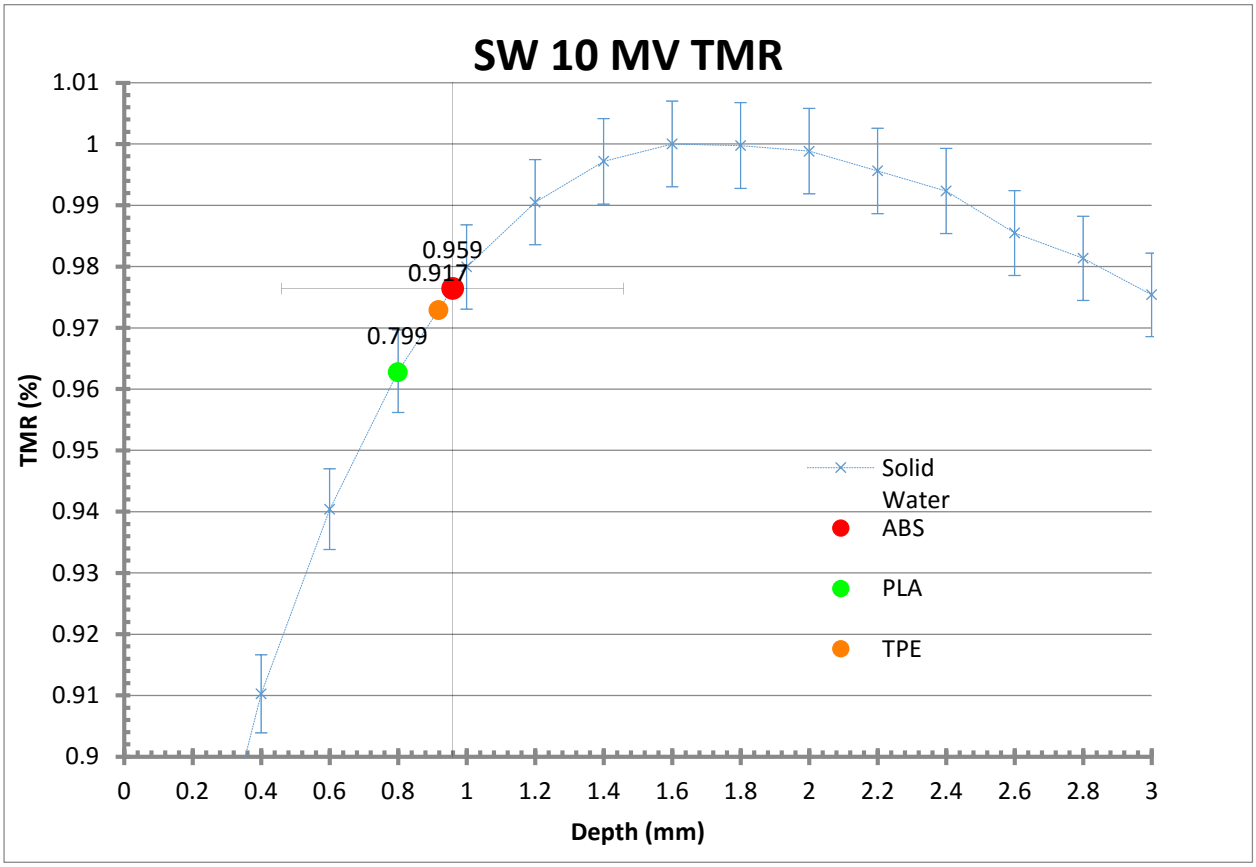

Fig. 1. TMR curve using 10 MV photons in Gammex solid water with point doses for 3D printed Materials and 0.7% error bars displayed.

Table 3.7. The ratio of the dose measured at 1 cm into 3D printed plastics and Solid water in a 10 MV beam.

Material	TMR	Z	ρ	Z_{eq}	Z_{eq}/Z	$Z_{eq}/Z \cdot \rho$
ABS	0.976	0.953	0.99	0.96	1.01	1.02
PLA	0.963	0.973	0.86	0.80	0.82	0.95
TPU	0.973	0.957	1.00	0.92	0.96	0.96

Where ABS in the 6 MV beam required less material to be water equivalent, at 10 MV ABS is water equivalent with the thickness adjusted ratio being 1.01.

Similarly to ABS, the amount of PLA required to be water equivalent has increased. Where at 6 MV, PLA was water equivalent, in a 10 MV beam PLA has a thickness adjusted ratio of 0.82.

In contrast to both the ABS and PLA results, the amount of material required for TPU to be water equivalent in a 10 MV beam decreased with a thickness adjusted ratio of 0.96 compared to 0.77 in the 6 MV beam.

It should be noted that because the 1cm blocks in a 10 MV beam fall in the build-up region, where electronic equilibrium has not been established, these results could underestimate the amount of dose being deposited, skewing the results. If all the 10 MV results had shifted in the same direction by a similar amount, this could have been attributed to a systematic decrease in the dose measured, however with TPU decreasing while both ABS and PLA increase, it is inconclusive.

Dose measurements of a 5x5x2 cm block and a 7x7x2 cm block, printed using the same filament, were compared and the results showed that in point dose measurements, there was only a 0.07% difference. When the same comparison was completed in water, the difference was 0.08% even though different printers were used. This suggests that the 5x5x2 cm blocks could be used in place of the 7x7x2 cm blocks as they provide the same accuracy in measurements. However, the 7x7x2 cm blocks were used in section 3.4 on attenuation measurements and section 3.5 on PDDs because it took minimal effort to print the larger blocks and meant that alignment errors would have less impact due to the size difference. Despite this, the PMMA blocks may have benefitted from using 5x5x2 cm block size as this may have prevented some of the warping.

Adding the water (and container) resulted in measured relative doses that were only consistently 0.6% different which, although small, does not align with the previous results because the 0.6% should have overshadowed the 0.08%. Accordingly, the effect the water container was having on the measurements was questioned. The dose measured with the 7x7x2 cm block in the container with no water was compared with the dose measured with the same block sitting directly on solid water. Using these measurements the container was found to affect the relative dose by 0.6%. This explains the above results, and suggests that the effect of the water is much less than the effect of adding the container to the measurement, meaning that water did not need to be considered in future experiments.

As the plastics have unknown radiation properties it is not possible to predict where the dose maximum is going to occur. This is interesting clinically because if a bolus were to make up all of the build-up region, then slight discrepancies in attenuation properties would not have a large impact on the point dose measurements around the dose maximum, but would still shift the entire dose. In later experiments, by making measurements more frequently and over a range of thicknesses of the 3D printed plastics, we were better able to understand what effect they were having on the dose distribution. There is however, another possible explanation; that a fundamental difference had been introduced between the attenuation properties of the 1 cm and 2 cm blocks. Our best efforts were made to maintain consistent printing conditions and they were printed in the same material, from the same manufacturer, on the same printer. However, the printer itself was inconsistent and therefore some print

settings had to be adjusted. These adjustments were only made in ways that we considered to have minimal impact on the attenuation properties of the blocks but it is possible that the impact of a change made was underestimated.

3.2 Depth scaling factors

Table 3.8, Depth scaling factors calculated for a range for 3D printed materials

Material	ABS	PLA	PMMA	HIPS	PVA	Solid Water	Water
$\frac{D_P}{D_W}$	1.011	0.898	0.943	1.319	0.855	0.988	1.000

Table 3.8 presents the depth scaling factors calculated for 3D printed materials based on their relative electron density compared with water. The density used for calculation was based on the densities were able to achieve when the materials were 3D printed.

The material that has a depth scaling factor closest to 1 is ABS. Based on its calculated electron density, ABS is the most water equivalent with 1 cm of ABS being equivalent to 1.011 cm of water.

PMMA is the next closest to water, with 1 cm of PMMA being equal to 0.943 of water. PLA, HIPS and PVA are significantly less water equivalent with 1 cm of each plastic being equal 0.898, 1.319 and 0.855 cm of water respectively.

Solid water was also included as it was used as a comparison in the preliminary experiment. Solid water is close to water with 1 cm of solid water be equivalent to 0.988 cm of water.

In the preliminary experiments a TMR in solid water was used as a comparison for the point dose measurements of the 3D printed plastics. Solid water comparison makes the ABS results appear less water equivalent because 1 cm of solid water is equal to slightly less than 1 cm of water, while 1 cm ABS is equal to slightly more than 1 cm of water increasing the apparent difference.

The electron density of PMMA was estimated even though it wasn't included in preliminary investigations as it was used in later investigations but wasn't physically available to us during the preliminary experiments. The proportional elemental make up of ABS and HIPS could be at least estimated, hence the inclusion of these materials, however TPU is not presented in this section as we were unable to obtain this information. The manufacturer was contacted but did not respond to our request for this proprietary information and we were unable to find this information in any previous literature. An estimate of the proportional elemental make up was not able to be made due to the method of producing TPU which depends on how complete the polymerisation is. The constituent

elements of TPU could have been measured directly using a technique like nuclear magnetic resonance (NMR) spectroscopy but this was outside the scope of the current project.

During the analysis it became apparent that mass density plays a large role in creating the difference between the different plastics, this suggests that adjusting the density to be similar to that of water is more important than the elemental composition. This also suggests that the relationship between the density of the blocks and the print settings used to produce them needs to be fully characterised if consistent results are to be achieved. In quality control systems, such as those required for the clinical production of bolus for use in radiation therapy, density would need to be a point of control.

Although there will be a different response between types of filaments, this mathematical analysis of the electron density suggests that is more important to print in a material that prints consistently. Due to the lower melting point, PLA is generally easier to print with, which generally translates into more consistent print quality and more consistent radiation interaction properties. This makes the comparison between ABS, which is more water equivalent, and PLA, which although less water equivalent is generally easier to print, informative.

Although we don't know the exact ratios of the constituent elements of both ABS and HIPS and our knowledge of what is added is also limited, we do know enough to give us an indication of what response we should expect when they are introduced into a high energy photon beam.

When comparing these results to those measured in the preliminary experiment, there appears to be a relationship between the water equivalent measurement when it has been density adjusted and the prediction made by the electron density. From the density adjusted results in the preliminary investigations, it was expected the most water equivalent plastic would be ABS and HIPS followed by PVA and PLA, with TPU being the least water equivalent. In this experiment, ABS was confirmed as the most water equivalent plastic followed by PMMA which was not available during the preliminary experiment. PLA and PVA were next with HIPS being the least water equivalent. TPU was not used in this experiment so cannot be compared. HIPS is the most surprising, being predicted as one of the most water equivalent materials and measuring as the least water equivalent. This could be because the mass density used for the calculation was based on the density achieved during the 3D printing process. Optimising the print settings could increase the density and therefore make HIPS more water equivalent.

By assuming that only Compton interactions occur for this analysis, increasing the energy from 6 MV to 10 MV means that the ratio of the interactions shifts to include more pair and triplet production, increasing the dependence on atomic number. These predictions were simply intended to give an indication of the possible applications of the plastics as water equivalent materials. In clinical 6 MV beams there is a spectrum of energies, therefore there is a proportion of the beam that still undergoes numerous photoelectric effect interactions.

Another way of estimating the water equivalence of the 3D printed plastics would be using the effective atomic number. Taylor et al. (2012) developed an application that would calculate the effective Z of custom materials based on the interaction cross-section of their constituent elements. By using the spectrum of a clinical 6 MV LINAC, collected by Mohan, Chui, & Lidofsky (1985), the application takes into consideration the poly-energetic nature of the beam. Although a direct comparison can't be made as we were looking at the effect of Compton scattering and its dependence on electron density, the predictions made by Taylor et al. (2012) provide additional information regarding the effect of changing energy.

Table 3.9. Comparison of the effective Z of 3D printed materials

Material	ABS	PLA	PMMA	HIPS	PVA	SW	Water
Effective Z	3.57	4.23	3.64	3.46	3.44	3.58	3.35
$\frac{Z_{eff}}{Z_{eff}^{water}}$	1.066	1.263	1.087	1.033	1.027	1.069	1.000
$\frac{D_P}{D_W}$*	1.011	0.898	0.943	1.319	0.855	0.988	1.000

* Duplicated for ease of comparison

Based on the ratio of the effective Z (Z_{eff}**)** of the plastics and the effective Z of water (Z_{eff}^{water}), PVA and HIPS are the closest to 1, and therefore water, once again with a ratio of effective Z of 1.027 and 1.033 respectively. ABS and Solid water were the next closest with 1.066 and 1.069 respectively. PMMA is slightly higher with a ratio of 1.087 and PLA has a much larger ratio than the rest of the plastics at 1.263.

This adds additional information about how the materials might become more or less water equivalent at lower and higher energies. For example, as the energy is increased PVA would be predicted to become more water equivalent because its effective Z is closer to water whereas HIPS would become less water equivalent as its depth scaling factor, based on its electron density is closer to water than its effective Z.

The electron density scaling results, combined with the effective Z, allow us to make predictions about the expected CT results. As CT energies are lower than treatment energies, a difference between the electron density scaling results and the CT results are expected. These differences could be explained with the effective Z.

CT numbers are calculated from equation 1.13 defined in chapter 1.1.3. A positive CT number suggests that the material would be more attenuating than water and a negative CT number indicates that the material would be less attenuating than water. The more attenuating the material, the less material needed to achieve water equivalence. PLA, for example, has a scaling factor of less than one and therefore should have a positive CT number. If the prediction based on electron density is incorrect and

the effective Z is greater than 1, it indicates that a larger positive CT number than predicted by the electron density scaling results.

Based on electron density, the expected CT results would be ABS being closest to water and having a higher CT number. PMMA, PLA and HIPS follow respectively however are while ABS is a positive CT number, the electron density results predict that these three plastics should have increasingly negative CT numbers.

3.3 Evaluation of the CT numbers of 3D printed materials

All the results in this section are displayed in terms of CT numbers. A calibration curve within the treatment planning system allows us to convert the CT numbers to ED. The curve is determined by taking a CT of samples of a known range electron densities. When the CT scans were analysed, the electron density was recorded but is not presented here as the CT number is a more intuitive number when interpreting the results.

Table 3.10, The CT numbers measured for a range of 3D printed materials.

Material	Colour	CT Number (HU)
ABS	White	7 ± 13
PLA	Black	115 ± 24
PMMA	Natural	69 ± 13
HIPS	White	-283 ± 25
TPU	Black	-127 ± 29
PVA	Natural	141 ± 29
Polyjet	Grey	112 ± 35
Water	Transparent	-5 ± 21

First, the CT number of water needed to be determined as this will determine the plastic most representative of water, and then all the other results can be compared to the water results. Water is, by definition, 0 HU, however due to the differences in the energy spectrum of each CT scanner, the CT

number measured for water varies around 0 HU. The mean value for water for our scanner in the 3D printed water container was –5 with a SD of ± 21.

ABS had the CT number closest to water of 7 ± 13 HU. This also agrees with the prediction made in previous section. ABS had a standard deviation of only ± 13 which is less than that of water, suggesting that homogeneity is not an issue. This is taken from the inside volume of the block so there may still be some variation in the outer layer of the block which is printed in a different pattern.

PLA had a CT number of 115 ± 24. The electron density results predicted that PLA would have a negative CT number however it has an effective Z greater than 1. An explanation for this could be that at lower energies, PLA is more attenuating because a great number of photo electric interactions are taking place due to the high effective Z.

While PMMA was expected to have a negative CT number, it wasn't predicted to be very negative. However, PMMA was measured to have an intermediary CT number of 69 ± 13. Density may also have played a role in the increase of PMMA's CT number. Although PMMA was not analysed in the preliminary investigations, it was measured for the attenuation experiment which be presented section 3.4.

HIPS had a CT number of -283 ± 25 which is consistent with the depth scaling predictions. HIPS also has a low density which would make the CT number increasingly negative. The low density could be due to air being introduced into the block during printing.

TPU had a CT number of -127 ± 29. There were no predictions made for TPU as it was not included in the depth scaling experiments because the proportional constituent elements were unable to be determined. TPU was measured in the preliminary experiment and had a density similar to water, however it had a low water equivalence when adjusted for the actual thickness of the block. This would suggest that TPU should have a large negative CT number even without the predictions from the depth scaling experiments.

PVA had a CT number of 141 ± 29 which differs from the predicted PVA results. PVA had an effective Z closest to that of water (1.027) and an electron density scaling factor of 0.855 which predicts a large negative CT number. This suggests that the density of the PVA block could be playing a role in the increased attenuation causing the large positive CT number. If the print quality was low and additional air was introduced into the block, we would expect that the density and the CT to decrease rather than increase, suggesting that this is not the case for the PVA block.

Polyjet had a CT number of 112 ± 35. As the constituent elements of Polyjet are unknown, a prediction of its electron density or effective atomic number were unable to be made. It was expected that print quality would be high and not have much air introduced during the print meaning that it would have a density higher than that of water which would predict a positive CT number.

Liquid water is a homogenous medium though some variation in CT number is expected due to noise within the imaging system. With water having a standard deviation of ± 21 it suggests that the 3D printed materials, all of which had a similar standard deviation, were also reasonably homogenous when compared to water.

Table 3.11. Comparison of the CT number of ABS from different filament manufacturers

Manufacturer	Colour	CT Number (HU)	Printer
Diamond Age	White	-53 ± 19	K&K
Hobbyist	White	-54 ± 24	Qubea
Kuehling & Kuehling	White	-82 ± 18	K&K

The CT number of ABS varies between manufacturers. When comparing filaments from different manufacturers, the diamond age filament was -53 HU which while more negative than the result present for ABS previously, was the closest to water. Hobbyist had very similar results to that of the Diamond Age filament at -54 HU while the Keuhling & Kuehling filament was quite different and more negative at -82 HU. As discussed above, the standard deviation for water on our CT machine was 21 therefore, the standard deviations measured for the different ABS manufacturers which were similar, suggest that a similar homogeneity was able to be achieved with different ABS manufactures.

The results for all the ABS filaments are more negative than predicted by their electron density and effective atomic number. The average CT number for the ABS blocks produced for the attenuation and PDD measurements was 7 HU. These were printed out of the diamond age filament which is very different from the -53 produced in this experiment. The blocks for the attenuation and PDD measurements were printed last, after experimentation and optimisation of print setters specifically for the Diamond Age filament.

We received the Kuehling and Kuehling filament with the purchase of the Kuehling and Kuehling RepRap Industrial. The factory print setting for ABS were optimised by Kuehling and Kuehling for their filament, however we encountered issue printing this filament even with these optimised settings. These problems could have caused the introduction of air into the prints, which could explain the lower than expected CT number measured.

The Hobbyist results were also more negative than we expected. The sample from the Hobbyist was provided to us from the Hobbyist and was therefore printed on a different printer. The Hobbyist supply their own filament, however we are unsure where they source this filament. It is interesting that

Hobbyist ABS filament provided a similar result to that of the Diamond Age filament, despite the fact that it was printed on a different printer.

It should be noted that in the cylinder test, which is discussed later in this section, Diamond Age filament was again used and a CT number of -14 HU was measured.

While the three different ABS filaments compared gave similar CT number results, they were all lower than predicted. Due to the fact that all the results were relatively similar, despite being low, it is unlikely that the filaments themselves are the cause of the lower than expected measurements. As the Hobbyist ABS filament was printed on a different printers but still measured similar results, it is unlikely that it is the printer itself that is causing the lower than expected results, and is more likely to be the printer configuration.

Quality assurance will need to play a large role in verifying that the printer is maintaining a consistent quality if it is going to be used in clinical applications, such as bolus. This is important because the print settings impact the attenuation properties of the sample. More rigorous investigations need to be conducted on the effect of print settings, such as layer height, and print configurations, such as nozzle size, to determine their impact on attenuation properties.

Table 3.12. A Comparison of different combinations of PLA with different colours.

Material	Colour	CT Number (HU)	Printer
PLA	Clear	113 ± 14	MDFstrap
PLA	Black	-192 ± 29	MDFstrap
PLA	Black	115 ± 24	K&K
PLA	Orange	144 ± 26	Ultimaker

Clear PLA and black PLA printed on the same MDFstrap printer had contrasting results with the clear PLA having a CT number of 113 HU and therefore being more attenuating than water and the black having a CT number of -192 HU meaning it is less attenuating than water. The same black PLA as previously mentioned was printed on a K&K printer and had results similar to the clear PLA with a CT number of 115 HU. The orange PLA provided to us by Ultimaker was printed on one of Ultimaker's printers using an unknown filament provider and achieved a CT number of 144 HU.

While little is known about the Ultimaker block, it is known that it was printed using Ultimaker's proprietary slicing software Cura. Cura was also the slicing software used with the MDFstrap printer, while the K&K used slicing software slic3r. As three of the four prints used the same software, and two

of them are similar, it would appear that the slicing software is not the cause of the difference recorded in the black PLA printed on the MDFstrap.

If there was an extrusion issue of the MDFstrap during printing, this could lead to more air being introduced into the print than is desired. This could explain the low CT number of the black PLA printed on the MDFstrap.

The differences highlighted in this experiment show again the need for careful quality control when producing items for clinical use, such as bolus.

Although the aim of this comparison was to explore only the effect different colour additives in PLA would have on its attenuation properties, other variables such as the printer used and the filament manufacturer were not consistent between colours. Showing only the clear and black PLA printed on the MDFstrap suggested that colour played a large role in the attenuation properties. It is unlikely that this difference was due to the colour additives, shown by the other two setups having similar results to the clear PLA, and more likely to be an effect of printer settings and print consistency.

ABS produced by Diamond Age was printed on both the Kühling&Kühling and the MDFstrap to compare the effect the printers were having on the attenuation properties. Using the Kühling&Kühling, a 7x7x2 cm block was printed using Sli3er which resulted in a CT number of -53 HU with a SD of 19 HU. A 5x5x2 cm block was printed on the MDFstrap using CURA which resulted in a CT number of 4HU and a SD of 15 HU. The densities of the two blocks were similar with 0.99 for the Kühling&Kühling print and 1.02 for the MDFstrap print. While it is not optimal that the blocks are different sizes and different slicers were used, the filament is the same, and the print settings were matched as closely as the two printers allowed which means that the results still offer a comparison of the different printers.

It is thought that for each filament-manufacturer pair there would be a theoretical maximum CT number that is achievable for a specific printer. As the settings move away from the theoretical optimal, more and more air is being introduced creating spaces between the extrusions and layers resulting in lower CT numbers. This is a possible explanation for why the ABS block produced by the Kühling&Kühling printer had a more negative CT number than that produced by the MDF strap, suggesting that the Kühling&Kühling printer's parameters needed more optimisation.

A range of materials were evaluated to determine which was the most water equivalent and would therefore be the best candidate as a bolus material. These same measurements were used to define the electron density of the 3D printed bolus for use in the treatment planning system.

There are two options to determine the electron density; one is to repeat the patient scan with the bolus in place, simulating how well the bolus fits. This would provide a quality control examination which would detect fluctuations in the CT number, caused by errors in the 3D printing process. This option,

however, means that the patient receives another scan and therefore additional dose. The other option would be to characterise the 3D printing process and ensure that the bolus fits the patient well and then define the bolus as an object in the treatment planning system with a specified electron density. A CT of the bolus by itself could still be taken and could used in quality control examinations, comparing its CT number with the known value of the 3D printed plastic being used. This option also omits the need for the additional patient scan, reducing the dose to the patient.

The depth scaling factors were calculated for both HIPS and PVA despite these plastics not being included in the attenuation and PDD experiments. HIPS and PVA were both analysed in the preliminary investigation, depth scaling estimations and in the CT analysis. PVA was not used in the future experiments as it is soluble in water meaning it is not ideal for bolus which need to be stable in general use. HIPS was not used in the future experiments as throughout the preliminary experiments and subsequent CT analysis ABS out performed it in terms of water equivalence. Further optimisation of the printing parameters for HIPS could improve its water equivalence but that was outside of the scope of the current project.

3.4 Photon Attenuation characteristics of 3D printed materials

The main aim of this experiment was to determine which 3D printed plastic had an attenuation coefficient closest to water. However this procedure is not something that would be carried out in a clinical setting but is more of a fundamental examination of the underlying physics.

It should be noted that the results plotted are the linear attenuation coefficients and not the mass attenuation coefficients.

Figure 3.20. shows that the measured value for PLA was more attenuating than expected for water, however this is what was expected based on linear attenuation coefficient calculated by NIST Xcom database. It also shows that the measured value for PLA and the NIST prediction for PLA are in close agreement. The R value is a measure of how well the data agrees with fitted model. An R value of 0.995 suggests that the agreement between the measured values and the exponential model fit is appropriate but there is some variation around the value predicted by the model. This is shown in the graph as the first three values are less than the predicted exponential whereas the last two are greater.

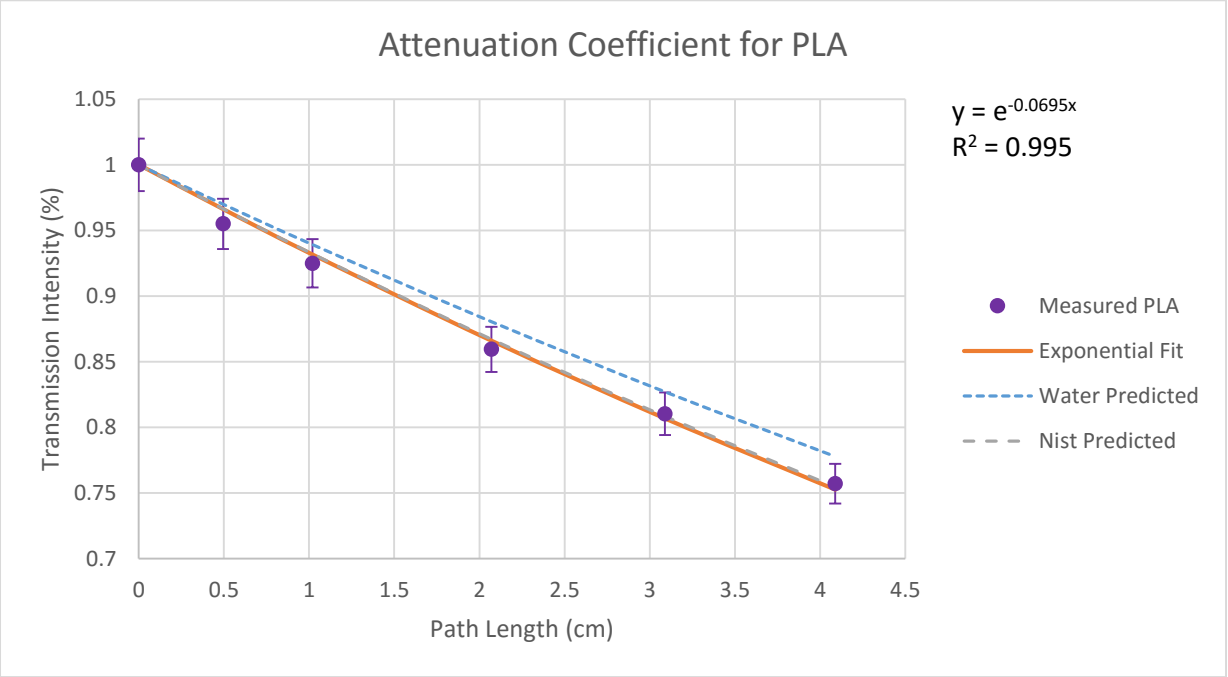

Figure 3.20. Comparison between the measured attenuation coefficient for PLA fitted with an exponential, the attenuation coefficient predicted by NIST and the attenuation coefficient for water.

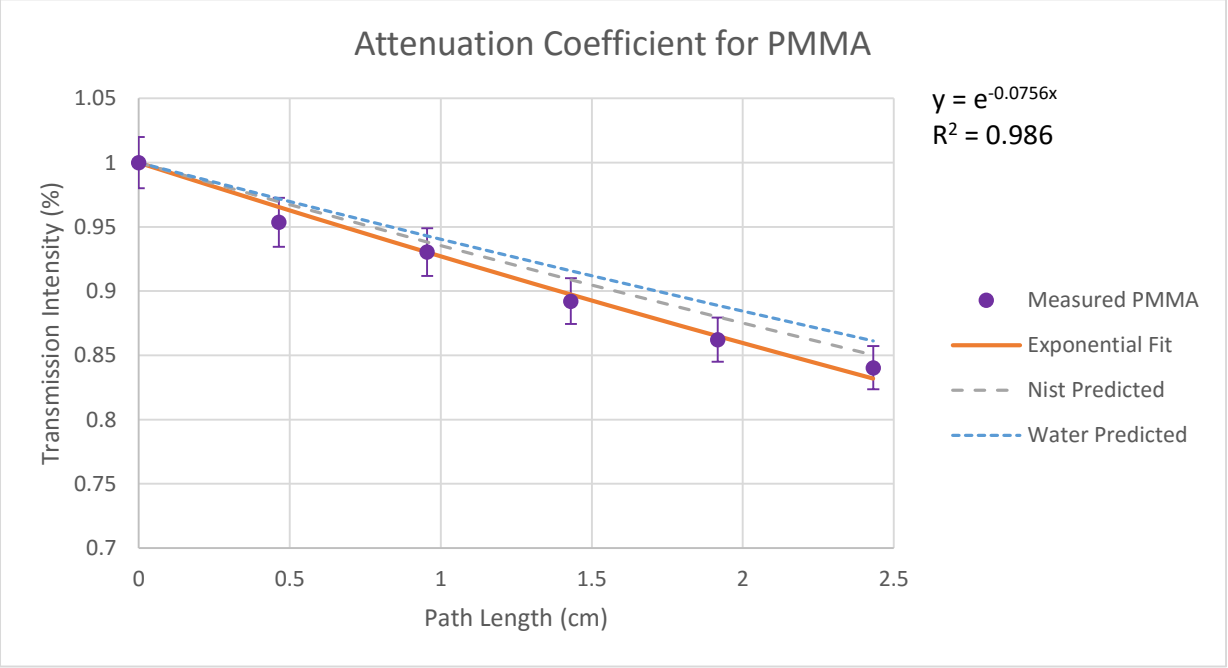

Figure 3.21 Comparison between the measured attenuation coefficient for PMMA fitted with an exponential, the attenuation coefficient predicted by NIST and the attenuation coefficient for water.

Figure 3.21 shows that PMMA, similarly to PLA is more attenuating than the expected values for water but unlike PLA, PMMA does not line up the NIST prediction. The linear attenuation coefficient predicted for PMMA by NIST was less attenuating and therefore closer to water than that measured for PMMA. The R value for PMMA is 0.986 which is lower than PLA suggesting that there is more variation in the PMMA measurements than there is in the PLA measurements.

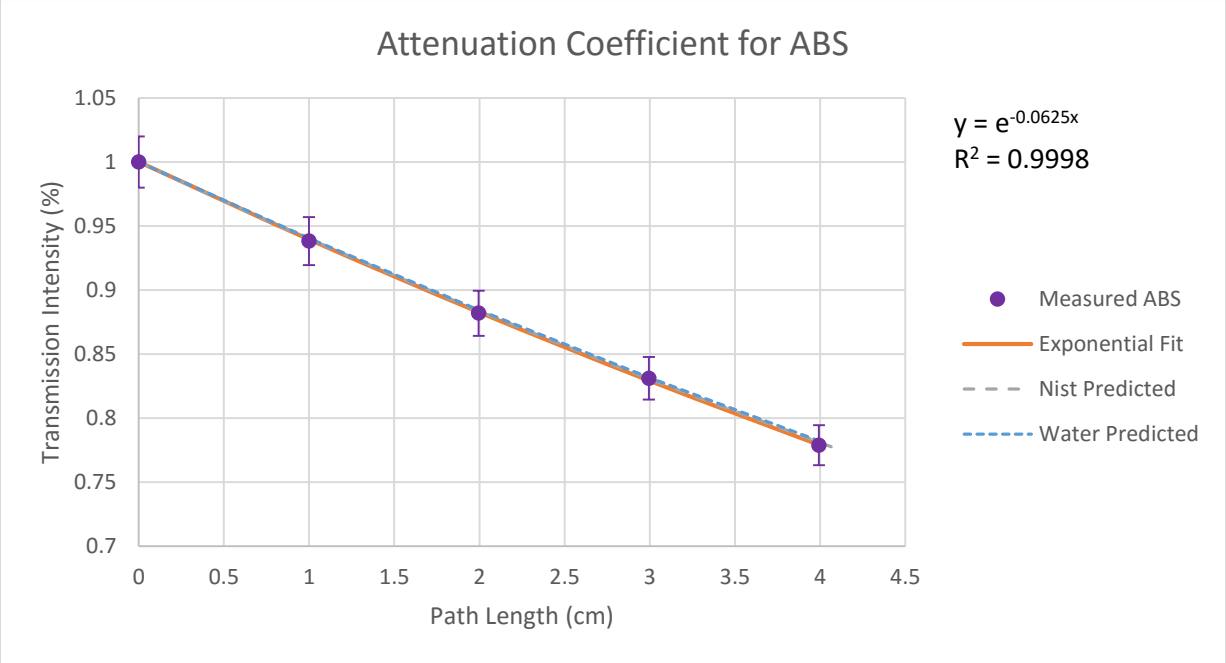

Figure 3.22 Comparison between the measured attenuation coefficient for ABS fitted with an exponential, the attenuation coefficient predicted by NIST and the attenuation coefficient for water.

Figure 3.22 shows that the results measured for ABS and those predicted by NIST are in excellent agreement. The linear attenuation coefficient of ABS is also very similar to the expect value of water. The R value is even closer to 1 than PLA, at 0.9998 with little measurable variation from the exponential predicted.

The first result that needed to be determined was the mass attenuation coefficient for the 5 cm water block. This was measured and found to be $0.0615 \pm 0.0012\ g/cm^2$ which suggested that the poly-energetic LINAC beam, had a mono-energetic effective energy of 1.32 ± 0.05 MV. The mean energy of a Clinac-6 (6 MV) was found by Mohan et al (1985) to be 1.92 MV. Although this was for a 10x10 cm field size and a Varian LINAC, which is not directly comparable with an Eleckta LINAC with a 5x5 cm field size, it does suggest that the result is at least reasonable.

Table 3.13. Comparison of the Linear Attenuation Coefficients for 3D Printing Plastics and Water

	PLA	PMMA	ABS	Water
Measured Linear Attenuation Coefficient (cm^{-1})	0.0695	0.0756	0.0625	0.0615
Measured Density (g/cm^3)	1.176	1.115	1.033	1.002
Measured Mass Attenuation Coefficient (cm^2/g)	0.0591	0.0678	0.0604	0.0616
Mass Attenuation Coefficient Percentage difference from Water (%)	-4.0	10.1	-1.9	
R^2	0.995	0.990	0.9998	
Mass Attenuation Coefficient predicted by NIST XCOM database (cm^2/g)	0.0585	0.0598	0.0599	
Percentage difference from NIST (%)	1.0	13.3	1.0	
NIST predicted difference from water (%)	-5.0	-2.8	-2.8	

The mass attenuation coefficient of ABS was measured to be $0.0604 \pm 0.0012\ g/cm^2$, which is 1.9% less attenuating than water, however this difference is negligible within our experimental error. This result indicates ABS was also only 0.9% more attenuating than that predicted by the NIST's XCOM database, suggesting that the estimated constituent elements is reasonable and also agree with both the depth scaling prediction based on electron density and the CT number. Within our experimental error, our measurement agrees with that predicted by NIST. These results suggest that 3D printed ABS would make an excellent water equivalent material

The mass attenuation coefficient of PLA was measured to be $0.059 \pm 0.0012\ g/cm^2$, which is 4% less attenuating than water, but only 1.0 % more attenuating than predicted by NIST's XCOM database. Within our experimental error, our measurement agrees with that predicted by NIST. These results suggest that any additives in the filament are not having an observable impact on the radiation properties at treatment energies compared with theoretically pure PLA.

The mass attenuation coefficient of PMMA was measured to be $0.0678 \pm 0.0014\ g/cm^2$, which is 10.1% more attenuating than water, and 13.3% more attenuating than what NIST's XCOM database predicted. This suggests that there may have been an error with the measurement and should be further investigated. The result was predicted to be between 10% and 5% different from water and less than 1% different from the NIST XCOM database which was achieved in the other materials. A possible explanation could be variations in the thickness and density of the blocks used for the measurement as they were particularly difficult to produce. It was expected that under the narrow beam conditions used for these measurements that air gaps and warping should have less of an effect but this is not what was observed. The predicted value for PMMA is similar to that of ABS.

One problem encountered in the preliminary experiments, was that there were two possible depth solutions for each point dose measurements because of the build-up region. By measuring attenuation coefficients, the build-up of dose as electronic equilibrium is reached is removed. By using the preliminary results in section 0 in combination with these attenuation results, we could confirm that the results on the far side of the build-up curve were indeed the correct solutions. These results can also be used in combination with the PDD results presented next, to provide a more complete picture of what is occurring. As already mentioned in section 1.1.3, there are two components that make up PDDs: the primary component and the scattered component. By using narrow beam geometry we are essentially able to disentangle the effect of scatter from the attenuation caused by 3D printed blocks.

Determining the attenuation coefficients at treatment energies (6 and 10MV) counteracts one of the limitations of using CT as it only provides an estimate of the attenuation at diagnostic energies (80 -140 keV). This would overestimate the effect of high Z materials due to a larger proportion of photoelectric events occurring. As the exact constituent elements of some of the materials is proprietary knowledge, it is difficult to predict how much of an effect this will have. The CT number results predicted that ABS, PMMA and PLA would all be more attenuating than water, with ABS being the most water equivalent and PLA being the least. The attenuation results showed that ABS was the most water equivalent as predicted by the CT number results, however PMMA had uncharacteristically high attenuation disagreeing with what was predicted by both the CT number results and NIST's Xcom database.

Constantinou, Attix, & Paliwal (1982) suggest that to achieve practical narrow beam conditions, the field size should be minimised to provide a uniform field to the ion chamber. In this experiment, the chamber, CC04, has a radius of 2mm and a length of 3.6mm, the field size reaching the chamber at 2.5m was 2.5 x 2.5cm^2 therefore, we could have used a 2x2 mm^2 field size, which would have resulted in a 5 x 5mm^2. However the smaller the field size the more difficult alignment would become, both in terms of collimation and ensuring correct placement of the chamber, increasing positional uncertainty.

One possible way to evaluate if true narrow beam conditions were achieved would be to plot the attenuation coefficient of a material, such as water, over a range of diminishing field sizes. Another method would be to increase the distance between the source and the chamber and determine if the inverse square law was still being followed. It would be expected that the attenuation would plateau and then possibly decrease as alignment became the limiting factor.

The validity of our assumption that the effective energy of a LINAC beam can be determined using the attenuation coefficient of water needs to be considered. One possible method of validating this method would be to use a photon emitter of a known energy and determine its effective energy based on measurements of its attenuation coefficient of water.

As already discussed in 1.2.3, for a poly-energetic photon beam, attenuation of the primary component is not strictly exponential. The low energy components of the beam will be attenuated more than the

high energy components, increasing the mean energy of the primary beam. This reduces the overall attenuation which moves away from the expected exponential relationship (Mayles et al., 2007).

This could be dealt with by calculating a beam hardening coefficient that describes the change in the attenuation per unit length as it is absorbed. Beam hardening could be expected to cause a variation of 0.5% per centimetre. Given that only 4cm of material was used, it would therefore only introduce a 2% error into the measurements.

3.5 PDDs

The main aim of this experiment was to demonstrate, in a clinically relevant way, what depth scaling would be required to achieve water equivalence for the selected 3D printed plastics.

Figure 3.23a, Figure 3.24a and Figure 3.25a present the percentage depth dose measurements in ABS, PLA and PMMA individually compared with water before they were depth scaled and offset while Figure 3.23b, Figure 3.24b and Figure 3.25b present the plastics after they were depth scaled and offset.

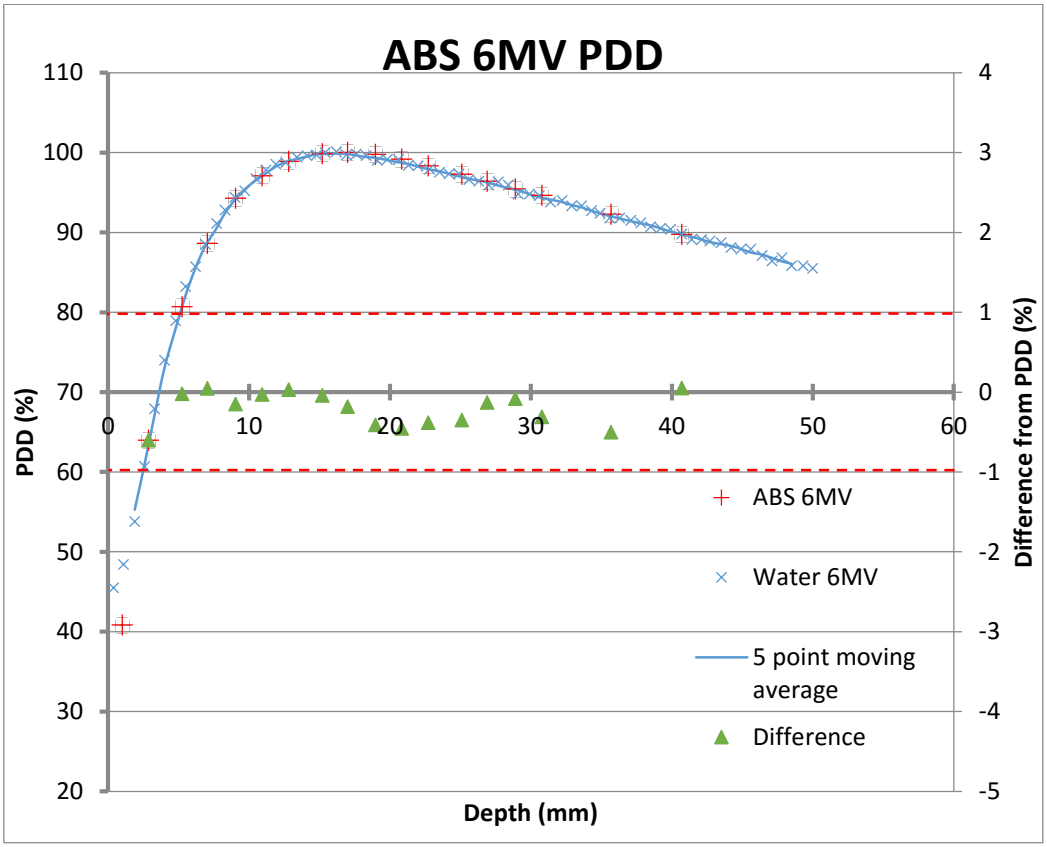

(a)

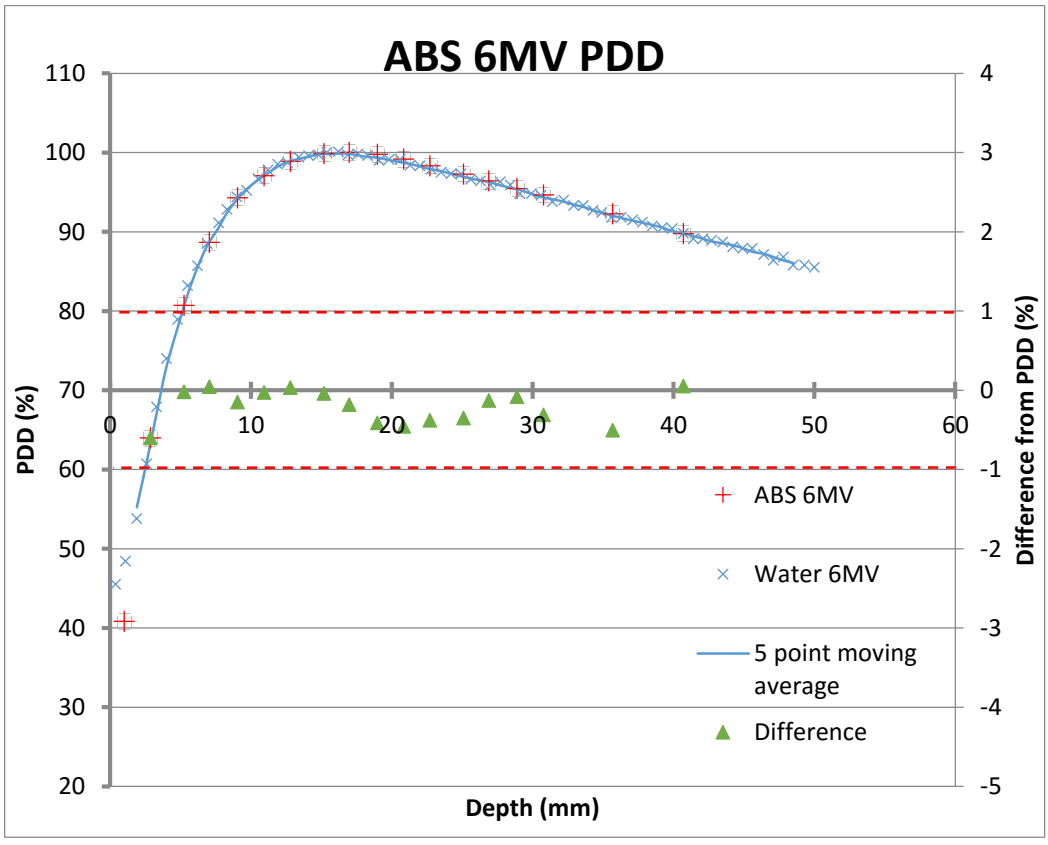

(b)

Figure 3.23, PDD for ABS compared with water measured with CC13 in the blue phantom for a 5cm x5cm field size 6MV photon beam. Difference plotted on secondary Y axis. (a) Original data PDD for ABS at 6 MV with depth not shifted or scaled which results in a sum of square of 1.68, (b) 0.15 mm Shift and 0.97 scale which results in a sum of squares of 0.61. The red dashed line illustrates a 1% error difference.

The raw data for ABS resulted in a squared difference of 1.68%. With a scaling factor of 0.97 and a depth offset of 0.15mm, a minimum sum of the squared differences of 0.61% was achieved. Figure 3.23 shows the PDDs for ABS before and after the offset and scale were applied.

As discussed in section 1.2, for a material to be considered water equivalent, the ICRU suggests that it should not impact the dose by more than 1%. The depth scale prediction based on electron density for ABS was 0.989 which is reasonably close to the 0.97 scaling factor. It can be seen both before and after the scaling and offsetting that all the differences in both plots are below 1%. This suggests that within our measuring accuracy, the results for water and ABS are equivalent. The shift and scale determined are small and also suggest that the ABS is essentially water equivalent. This suggests that ABS could be used as a water equivalent material without the need for a depth correction factor. However, our error is very close to the ICRU limit of 1% so further investigation would be needed.

It should be noted that although there are slight fluctuations in the ABS PDDs measured in water at 28.5mm and 40mm, their effect has largely been removed during the smoothing process. As the difference is calculated between the measured and smoothed values, these fluctuations have little effect.

The validity of including an offset needs to be discussed. If the scaling is calculated without allowing the optimiser to calculate a shift, the scaling factor calculated is 0.992, with a resulting sum of the squares of 1.43%. This suggests that there is even less of a difference between water and ABS.

There is a possible explanation for the shift in that the water PDD and the ABS PDD were measured using different experimental setups. The setups should be identical but with a combined positional uncertainty in depth of $\pm$ 0.65 mm ($\pm$ 0.5 mm for the water PDD measurement and $\pm$ 0.15 mm for the block measurement) a 0.15 mm shift is reasonable.

The remaining differences seem to follow a pattern that repeats every cm. A possible explanation is that there were slight differences between the blocks and the pattern is formed because they were used in repeating combinations to make up each depth. They also give an indication of random measurement uncertainty.

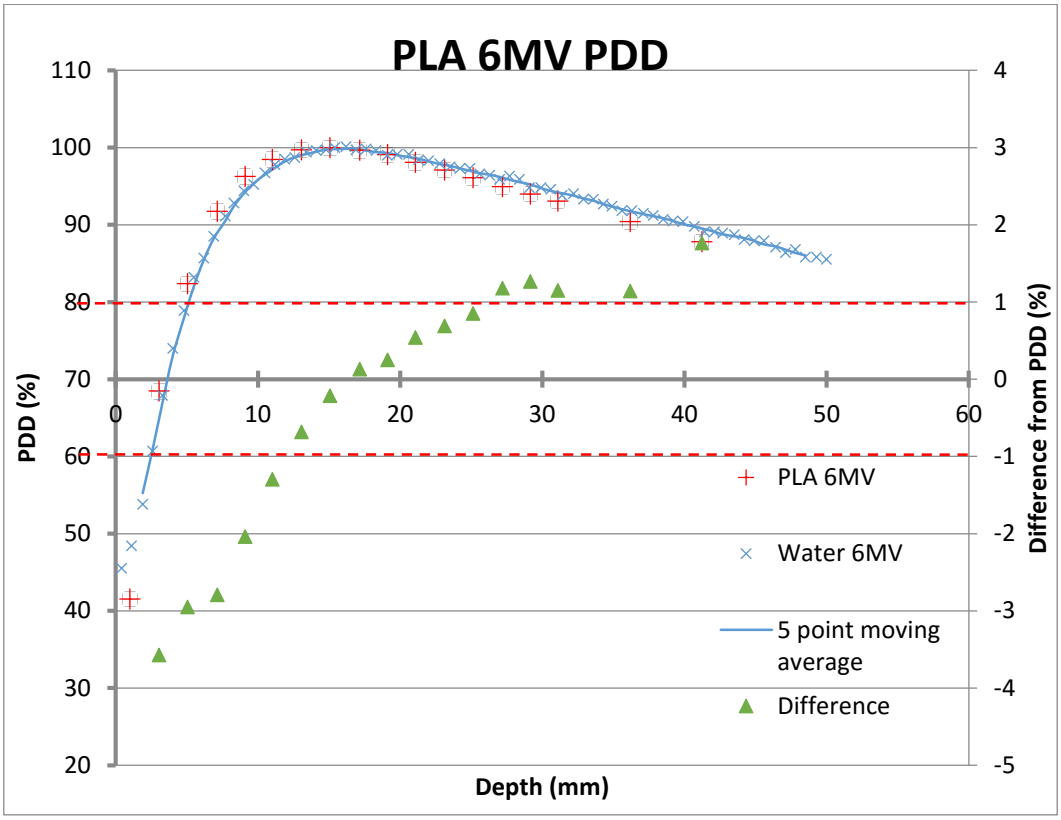

(a)

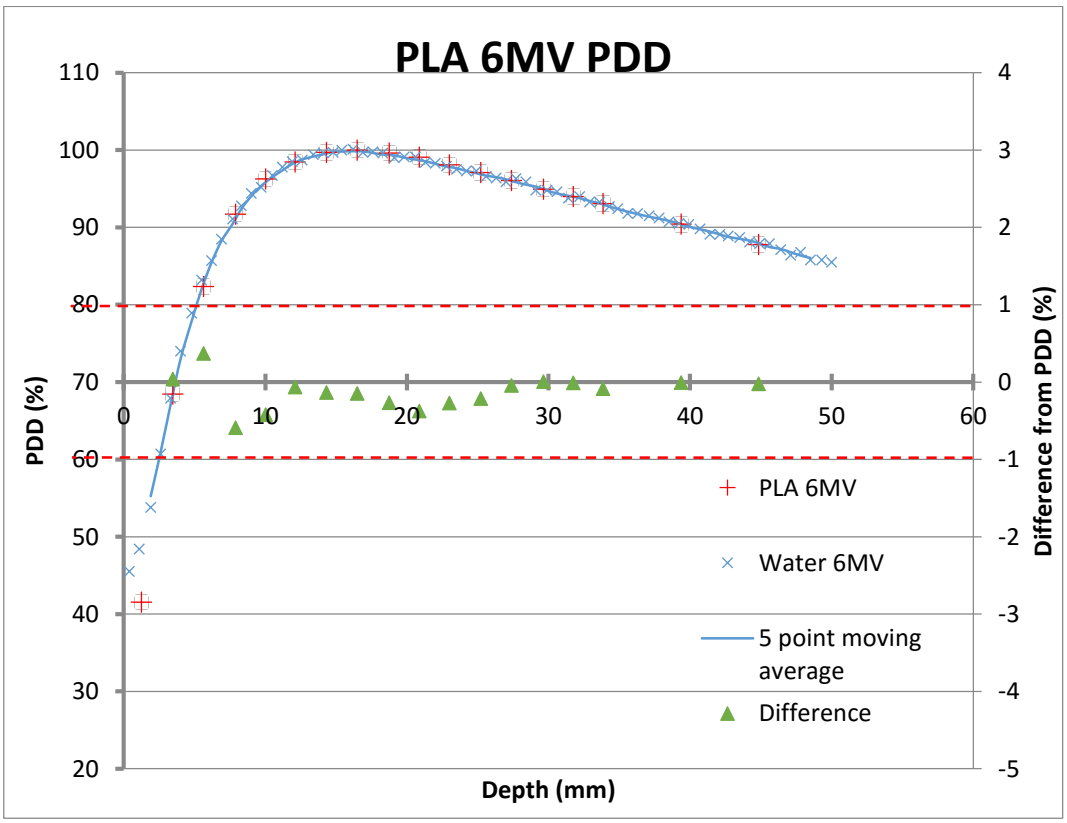

(b)

Figure 3.24, PDD for PLA compared with water measured with CC13 in the blue phantom for a 5cm x5cm field size 6MV photon beam. Difference plotted on secondary Y axis. (a) Original data PDD for PLA at 6 MV with depth not shifted or scaled which results in a sum of square of 45.9, (b) 0.154 mm shift and 1.083 scale which results in a sum of square of 1.04. The red dashed line illustrates a 1% error difference.

The raw data for PLA resulted in a squared difference of 45.9%. When scaled by a factor of 1.08 and once again applying 0.15 mm depth offset, the sum of the differences is reduced to a minimum of 1.04%. Figure 3.24 shows the PDDs for PLA before and after the offset and scale factor were applied.

It can be seen that before both scaling and offsetting, there seems to be a trend in the differences with the deep and shallow measurements being above 1%. This suggests that within our measuring accuracy the results for water and PLA are not the same. But after scaling and offsetting, all the differences are below 1% suggesting that PLA could be used as a water equivalent material if a depth scaling factor is applied.

The depth scaling predicted for PLA based on the electron density was 1.11 which is 3% different from the 1.08 scaling factor measured here.

Once adjusted, the largest difference between the water and PLA was the point at 8mm which is in the build-up region where the gradient was the greatest. This is in part due to it being the vertical distance that is used as the difference, whereas if the perpendicular difference was used, the gradient would have less impact on the difference measured.

The same justification stands for PLA as it did for ABS. The fact that the offset for PLA is the same for ABS brings credibility to the assumption that it could be due to a setup difference.

The raw data for PMMA results in a squared difference of 31.2%. It was found that scaling the depth by 1.06 and offsetting by 0.1 mm resulted in a sum of the squares of 1.75%. Scaling by 1.055 while offsetting the depth by 0.22 mm, decreased the sum to 1.39%. Figure 3.25 shows the PDDs for PMMA before and after the offset and scale were applied.

The depth scaling predicted for PMMA based on the electron density was 1.074 which is only 2% different to the measurement.

It can be seen both before scaling and offsetting that there seems to be a trend in the differences with the shallow measurements being above 1%. For PMMA, a depth was not reached where the deeper measurements also broke the 1% threshold. However , the trend suggests that it would have if we had been able to measure deeper. This suggests that within our measuring accuracy the results for water and PMMA are not the same. After scaling and offsetting, all the differences are below 1% suggesting that PLA could be used as a water equivalent material if a depth scaling factor is applied.

The depth shift is larger for PMMA but not so much larger that it couldn’t be explained in the same way. The print quality of the PMMA blocks was not to the same level that it was for the ABS and the PLA, with significant warping and inconstancies within the blocks.

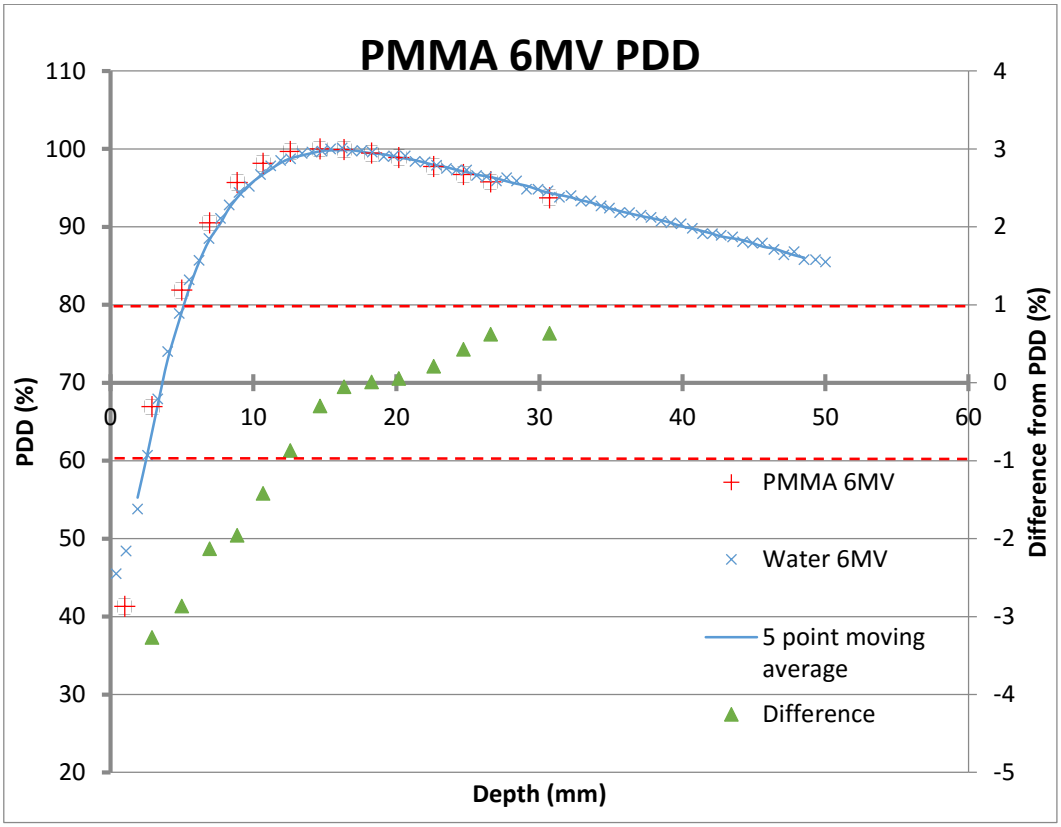

(a)

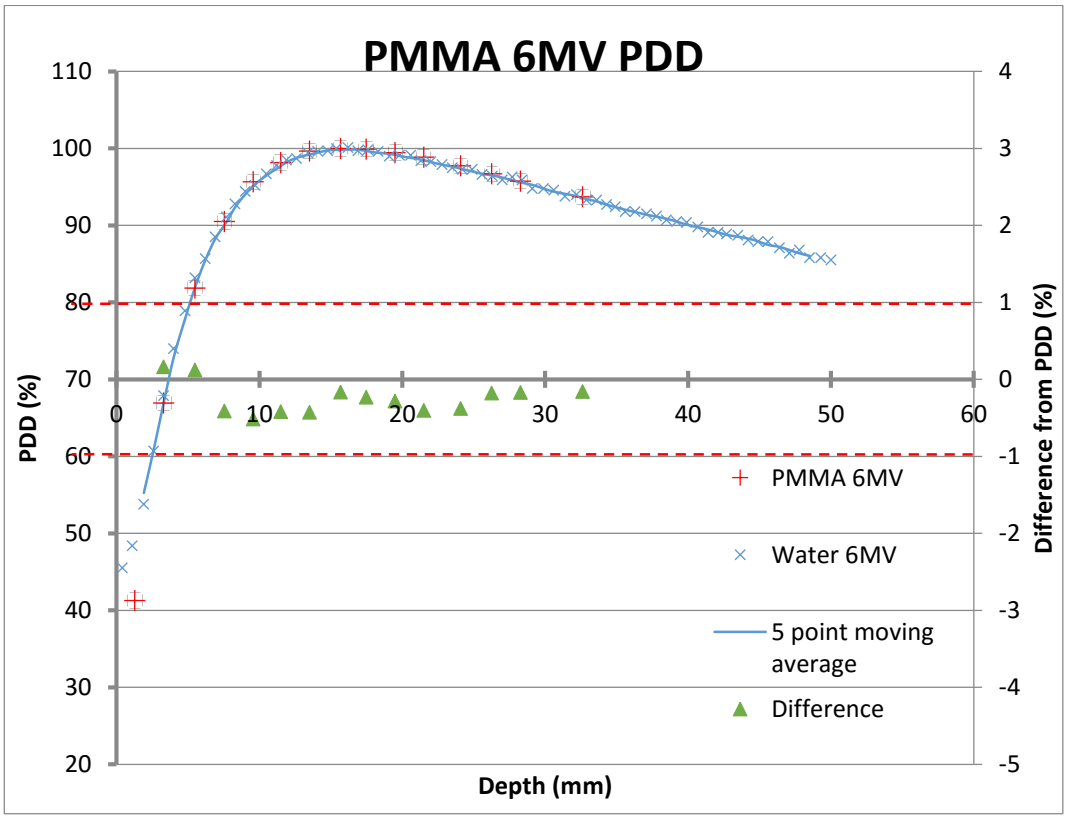

(b)

Figure 3.25, PDD for PMMA compared with water measured with CC13 in the blue phantom for a 5cm x5cm field size 6MV photon beam. Difference plotted on secondary Y axis. (a) Original data PDD for PMMA at 6 MV with depth not shifted or scaled which results in a sum of square of 31.2, (b) 0.22 mm Shift and 1.055 scale which results in a sum of square of 1.39. The red dashed line again illustrates a 1% error difference.

Similarly to ABS and PLA, there is a difference at the point 5.5mm which is where the gradient was the greatest in the build-up region. In PMMA, however, the largest difference was measured at 9.5mm where there is a dip in the water curve.

An investigation using the absolute differences instead of a square differences was carried out between the water and plastic PDDs and it was concluded that there were minimal differences. This is believed to be due to the absence of significant outliers, as squaring the difference amplifies the effect of the outliers.

Using the PDD method gives us a much clearer illustration of what is happening to the dose within these 3D printing materials compared to the point dose measurement method used in the preliminary experiment. Although the PDD method has the advantage that it combines measurements over a series of blocks, ideally the measurements would be repeated for multiple sets of plastic blocks and the scaling factors averaged. As there was little variance away from the model in our measurements, it gives some confidence in the measurements without having to repeat them. By standardising the printing parameters, we know that the differences measured are due to the materials and are as independent as possible of the print settings.

3.6 An example of clinical bolus

Figure 3.26. shows the percentage dose measured using film, with and without the 3D printed bolus in place. It should be noted that the dose deposited is within the phantom and that the dose deposited within the bolus was not measured. It was expected that the bolus would shift the dose distribution to shallower depths (to the left as shown on Figure 3.8) by approximately 0.98 cm (the thickness of the bolus 1 cm being multiplied by the scaling factor which had a value of 0.98). The percentage depth dose plotted in Figure 3.27 with the 3D print bolus in place has been shifted 1cm deeper (to the right) to show how well they align when the attenuation of the 1cm of bolus is taken into account. It can be seen the deposition of dose is not only affected by the bolus but also by the spatial distribution of the density of the material it is passing through.

In higher density materials, like bone, the dose will be deposited more rapidly. This is illustrated in the PDD by a larger negative gradient after Z_{max}. The opposite is true in a less dense material like air, where the dose is deposited more slowly and the gradient becomes less negative. The interactions that occur at a transition into a higher (or lower) density material, are complex and beyond the scope of the current project but could be an explanation for the characteristic increase in dose deposition and then the fall off that occurs near a transition and appears as a “bump” in the dose deposition. This is complicated further, by the presence of noise which can artificially insert similar “bumps” into the dose distribution.

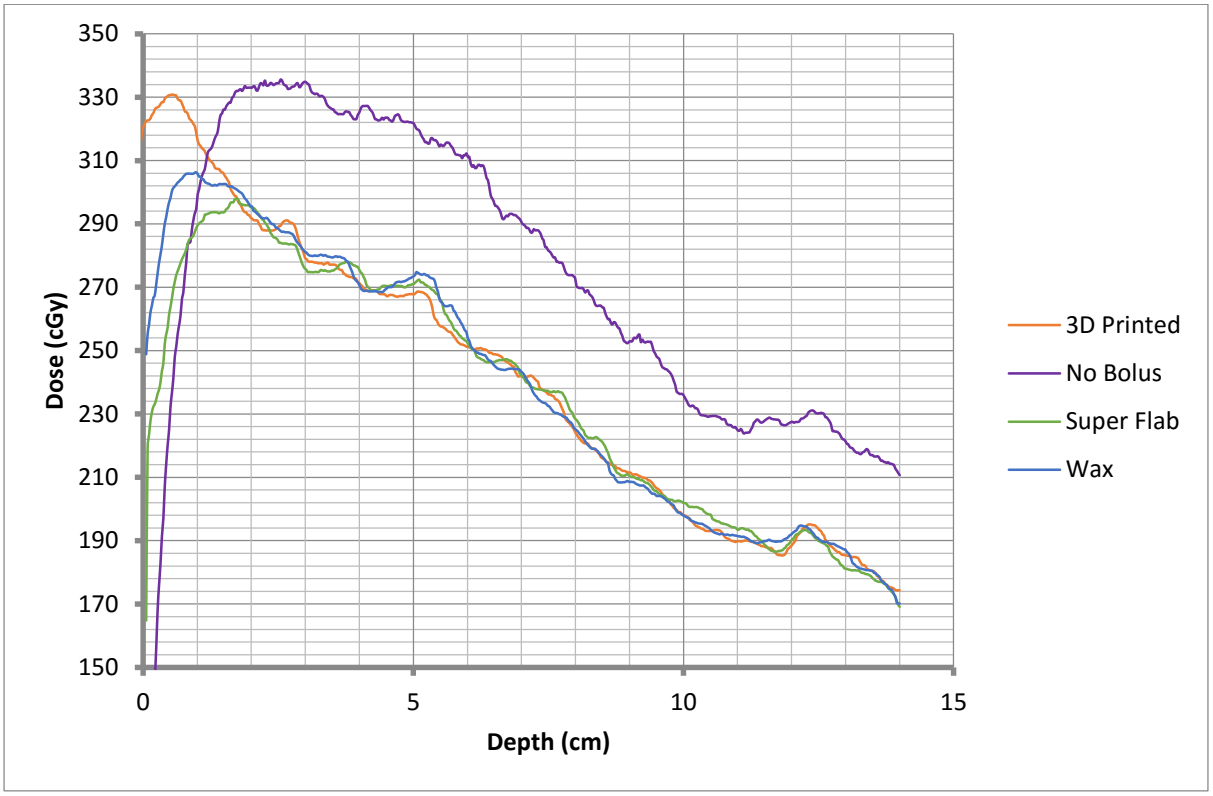

Figure 3.26. Absolute dose measurements of different bolus materials.

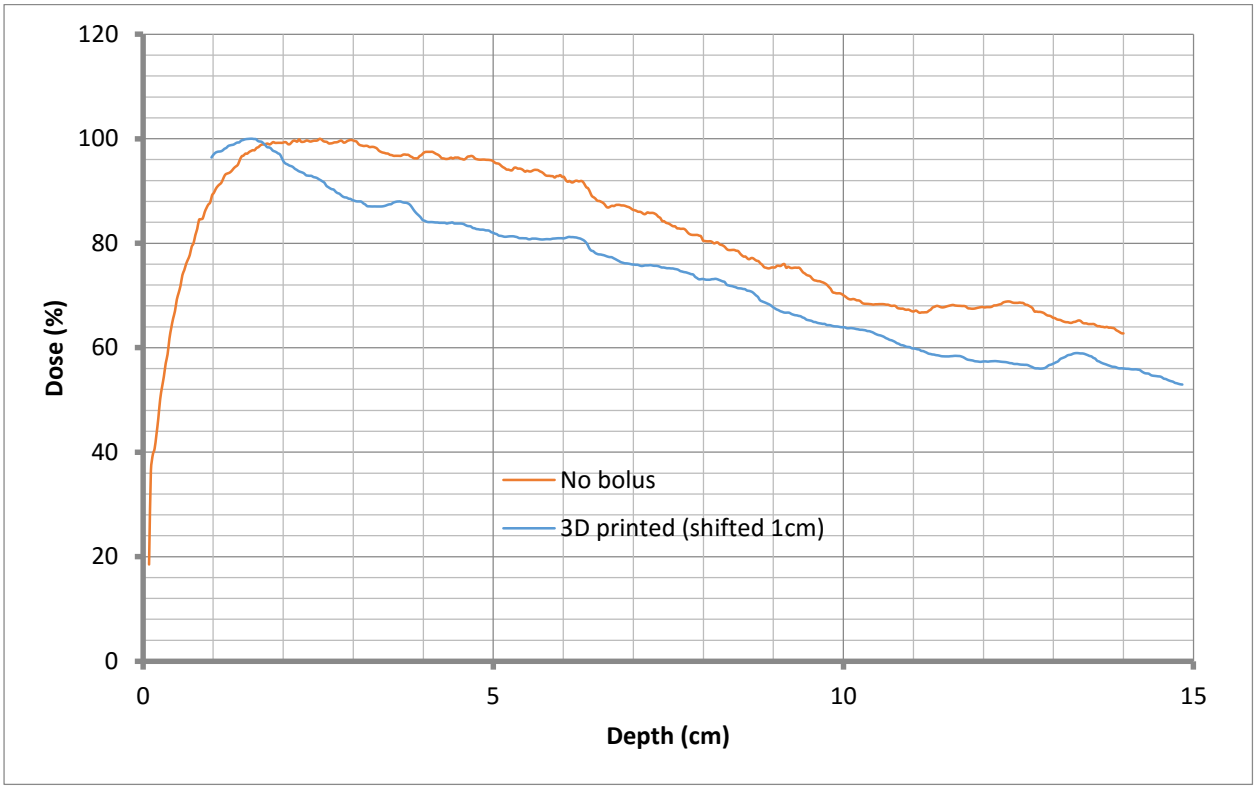

Figure 3.27 Normalized dose measurements of the 3D printed bolus shifted by 1cm and no bolus.

Figure 28Even though the dose distribution has been shifted superficially by 1cm, the dose still passes through the anatomy at the same place. Accordingly, the characteristic changes in dose deposition shown in the Figure 3.26. are in similar places in each of the materials as they encounter the anatomy in the same place. However, the 3D printed data has been shifted in Figure 3.27 so the characteristic changes have also been shifted, making them more difficult to compare.

Some characteristic changes that appear in the 3D printed data are not shown in the bolus free data. This difference can possibly be explained by random setup errors, meaning that the dose profile in each situation is not exactly the same. Between each film measurement, the boluses were exchanged, the phantom disassembled and the film removed. New film was then inserted and the phantom realigned. It was during this process that setup errors could occur. Due to the rapidly changing anatomy in the region of interest, even millimetre errors in setup position could mean that the anatomy encountered along the profile could be significantly different (e.g. bump number 2 which is caused by a bone).

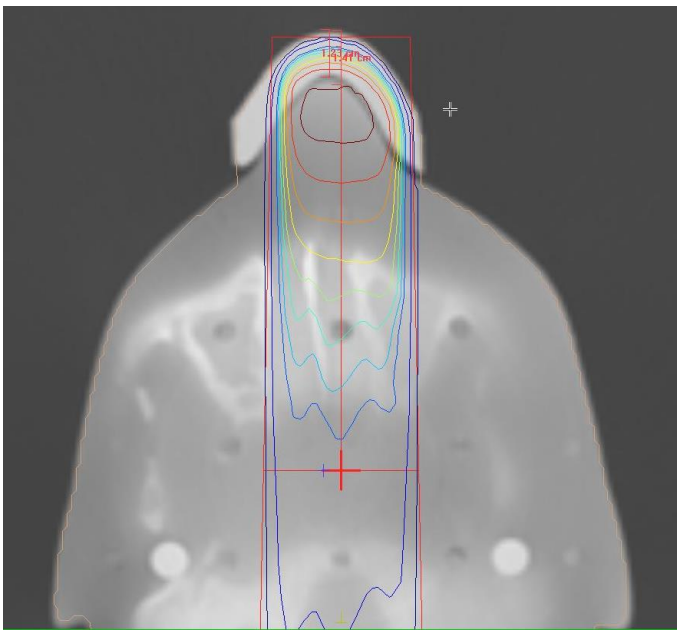

Figure 3.29. Dose distribution in the film plane calculated by Monaco with the 3D printed bolus in place. Illustration the effect of surface anatomical geometry

As demonstrated in Figure 3.29, due to our choice of anatomical site, the surface geometry starts narrow and slowly increases in width. This complicates the build-up process. The bolus extends the patient's surface 1 cm in every direction, which means that the curvature of the bolus is different from that of the patient. Not only is it different but the accumulation of the material occurs more rapidly. In the non-bolus case, there may only be 1 cm of tissue lateral to the beam, however with the 3D printed bolus in

place there is an extra 1cm of material on each side. This means that the dose builds up more rapidly. As it passes through the bolus, it is not only passing through 1 cm of extra tissue in which to build up in, it has also got more material laterally which creates another difference between the bolus and non-bolus cases. It is theorised that the surface geometry of the nose causes the dose without the bolus to plateau as scatter builds up, reaching a point where the attenuation reduces the dose by the same amount that the increase in scatter increases the dose. In the bolus case, full lateral scatter has been achieved and is no longer increasing dose, therefore the dose decreases more rapidly.

The 1cm on either side of the anatomy is only possible because the 3D printed bolus was created as a geometric expansion, whereas the Superflab only comes in 0.5cm sheets. The wax bolus starts as a 1cm sheet that then needs to be deformed into the surface contours of the patient, which can cause variations in the thickness of the bolus.

In the phantom used, nostrils and a nasal septum were not mimicked. This makes the dose distribution less anatomically accurate but in this case removes an area of rapidly changing anatomy that could be significantly impacted by alignment in patient setup.

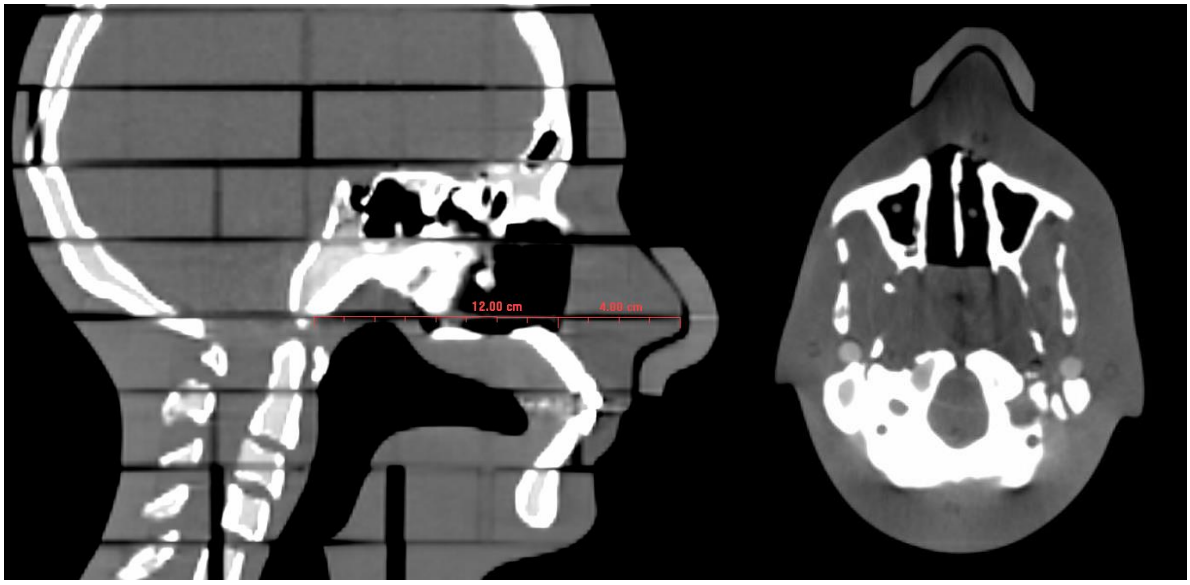

Figure 3.30. CT scans illustrating the 3D printed bolus in situ and the red ruler markings illustrate the film location

3.7 Error

Table 14. Uncertainty budget for the Preliminary investigation to estimate water equivalence,

Source of uncertainty		Prelim	Attenuation	PDDs
		TMR - Point doses		
Type A		0.04	0.3	0.01
Chamber Positioning				
	Solid Water	0.15	-	-
Depth	3D Printed plastics	0.3	0.3	0.3
	Water Tank	-	-	0.5
X - Y		0.04	0.2	0.04
Chamber Response				
Leakage		0.1	1	0.1
Ion Recombination		0.1	0.1	0.1
Direction dependence		-	-	0.1
Energy Dependence		0.1	0.1	0.1
Electrometer rounding		0.02	0.5	0.1
Linac Setup				
Field size		0.25	0.25	0.25
Gantry Angle		0.01	0.01	0.01
SSD	ODI	0.4	-	0.4
	Front Pointer	0.2	-	0.2
Output		0.3	0.3	0.3
Total		**0.7**	**1.3**	**0.8**

The Type A statistical uncertainty was estimated by taking ratio of the standard deviation and the mean of the raw measured values.

The intensity measurements TMR, PDD curves and are not absolute dose measurements and are therefore not reliant on the calibration chain to determine absolute dose. The error contributions can come from the positioning the chamber, error in the chambers response and the setup of the LINAC.

In terms of the initial setup of the chamber position, three different setups were used to carry out depth measurements. The solid water setup has a rigid geometry that is dependent only on the geometry of the solid water blocks which reduces uncertainties in depth positioning. The RMI solid water is certified to have a $\pm$ 0.15 mm tolerance on thickness and flatness. Comparing this tolerance to that achieved by the 3D printed PMMA blocks, which were the most difficult to produce, thickness of tolerance of $\pm$ 0.3 mm was achieved, except on the corners where warping occurred. The uncertainties due to flatness would dominate over the measurement accuracy of digital calipers used to measure the thickness of the blocks.

A water tank setup was also used which is more flexible and therefore has more degrees of freedom, increasing the setup uncertainty. The physical uncertainties in the setup position of the chamber within the water tank were estimated to be of the order of 0.5 mm.

The dose gradient for a 6 MV beam was measured to start at approximately 8% per mm in the build-up region to 0% per mm at dose maximum 15mm later and the quickly reach a value of -0.5% per mm tell the end of our measurements at 40mm. The average gradient which was calculated to be 1% per mm and was used to estimate that the effect of absolute depth uncertainty on the dose measured would be on average 0.15%. It needs to be acknowledged that using the average grossly underestimates the uncertainty in the build-up region where is can be as large as 1.2%, overestimates in at d_{max} where is wouldn't introduce an uncertainty at all and overestimates the uncertainty after d_{max} where the uncertainty would be 0.075%.

The effect of the thickness of the printed plastics on the attenuation measurements can be estimated by considering the flatness of the blocks which was $\pm$ 0.3 mm and transmission intensity which was estimated to on average fall by 1% per mm resulting in a uncertainty of 0.3%.

For both the Preliminary and PDD measurements the X and Y physical uncertainty was then used to estimate the dose uncertainty by using the off axis factor for a 5 x 5 cm^2 beam. Whereas for attenuation measurements a 1 x 1 cm^2 field size was

A portion of the error also generated within the chamber electrometer measurements system. The Roos chamber exhibits a directional dependence which combined with the uncertainty in the positioning on the linac could introduce a 0.1% error. The Roos chamber also exhibits an energy dependence with a difference of 0.1% expected for fluctuations of 0.2 MV. CC13 being a cylindrical chamber has does not a have a noticeable directional dependence. Of the charge that accumulates within the ion chamber two

process introduce uncertainty into the charge that is measured. The first process is recombination which was estimated to introduce an error of 0.1%, accounts for a decrease in the charge measured due to the recombining of ion pairs within the chamber volume.

The second process leakage which is generated by the measuring system as a whole but can be minimised by electrometer through proper nulling technique but some residual change leakage will still be present. For the PDD measurements leakage was estimated to be 0.1% for the 100MU, 5x5 cm^2 beams. Increasing the number of MUs deliver for each measurement would be one method of reducing the relative error due to leakage.

For the attenuation measurements even though 500MUs were delivered, due to the small field size, collimation and small chamber volume, the relative error due to leakage was estimated to be as large as 1% This is due the difference in the amount of change measure. In the PDD experiment the smallest measurements were 5.9 nC, whereas, the smallest measurement for the attenuation measurement was an order of magnitude smaller, with the smallest charge to be measured being 0.185 nC. The amount of time taken to deliver the charge was also five times longer providing more time for the charge leak away. It is possible to measure and correct for the leakage and this would have been recommended given the size of the uncertainty this process introduced in the attenuation measurements but correction was not required for the TMR and PDD measurements. The electrometer only displays 4 significant figures so it also introduce a rounding error. By analysing a range of raw values in the PDD and 1 division at that level divided by the whole charge measured the error component due to the rounding was estimated to be less than 0.1%. Because of the smaller magnitude of the charges measured for the attenuation measurements the rounding error was estimated to be 0.5%.

The distance between the photon source within the LINAC and the surface of the phantom was measured with either the optical distance indicator (ODI) or a mechanical front pointer. The ODI projects a scale onto the surface of the phantom and was estimated to introduce an error of 0.4%. The mechanical front pointer which that attaches to the face and uses a scale etched onto a tipped rod as physical measurement guide and has a scale that is more precise than that of projected scale of the ODI was estimated to introduce an error of 0.2%

4 Summary

This section is a final summary where the results from Section 3 will be considered in its entirety.

An investigation was performed of a selected set of printers to determine their capabilities before printing a range of materials of different thicknesses. Water equivalence of the 1cm and 2cm blocks using a TMR methodology was determined. Using this method, it was found that PVA and PLA were

the closest to water equivalent. A depth scaling factor based on the electron density of the materials was estimated and this predicted ABS to be the most water equivalent. To resolve this difference, the attenuation coefficient of both PLA and ABS was measured confirming the prediction that ABS was closest to water equivalent. This also confirmed the amount of depth scaling that PLA would require to be water equivalent. The blocks were scanned using CT to assess their uniformity and homogeneity and, as the CT number is used to determine the radiation properties of materials in a clinical treatment planning system, it also provides a measure indicating which material is most water equivalent. This once again confirmed that ABS is the closest to water equivalent as its CT number was closest to that of water.

In certain conditions the blocks were adequately uniform, however when print settings were not optimised, clearly visible variations in CT could be seen. The clinical examination was then extended using PDDs and blocks with a range of thicknesses to measure how dose would be deposited with depth. This would help determine how various thicknesses of each material would affect the dose distribution. It was found that there was no difference between the dose measured in ABS and the dose measured in water. A scaling factor for PLA was calculated to be of a similar magnitude to those previously determined.

It was then decided to use ABS to produce a 1cm bolus for a clinical site and compare its performance to other commonly used bolus materials. The 3D printed bolus was found to perform similar to the other bolus materials shifting the dose distribution by approximately the required 1cm. The exact shift in the distribution was difficult to determine due to the underlying anatomy causing variations in the dose. The 3D printed bolus outperformed the other bolus materials maintaining a surface dose similar to the maximum dose achieved without a bolus.

The feasibility of using that 3D printers to produce boluses in a clinical setting has been demonstrated. The material of choice for bolus would be ABS as it is the most water equivalent material with our printer. A depth scaling factor would not need to be used in our clinical setting, however this would need to be investigated on an individual basis. PDDs would need to be measured to provide the evidence required for clinical decisions to be made about how the dose distribution would be shifted. The bolus can be accurately defined digitally within the treatment planning system and exported as a DICOM structure. This structure file is converted into a file that is readable by the 3D printer. Once printed using the established optimal settings, the quality of the bolus would need to be evaluated by CT, verifying the CT number, the homogeneity and checking for the presence of artefacts. Point dose measurements could be used as a consistency measure with reference blocks if changes were made, including to the print settings or the filament provider. The fit of the bolus on the patient should be checked prior to treatment occurring. The DICOM structure which represents the physical bolus exactly, can then be used within the treatment planning system with an electron density set to 1 to precisely calculate dose delivered to the patient.

5 Bibliography

Ali, E. S. M., & Rogers, D. W. O. (2011). Functional forms for photon spectra of clinical linacs. *Physics in Medicine and Biology*, *57*(1), 31–50. http://doi.org/10.1088/0031-9155/57/1/31

Andreo, P., Burns, D. T., Hohlfeld, K., Huq, M. S., Kanai, T., Laitano, F., … Vynckier, S. (2000). *Absorbed dose determination in external beam radiotherapy: an international Code of Practice for dosimetry based on standards of absorbed dose to water*. *IAEA Technical Reports Series no 398* (Vol. 12).

Andreo, P., Huq, M. S., Westermark, M., Song, H., Tilikidis, A., DeWerd, L., & Shortt, K. (2002). Protocols for the dosimetry of high-energy photon and electron beams: a comparison of the IAEA TRS-398 and previous international codes of practice. International Atomic Energy Agency. *Physics in Medicine and Biology*, *47*, 3033–3053. http://doi.org/10.1088/0031-9155/47/17/301

Attix, F. H. (1986). *Introduction to Radiological Physics and Radiation Dosimetry*. Wiley. Retrieved from https://books.google.co.nz/books?id=PL8971RdEfoC

Benmakhlouf, H., Sempau, J., & Andreo, P. (2014). Output correction factors for nine small field detectors in 6 MV radiation therapy photon beams: a PENELOPE Monte Carlo study. *Medical Physics*, *41*(4), 041711. http://doi.org/10.1118/1.4868695

Beyler, C. L., & Hirschler, M. M. (2002). Thermal Decomposition of Polymers. In *SFPE Handbook of Fire Protection Engineering, 3rd Edition* (pp. 110–131).

Bibb, R., Thompson, D., & Winder, J. (2011). Computed tomography characterisation of additive manufacturing materials. *Medical Engineering & Physics*, *33*(5), 590–596. http://doi.org/10.1016/j.medengphy.2010.12.015

Blackwell, C. R., Coursey, B. M., Gall, K. P., Galvin, J. M., Mclaughlin, W. L., Meigooni, A. S., & Soares, C. G. (1998). Radiochromic Film Dosimetry. *America*, *25*(63).

Boles, M. (1972). Central Axis Depth Dose Data for Use in Radiotherapy. *Radiology*, *104*(1), 196. http://doi.org/10.1148/104.1.196

Brannon-Peppas, L., & Blanchette, J. O. (2012). Nanoparticle and targeted systems for cancer therapy. *Advanced Drug Delivery Reviews*, *64*(SUPPL.), 206–212. http://doi.org/10.1016/j.addr.2012.09.033

Burleson, S., Baker, J., Hsia, A. T., & Xu, Z. (2015). Use of 3D printers to create a patient-specific

3D bolus for external beam therapy. *Journal of Applied Clinical Medical Physics*, *16*(3), 166–178.

Constantinou, C., Attix, F. H., & Paliwal, B. R. (1982). A solid water phantom material for radiotherapy x-ray and gamma-ray beam calibrations. *Medical Physics*, *9*(3), 436–441. http://doi.org/10.1118/1.595063

Cunha, J. A. M., Mellis, K., Sethi, R., Siauw, T., Sudhyadhom, A., Garg, A., … Pouliot, J. (2015). Evaluation of PC-ISO for customized , 3D printed , gynecologic 192 Ir HDR brachytherapy applicators, *16*(1), 246–253.

Dimetrov, D., Schreve, K., & Beer, N. De. (2006). Advances in Three Dimensional Printing - state of the art and future perspectives. *Journal for New Generation Sciences*, *4*(1), 21–49.

Espalin, D., Arcaute, K., Rodriguez, D., Medina, F., & Posner, M. (n.d.). Fused Deposition Modeling of Polymethylmethacrylate for Use in Patient- Specific Reconstructive Surgery. *Design*, 569–583.

Fischer, F., & Stratasys. (2011). Thermoplastics : the Strongest Choice for 3D Printing.

France, A. K. (2013). *Make: 3D Printing*. Maker Media, Incorporated. Retrieved from https://books.google.co.nz/books?id=K5MlnQEACAAJ

Geraldelli, W., Tomal, A., & Poletti, M. E. (2013). Characterization of tissue-equivalent materials through measurements of the linear attenuation coefficient and scattering profiles obtained With Polyenergetic Beams. *IEEE Transactions on Nuclear Science*, *60*(April), 566–571. http://doi.org/10.1109/TNS.2013.2248382

Hall, E. J., & Giaccia, A. J. (2012). *Radiobiology for the Radiologist*. LWW.

Harris, B. D., Nilsson, S., & Poole, C. M. (2015). A feasibility study for using ABS plastic and a low-cost 3D printer for patient-specific brachytherapy mould design. *Australasian Physical & Engineering Sciences in Medicine*, *38*(3), 399–412. http://doi.org/10.1007/s13246-015-0356-3

Hiemenz, J., & Stratasys Inc. (2008). *3D Printing With FDM*. Retrieved from http://www.stratasys.com/~/media/Main/Files/White Papers/SSYS-WP-3DP-HowItWorks-09-11.ashx

Hill, R. F., Brown, S., & Baldock, C. (2008). Evaluation of the water equivalence of solid phantoms using gamma ray transmission measurements. *Radiation Measurements*, *43*, 1258–1264. http://doi.org/10.1016/j.radmeas.2008.01.019

Hull, C. W. (1986). Apparatus for Production of Threedimensional Objects By Stereolithography.

Jelčić, Ž., & Ranogajec, F. (2012). Radiation modified high impact polystyrene. *Radiation Physics and Chemistry*, *81*(9), 1366–1369. http://doi.org/10.1016/j.radphyschem.2011.11.044

Johns, H. E., & Cunningham, J. R. (1983). *The physics of radiology*. Charles C. Thomas. Retrieved from https://books.google.co.nz/books?id=7TprAAAAMAAJ

Jones, R., Haufe, P., Sells, E., Iravani, P., Olliver, V., Palmer, C., & Bowyer, A. (2011). RepRap – the replicating rapid prototyper. http://doi.org/10.1017/S026357471000069X

Khan, F. M. (2010). *Khan's The Physics of Radiation Therapy*. Wolters Kluwer Health. Retrieved from https://books.google.co.nz/books?id=cvtPBAAAQBAJ

Kim, S.-W., Shin, H.-J., Kay, C. S., & Son, S. H. (2014). A Customized Bolus Produced Using a 3-Dimensional Printer for Radiotherapy. *PLoS ONE*, *9*(10), e110746. http://doi.org/10.1371/journal.pone.0110746

Kudchadker, R. J., Antolak, J. a, Morrison, W. H., Wong, P. F., & Hogstrom, K. R. (2003). Utilization of custom electron bolus in head and neck radiotherapy. *Journal of Applied Clinical Medical Physics / American College of Medical Physics*, *4*(4), 321–33. http://doi.org/10.1120/1.1621494

Kudchadker, R. J., Hogstrom, K. R., Garden, A. S., McNeese, M. D., Boyd, R. a, & Antolak, J. a. (2002). Electron conformal radiotherapy using bolus and intensity modulation. *International Journal of Radiation Oncology, Biology, Physics*, *53*(4), 1023–37. Retrieved from http://www.ncbi.nlm.nih.gov/pubmed/12095572

Kumar, R., Sharma, S. D., Despande, S., Ghadi, Y., Shaiju, V. S., Amols, H. I., & Mayya, Y. S. (2010). Acrylonitrile Butadiene Styrene (ABS) plastic-based low cost tissue equivalent phantom for verification dosimetry in IMRT. *Journal of Applied Clinical Medical Physics*, *11*(1), 24–32.

Lasdon, L. S., Waren, A. D., Jain, A., & Ratner, M. (1976). Design and Testing of a Generalized Reduced. *ACM Transactions on Mathematical Software (TOMS)*, *4*(1), 51.

Leary, M., Kron, T., Keller, C., Franich, R., & Lonski, P. (2015). Additive manufacture of custom radiation dosimetry phantoms : An automated method compatible with commercial polymer 3D printers. *Jmade*, *86*, 487–499. http://doi.org/10.1016/j.matdes.2015.07.052

Lindsay, C., Kumlin, J., Jirasek, a, Lee, R., Martinez, D. M., Schaffer, P., & Hoehr, C. (2015). 3D printed plastics for beam modulation in proton therapy. *Physics in Medicine and Biology*, *60*(11), N231–N240. http://doi.org/10.1088/0031-9155/60/11/N231

Low, D. A., & Hogstrom, K. R. (1994). Determination of the relative linear collision stopping power and linear scattering power of electron bolus material. *Physics in Medicine and Biology*, *39*(6), 1063.

Low, D., Starkschall, G., Bujnowski, S., Wang, L., & Hogstrom, K. (1991). Electron bolus design for radiotherapy treatment planning: bolus design algorithms. *Medical Physics*.

Madamesila, J., McGeachy, P., Villarreal Barajas, J. E., & Khan, R. (2015). Characterizing 3D printing in the fabrication of variable density phantoms for quality assurance of radiotherapy. *Physica Medica*. http://doi.org/10.1016/j.ejmp.2015.09.013

Mayles, P., Nahum, A., & Rosenwald, J.-C. (2007). *Handbook of radiotherapy physics: theory and practice*. CRC Press.

Mazzoli, A. (2013). Selective laser sintering in biomedical engineering, 245–256. http://doi.org/10.1007/s11517-012-1001-x

Melchels, F. P. W., Domingos, M. A. N., Klein, T. J., Malda, J., Bartolo, P. J., & Hutmacher, D. W. (2012). Additive manufacturing of tissues and organs. *Progress in Polymer Science*, *37*(8), 1079–1104. http://doi.org/10.1016/j.progpolymsci.2011.11.007

Ministry of Health. (2010). *Cancer: New registrations and deaths*.

Mohan, R., Chui, C., & Lidofsky, L. (1985). Energy and angular distributions of photons from medical linear accelerators. *Medical Physics*, *12*(5), 592–597. http://doi.org/10.1118/1.595680

Nelson, G., & Reilly, D. (1991). Gamma-ray interactions with matter. *Passive Nondestructive Analysis of Nuclear Materials*, (I), 27–42. Retrieved from http://www.fas.org/sgp/othergov/doe/lanl/lib-www/la-pubs/00326397.pdf

Orton, C. (2013). *Progress in Medical Radiation Physics*. Springer US.

Podgoršak, E. B. (2005). *Radiation Oncology Physics: A Handbook for Teachers and Students*. International Atomic Energy Agency. Retrieved from https://books.google.co.nz/books?id=alRRAAAAMAAJ

Rengier, F., Mehndiratta, a, von Tengg-Kobligk, H., Zechmann, C. M., Unterhinninghofen, R., Kauczor, H.-U., & Giesel, F. L. (2010). 3D printing based on imaging data: review of medical applications. *International Journal of Computer Assisted Radiology and Surgery*, *5*(4), 335–41. http://doi.org/10.1007/s11548-010-0476-x

Stephens, B., Azimi, P., El Orch, Z., & Ramos, T. (2013). Ultrafine particle emissions from desktop

3D printers. *Atmospheric Environment*, *79*, 334–339. http://doi.org/10.1016/j.atmosenv.2013.06.050

Stratasys Inc. (2012). A New Mindset in Product Design.

Taylor, M. L., Smith, R. L., Dossing, F., & Franich, R. D. (2012). Robust calculation of effective atomic numbers: The Auto-Zeff software. *Medical Physics*, *39*(4), 1769. http://doi.org/10.1118/1.3689810

Tello, V. M., Tailor, R. C., & Hanson, W. F. (1995). How water equivalent are water-equivalent solid materials for output calibration of photon and electron beams? *Medical Physics*, *22*(1995), 1177–1189. http://doi.org/10.1118/1.597613

Ullmann's Encyclopedia of Industrial Chemistry. (2003). John Wiley & Sons. Retrieved from https://books.google.co.nz/books?id=rohUAAAAMAAJ

Ventola, C. L. (2014). Medical Applications for 3D Printing : Current and Projected Uses. *P&T*, *39*(10), 704–711.

Verhaegen, F., & Devic, S. (2005). Sensitivity study for CT image use in Monte Carlo treatment planning. *Physics in Medicine and Biology*, *50*(5), 937–946. http://doi.org/10.1088/0031-9155/50/5/016

White, D. R., Booz, J., Griffith, R. V, Spokas, J. J., & Wilson, I. J. (1989). Tissue substitutes in radiation dosimetry and measurement. *ICRU Report*, *44*.

Zwicker, A. P., Bloom, J., Albertson, R., & Gershman, S. (2015). The suitability of 3D printed plastic parts for laboratory use. *American Journal of Physics*, *83*(3), 281–285. http://doi.org/10.1119/1.4900746

Appendix 1: **Linear accelerators (LINACs)**

Some cancerous tumours are located deep in the body and require high energy photons to spare the normal tissue. MV energy photon beams are required to achieve the tissue sparing required; however it is not practical to use an x-ray generator above 300kV. MV radiation can be generated by several methods, with the most common being a clinical linear accelerator, often referred to as LINAC

Linear accelerators (LINACs) generate megavoltage electromagnetic radiation by accelerating electrons using energy transferred from microwaves rather than a direct potential like conventional x-ray tubes (Khan, 2010). A majority of radiation therapy machines rely on a LINAC as the source of high energy electrons, which can be used directly as a form of treatment or can be used to generate therapeutic photon beams. As discussed in section 1.2.2, the interactions that both photons and electrons undergo are dependent on energy. How and why LINACs produce a spectrum of energies will be described in this section.

Electrons are generated by thermionic emission by heating a triode tungsten filament which is part of an electron gun. Bunches of emitted electrons are then accelerated into the waveguide using a 15 kV direct potential. It is in the waveguide that the main energy portion is transferred and that the electrons are accelerated. The length and diameter of irises in the waveguide are carefully tuned so that the velocity of the microwaves matches the velocity of the electrons as they are accelerated. The amount of energy the electrons receive from the wave depends on their position on the wave. For the electrons to receive maximum energy, they must maintain their position in the optimal accelerating region of the wave.

The energy of the electrons depends largely on matching the wave velocity with the electron velocity (which affects the efficiency of energy transfer), the peak power level of the microwaves generated and the number of electrons to be accelerated.

To generate a photon beam, the high-energy electrons are focused onto a tungsten target. The electrons may undergo interactions that result in a complete loss of energy or they may only partially lose energy and undergo bremsstrahlung interactions in the material. The electrons will also undergo interactions with the tungsten nuclei at different depths. Both variation in the completeness and the depth of the interaction will result in the production of photons with a continuous spectrum of energies up to the initial energy of the electron (Ahnesjö & Andreo, 1989; Khan, 2010).

The energy spectrum of the photons produced is then altered as they pass through the conical flattening filter designed to make the beam intensity uniform across the field. The photons passing through the centre of the flattening filter pass through a greater thickness than those passing through

at a radial distance. As lower energy photons have a greater probability of interacting with high Z materials (which was also covered in section 1.2.2), the energy spectrum of the photons becomes a function of radial position, with those in the centre having a higher mean energy than those more radially distant.

The photon beam will be further altered as it passes through the beam-shaping elements of the radiation therapy machine. The spectrum of the beam will therefore also depend on the field size of the beam as it will determine how much of the central beam is transmitted and how much beam will interact with the beam shaping elements. The shape of the beam used to deliver treatment is first defined by jaws, square-edged high atomic material plates, which create a rectangular beam that is then further defined by the multi-leaf collimator (MLC), which is made up of up to 80 pairs of 5mm (at isocenter) high Z material leaves that can move independently to shape the beam. The photon beam interacts with the high Z materials producing scattered low energy photons and electrons.